A PHOSPHOR-BASED LIGHT-EMITTING DIODE USING WHITE-LIGHT CADMIUM SELENIDE NANOCRYSTALS

By

Jonathan David Gosnell

Dissertation

Submitted to the Faculty of the

Graduate School of Vanderbilt University

in partial fulfillment of the requirements

for the degree of

DOCTOR OF PHILOSOPHY

in

Interdisciplinary Materials Science

May, 2010

Nashville, Tennessee

Approved:

Professor Sharon M. Weiss

Professor Sandra J. Rosenthal

Professor Leonard C. Feldman

Professor Daniel M. Fleetwood

Professor Richard F. Haglund, Jr.

To my wife, Heather,

and my parents and in-laws. I would not have made it without their support.

ACKNOWLEDGEMENTS

This work would not have been possible without the generous financial support of the National Science Foundation (NSF) Integrative Graduate Research Experience and Training (IGERT) fellowship program, the financial and technical support of the Vanderbilt Institute of Nanoscale Science and Engineering (VINSE), and the financial support of Vanderbilt University through a Discovery Grant.

I am grateful to my dissertation committee for their time, assistance, and guidance throughout the completion of this work, especially my advisor Dr. Sharon Weiss. She has taught me so much about scientific research and writing, and has greatly helped me develop my analytical and experimental abilities. For their assistance with research topics and experimental measurements, I thank Michael Schreuder and Dr. James McBride (CdSe nanocrystal synthesis and many fruitful discussions), Dr. Dmitry Koktysh (absorbance and photoluminescence), Rossane DeLapp (ICP-MS measurements and theory), Dr. John McLean (ICP-MS theory), and Dr. Robert Geil (profilometry). A big thank you goes to Sarah Satterwhite for providing help in a range of areas, from class schedules to paychecks to being instrumental in getting the MRS chapter off the ground.

I would also like to thank Dr. Madis Raukas and David Bay at OSRAM Sylvania for allowing me to use their facilities for scattering and photoluminescence measurements. Though it was only a brief six months, I learned a great deal about laser operation, optical measurements, and experimental design from an industry perspective. I also discovered that Boston has beautiful weather during the summer months when twice-weekly soccer games are a must, and that tranquil, seaside towns like Rockport are

the perfect spot for both running and peaceful reflection. I am also grateful to the members of the Weiss group as well as Flo Wahidi and Lewis Saettel for the help that they have provided for me.

Finally, I am thankful to all of my family and friends for their encouragement and understanding throughout my graduate studies. I would like to thank my parents for their love and guidance, and for always believing in me no matter what I have chosen to do. Most importantly, I am grateful to my wife, Heather, for her moral support as we endured graduate school together.

TABLE OF CONTENTS

Page

LIST OF TABLES

LIST OF FIGURES

LIST OF ABBREVIATIONS

AAS	atomic absorption spectroscopy
AMU	atomic mass unit
BP-PFCB	biphenylperfluorocylcobutyl
CCD	charge-coupled device
CCT	correlated color temperature
CIE	commission internationale de l'éclairage
CRI	color rendering index
DBR	distributed Bragg reflector
DOE	Department of Energy
DPA	dodecylphosphonic acid
DRC	dynamic reaction cell
HDA	hexadecylamine
ICP-MS	inductively coupled plasma mass spectrometry
ICP-OES	inductively coupled optical emission spectrometry
IR	infrared
LED	light-emitting diode
MBE	molecular beam epitaxy
MOVPE	metallorganic vapor phase epitaxy
NC(s)	nanocrystal(s)
ODE	octadecene
OLED	organic light-emitting diode
PLED	polymer light-emitting diode
ppb	part per billion
ppm	part per million
ppt	part per trillion
RBS	Rutherford backscattering spectrometry
RF	radio frequency
SSL	solid-state lighting
TBP	tri-*n*-butylphosphine
TEM	transmission electron microscopy
TIP	truncated-inverted-pyramid
TOPO	tri-*n*-octylphosphine oxide
UV	ultraviolet
UV-VIS	ultraviolet-visible
XRD	x-ray diffraction
YAG:Ce	ytrrium aluminum garnet:cerium

CHAPTER I

INTRODUCTION

1.1 Solid-state lighting

The use of artificial light by humans can be traced back to as long as 500,000 years ago with the discovery of fire. This source of lighting was made portable through the use of torches, dishes, bowls, and baskets, among other containers. Beginning 30,000 to 70,000 years ago, it was found that the efficiency could be improved by using a stone lamp with a wick or other fiber inserted into melted fat. The Romans are credited with the first use of candles, where the fuel was melted by the heat of the flame. The first true modern lighting devices were invented towards the end of the eighteenth century, most notably an oil lamp with a much-improved efficiency and the introduction of gas lighting. The combustion of a gaseous fuel to produce light was used extensively for over a hundred years until the first practical incandescent filament lamps were invented at the end of the nineteenth century. Starting with Thomas Edison and Joseph Swan's introduction of a carbonized-paper filament lamp, later incandescent lamps featured metal filaments such as osmium, tantalum, and tungsten. At the beginning of the twentieth century low-pressure gas discharge lamps were introduced, first using mercury vapor that became the source of later fluorescent lamps that use a mercury discharge lamp coated with a phosphor to emit white light, and later using sodium vapor. At the end of the twentieth and into the twenty-first century, several of these technologies still dominate the general lighting market. Tungsten incandescent lamps, along with compact

fluorescent bulbs are widely used in residential lighting, fluorescent lighting is found in the vast majority of commercial lighting, and sodium lamps are featured in almost all street lighting. The newest method for achieving white light is through the use of a white light-emitting diode (LED), which has the potential to replace all of these older lighting technologies.[1]

With the potential for much longer lifetimes and lower energy consumption as compared to current lighting technologies, the use of LEDs, an area of research known as solid-state lighting (SSL), is likely to be a disruptive technology in the lighting industry in the coming years. A Department of Energy study found that a transition to solid-state lighting could decrease the total electricity usage for lighting by 62%, saving the U.S. $42 billion per year by 2025 in energy costs.[2-5] As a result, carbon dioxide emissions would also be reduced by 100 megatons per year. At the same time, LED lighting can provide a higher quality white light that reproduces the color of objects more effectively than most other lighting technologies. The main reason that there has not yet been a transition to solid-state lighting technologies is the lack of a highly efficient and high color quality white LED that is inexpensive and simple to manufacture.

1.2 Light-emitting diodes

Electroluminescence, or emission by injection of current into a material without the generation of heat, was first discovered and reported by Henry Round in 1907 using silicon carbide (SiC).[6] It was not until the mid-1920s that Oleg Losev invented what we now know as the LED, which was based on this phenomenon of electroluminescence. Losev was a technician who was working on radio receivers and noticed that the SiC

detector emitted light when current was passed through it.[7] The first practical LED, which emitted red light and was based on the material gallium arsenide phosphide (GaAsP), was invented in 1962 by Holonyak and Bevacqua at General Electric.[8] The first white LED was not possible until the blue LED was demonstrated in 1994 by Shuji Nakamura at Nichia Corporation.[9,10] After several years of development on blue LEDs to make them more efficient, a yellow phosphor coating made of $Y_3Al_5O_{12}:Ce^{3+}$ ($YAG:Ce^{3+}$) was added that converted some of the blue light to yellow, giving the appearance of white light.

The mechanism of electroluminescence is distinct from that of conventional lighting technology, which is based on incandescence (emission due to an object's temperature) or gas discharge (emission via an electrical discharge sent through an ionized gas, or plasma). An LED comprises a semiconducting material that is implanted, or doped, with electrons to form an n-type layer and holes to form a p-type layer. A hole is the absence of an electron in the valence band, and is formed when an electron is excited from the valence band to the conduction band. The difference in energy between the conduction band and valence band is referred to as the band-gap of a material. When an n-type and a p-type layer are joined together, a p-n junction is produced, which is shown in Figure 1.1. By applying a voltage, or bias, to the p-n junction, it can function as a diode. When electrons lose energy and recombine with a hole in the valence band, photons with energy equal to the band-gap of the material can be emitted, as displayed in Figure 1.2. The relationship between the band-gap energy and wavelength of emitted light is given in Eqn 1.1, where E_g is the band-gap energy, h is Planck's constant, c is the speed of light and λ is the emitted wavelength of the light.

$$E_g = \frac{hc}{\lambda} \tag{1.1}$$

The band-gap energy is a material property, which can be altered by combining, or alloying, different semiconductor materials. In this way, LEDs with different emission wavelengths can be fabricated to produce light in a variety of colors from the ultraviolet (UV) to the visible to the infrared (IR).

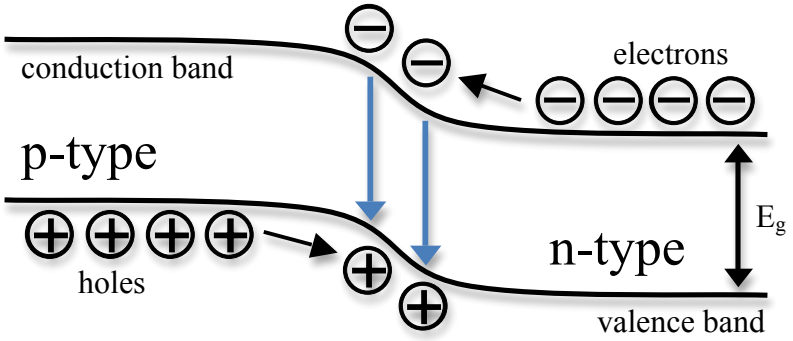

Figure 1.1: Diagram of a forward-biased p-n junction.

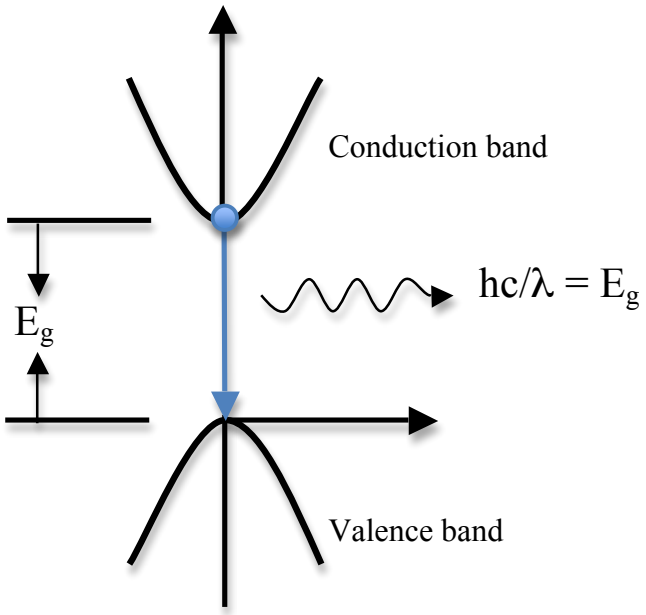

Figure 1.2: Diagram of a direct band-gap semiconductor, where an electron in the conduction band radiatively recombines with a hole in the valence band, emitting a photon of energy equal to the band-gap energy.

Because of losses in fluorescent lighting due to the difference between the absorption and emission spectral peaks, referred to as the Stokes shift, and the high operating temperatures of incandescent lighting, conventional lamps are not very efficient. Due to small energy losses and low operating temperatures, LEDs can be much more efficient than other lighting sources and have quantum yields that approach 1.[11,12] In addition, because LEDs do not rely on a filament for light emission as in many traditional sources, they can have lifetimes of up to 100,000 hours, 100 times longer than most incandescent lights and 5 to 10 times longer than fluorescent lights.[12] Table 1.1 shows values for the intensity (luminous flux), efficiency (luminous efficacy), and lifetime of conventional lighting compared to the goals of solid-state lighting for white LEDs. As discussed in the next sections, white LEDs can be fabricated using phosphor-conversion, multiple chips, and organic technology.[1]

Table 1.1: Luminous flux, luminous efficacy, and lifetime of common white-light sources compared to solid-state lighting.[1,4] Equations are provided to calculate these quantities in Tables 1.2 and 1.4.

White-Light Source	Luminous Flux (lm)	Luminous Efficacy (lm/W)	Lifetime (khrs)
Incandescent (120 V, 60 W)	865	14.4	1
Tungsten halogen (120 V, 50 W)	590	11.8	2
Fluorescent triphosphor (32 W)	2850	84	24
Compact fluorescent (15 W)	900	51	10
State of the art LED bulb (Cree LR6)	650	62	50
Solid-state lighting (goals)	1500	200	100

1.3 Phosphor-conversion LEDs

Phosphor-conversion LEDs employ a phosphor coating on top of an excitation LED. The phosphor absorbs some or all of the light from the excitation LED and, in turn,

emits light of another color. The proper color combination of phosphor emission and excitation LED emission can lead to the generation of white light. Schematics of several common phosphor-conversion LED designs are shown in Figure 1.3. The most common type of phosphor-conversion white LED is based on a blue InGaN/GaN LED and a yellow YAG:Ce^{3+} phosphor.[10,13-20] The efficiency of these LEDs has been shown recently in the laboratory to be as high as 186 lm/W and in commercial products as high as 132 lm/W (both by Cree, Inc.), and they are easy and inexpensive to manufacture. The combination of the blue light from the LED and the yellow light from the phosphor gives the appearance of white light, however it is a blueish-white and not ideal for general lighting due to its lack of red emission. In addition, since the blue light from the LED is highly directional and the yellow light from the phosphor is emitted in a 2π solid angle, the white light is not uniform in all directions. Furthermore, as the blue LED degrades over time, the color characteristics of the white light will change from their initial desired values. Scattering from phosphor particles, which is the main source of efficiency losses in phosphor-conversion LEDs, is the topic of Chapter 6.

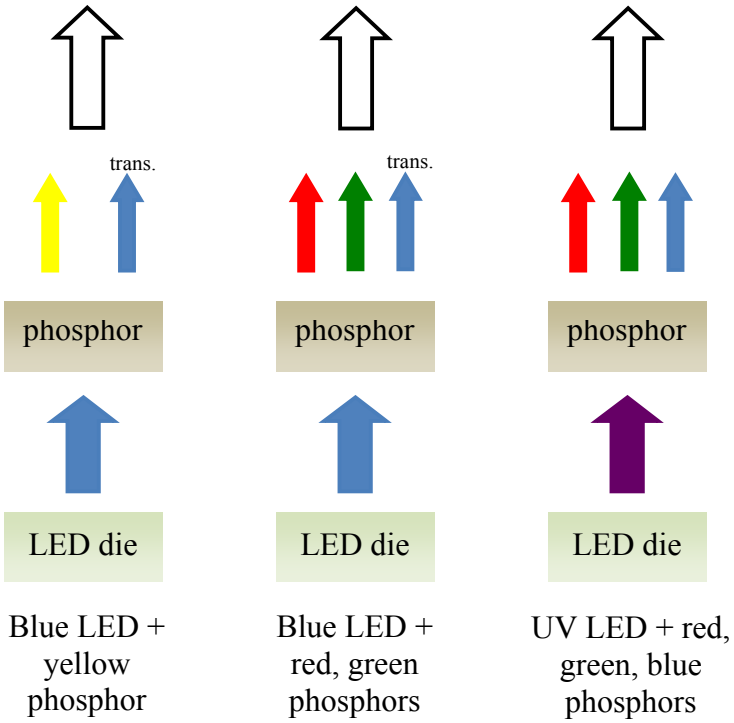

Figure 1.3: Schematics of three common designs of a phosphor-conversion LED. The notation of (trans.) signifies that some of the light from the LED is transmitted through the phosphor film and contributes to the emission characteristics of the device.

A higher degree of tunability can be obtained through the use of multiple phosphors, pumped by either a blue or UV LED.[21-26] A blue LED combined with both a red and a green phosphor will have better color rendering and overall a higher quality white light than with just a yellow phosphor. Similarly, a UV LED combined with red, green, and blue phosphors will have good control over the color quality and good color stability. These benefits are outweighed, however, by a more complex fabrication and higher Stokes energy loss, in addition to UV LEDs having a lower efficiency than blue LEDs.

1.4 Multichip LEDs

A potentially more efficient white LED design than using phosphor-conversion is a multichip LED, which uses separate red, green, and blue LEDs combined to achieve white light, as demonstrated in Figure 1.4.[27,28] The color rendering and color tunability of these LEDs is high, and can be tuned by balancing the power applied to each color die. Although there is no Stokes energy loss in these LEDs, which leads to a higher efficiency, the different colored LEDs will degrade at different rates and can disturb the delicate color balance with only small changes in the intensity of the different colors.[28] The use of a complicated feedback system will allow for tuning of the color balance, though this causes multichip LEDs to be much more expensive to manufacture and to maintain than phosphor-conversion LEDs.

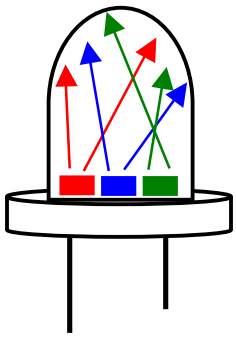

Figure 1.4: Schematic of a multichip white LED, which utilizes separate red, green, and blue dies that when combined together provide white light.

1.5 Organic Light-Emitting Diodes (OLEDs)

White LEDs can also be designed to use an organic compound that is used as the emission layer instead of a semiconductor material.[29-43] A typical OLED, consisting of a substrate, a conductive layer, an emissive layer, a cathode, and an anode, is shown in

Figure 1.5. To improve the efficiency, layers that aid charge injection or block holes or electrons from reaching the undesired electrode can be added. A voltage is applied across the layers of the device, where holes and electrons recombine in the emission layer, which can lead to radiative recombination and thus light emission. One of the advantages of these devices is the possibility of using materials that are flexible, which could lead to devices such as flexible displays or luminous wallpaper. Also, the ease and potential low cost of fabrication of OLEDs, as well as the versatility of color options through mixing and changing the organic, emitting materials, makes OLEDs an attractive option for solid-state lighting applications. Despite these advantages, there are currently significant challenges that OLEDs must overcome, including shorter lifetimes and lower color stability, before they are ready for widespread implementation in commercial lighting applications. Because the emitters of different colors degrade at different rates, OLEDs will also require a feedback system, much like the multichip white LEDs. In addition, the lifetime of white OLEDs is only projected to be about 20,000 hours, much shorter than the 100,000-hour projected lifetime of inorganic white LEDs.[2]

1.6 Performance of LEDs

1.6.1 Radiometry and photometry

Radiometry is the measurement of optical radiation, which is the range of the electromagnetic spectrum that includes ultraviolet, visible, and infrared light, in terms of the absolute power of the radiation. In contrast, photometry is the measurement of light that can be detected by the human eye, which is restricted to the visible region of the spectrum, and is weighted by the spectral response, or sensitivity, of the eye. Table 1.2

lists the quantities that are used to determine the intensity and brightness of a light source. Figure 1.5 shows the relative sensitivity of the human eye to different wavelengths of light in the visible spectrum under well lit (photopic) and low light level (scotopic) conditions.

Table 1.2: Quantities used for the determination of the intensity and brightness of a light source.[1]

Term	Symbol	Units	Description	Applicable Equation
Radiant flux	Φ_e	W	The energy per unit time that is radiated from a source	
Spectral density of the radiant flux (spectral power distribution)	$\Phi_{e\lambda}$ or $S(\lambda)$	W/nm	A graph of the radiant flux of the emitted light at each wavelength	$\Phi_{e\lambda} = \frac{d\Phi_e}{d\lambda}$
Radiant intensity	I_e	W/sr	The radiant flux from a point source per unit solid angle	$I_e = \frac{d\Phi_e}{d\omega}$
Spectral density of the radiant intensity	$I_{e\lambda}$	W/sr/nm	A graph of the radiant intensity of the emitted light at each wavelength	$I_{e\lambda} = \frac{dI_e}{d\lambda}$
CIE relative luminous efficiency function	$V(\lambda)$ or $V'(\lambda)$	unitless	Spectral response of the eye	1 W of radiant energy at 555nm (peak eye sensitivity) = 683 lumens; photopic ($V(\lambda)$) vision uses cones (color) and is for bright conditions, scotopic ($V'(\lambda)$) uses rods (black and white) and is for dark conditions; displayed in Figure 1.5
Luminous flux	Φ_v	lumen (lm)	The energy per unit time radiated over wavelengths visible to the human eye, weighted for eye sensitivity	$\Phi_v = 683\ lm/W \times \int \Phi_{e\lambda} V(\lambda) d\lambda$

Table 1.2, continued

Luminous intensity	I_v	candela (cd) = lm/sr	The luminous flux from a point source per unit solid angle	$I_v = \frac{d\Phi_v}{d\omega} = 683\ lm/W \times \int I_{e\lambda} V(\lambda) d\lambda$
Luminance	L	cd/m^2	A measure of the amount of light that passes through or is emitted by an area (element dA, area projected in observation direction is dA′) that is within a certain solid angle (observed angle θ)	$L = \frac{dI_v}{dA'} = \frac{d^2\Phi_v}{d\omega\, dA \cos\theta}$
Illuminance	E	lux (lx) = lm/m^2	The luminous flux incident on a surface per unit area at a distance of r from the source to the illuminated plane	$E = \frac{d\Phi_v}{dA} = \frac{I_v \cos\theta}{r^2}$

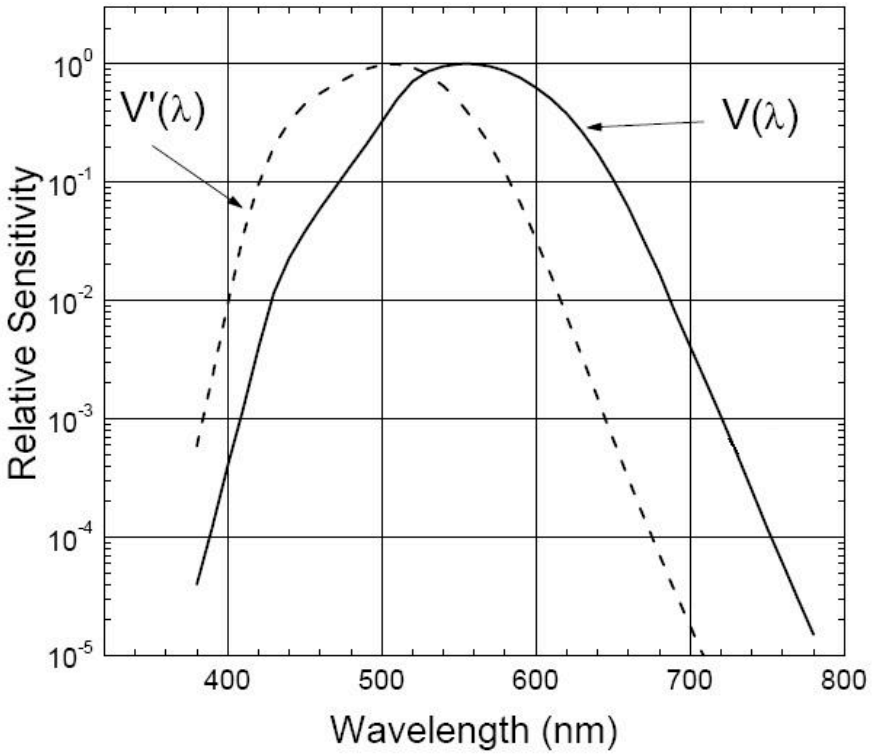

Figure 1.5: The spectral sensitivity curves for photopic (V(λ)) and scotopic vision (V ' (λ)).[1]

1.6.2 Colorimetry

While radiometry and photometry describe the intensity of a light source, colorimetry describes the color of a light source. The main quantities measured and given for different sources are the CIE chromaticity coordinates, color rendering index (CRI), and correlated color temperature (CCT). The 1931 CIE chromaticity coordinates x, y, and z represent the actual color as perceived by an average observer, and are calculated using Eqns 1.2 and 1.3:

$$x = \frac{X}{X+Y+Z} \qquad y = \frac{Y}{X+Y+Z} \qquad z = \frac{Z}{X+Y+Z} \tag{1.2}$$

where X, Y, and Z are the tristimulus values:

$$X = \bar{x}(\lambda)S(\lambda)d\lambda \quad Y = \bar{y}(\lambda)S(\lambda)d\lambda \quad Z = \bar{z}(\lambda)S(\lambda)d\lambda \tag{1.3}$$

and $\bar{x}$, $\bar{y}$, and $\bar{z}$ are the color matching functions, which are similar to the spectral sensitivity of the cones in our eyes, and displayed in Figure 1.6.

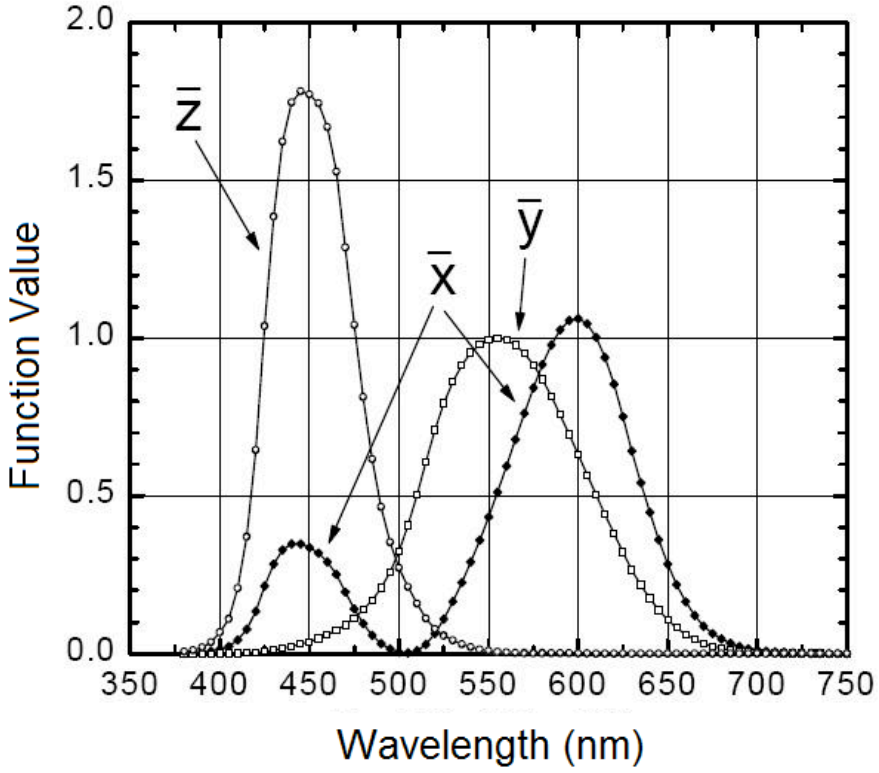

Figure 1.6: The 1931 CIE color-matching functions for red ($\bar{x}$), green ($\bar{y}$), and blue ($\bar{z}$).[1]

The chromaticity coordinates can be plotted on the CIE chromaticity diagram, seen in Figure 1.7. The ideal chromaticity coordinates for a white-light source are x=0.333, y=0.333, which is known as the equal energy point. The color rendering index is a measure of the ability of a light source to reproduce colors of an object illuminated by the light source. The scale of the color rendering index runs from 0, which represents the worst possible color rendition, to 100, the best possible color rendition. The correlated color temperature is the temperature in degrees Kelvin of a blackbody radiator that has

the same chromaticity as the tested light source, ideally between 2500 K and 6500 K for a white-light source. The Planckian locus, which is the locus of points for blackbody radiators at different temperatures can be seen in Figure 1.7 across the middle of the chromaticity diagram. The CIE coordinates, CRI, and CCT of common white-light sources are shown in Table 1.3.

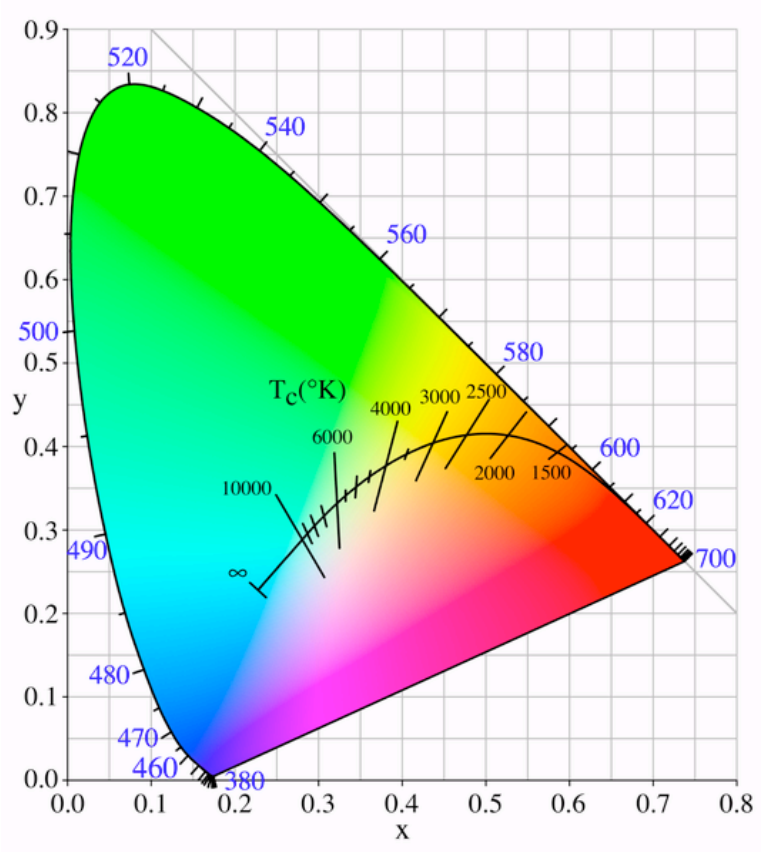

Figure 1.7: The 1931 CIE chromaticity diagram, showing the Planckian locus. Adapted from the Wikimedia Commons file "File:PlanckianLocus.png".

Table 1.3: CIE coordinates, CRI, and CCT for common white-light sources.[29] The Inova white-light LED keychain was measured in a Labsphere SLMS-LED-1050 integrating sphere system.

White-Light Source	CIE x	CIE y	CRI	CCT (K)
Daylight (CIE Standard Illuminant D_{65})	0.313	0.329	90	6500
Incandescent Bulb	0.448	0.408	100	2854
Fluorescent, cool white	0.375	0.367	89	4080
Fluorescent, warm white	0.440	0.403	72	2940
Inova white-light LED keychain	0.308	0.300	76	7137

1.6.3 Device efficiency

The general equations that govern the efficiency of both photoluminescent and electroluminescent LEDs are given in Eqns 1.4 and 1.5.[1] The terms in these equations are defined in Table 1.4.

$$\text{Overall efficiency (PL)} = \textit{Excitation LED efficiency} \times \eta_{phos} \times C_{ex} \tag{1.4}$$

$$\text{Overall efficiency (EL)} = \eta_{ext} \times \eta_{elec} = \eta_{inj} \times \eta_{\text{int}} \times C_{ex} \times \eta_{elec} \tag{1.5}$$

Increasing the efficiency of nanocrystal-based LEDs is the topic of Chapter 5. The terms in these equations are defined in Table 1.4 below.

Table 1.4: Quantities used in the determination of the efficiency of a light source.[1]

Term	Symbol	Units	Description	Important Equation
Phosphor efficiency	η_{phos}	unitless	Includes absorption efficiency (proportion of excitation photons absorbed by the phosphor), conversion efficiency (quantum yield), and Stokes loss (emitted divided by excitation energy)	$\eta_{phos} = \eta_{abs} \times \eta_{conv} \times \frac{E_{emit}}{E_{exc}}$
Extraction efficiency	C_{ex}	unitless	The proportion of generated photons that escape the device	

Table 1.4, continued

Injection efficiency	η_{inj}	unitless	The proportion of injected electrons that reach the active region of the device	
Internal quantum efficiency	η_{int}	unitless	The ratio of photons generated to the number of electrons that are injected into the active region of the LED	
External quantum efficiency	η_{ext}	unitless	The ratio of the number of photons that escape the device to the number of injected electrons	$\eta_{ext} = \eta_{inj} \times \eta_{\text{int}} \times C_{ex}$
Luminous efficacy of radiation (LER)	K	lm/W	A measure of the ability of the radiated light to produce visible light	$K = \frac{\Phi_v}{\Phi_e} = 683\ lm/W \times \frac{\int_{380}^{780} V(\lambda)S(\lambda)d\lambda}{\int_0^{\infty} S(\lambda)d\lambda}$
Radiant efficiency or wall-plug efficiency	η_e	unitless	The ability of a light source to convert electrical power (P, in units of W) into radiant flux	$\eta_e = \frac{\Phi_e}{P}$
Luminous efficacy	η_v	lm/W	The ability of a light source to convert electrical power into visible light	$\eta_v = \frac{\Phi_v}{P} = \eta_e \times K$
Electrical efficiency	η_{elec}	unitless	The conversion to photon energy (in eV) from electrical energy (V_a is applied voltage)	$\eta_{elec} = \frac{E_{photon}}{e \times V_a}$

1.6.4 Light extraction

The main factor that limits the light extraction efficiency in LEDs is total internal reflection. The critical angle θ_c for total internal reflection is calculated by Snell's law, which is given by Eqn 1.6:

$$\theta_c = \sin^{-1}\left(\frac{n_e}{n_s}\right) \tag{1.6}$$

where n_e is the index of refraction of epoxy or the material above the semiconductor LED chip, whose refractive index is n_s. The escape cone is the three-dimensional volume defined by the critical angle where within the cone light can be transmitted, and outside the cone light will be reflected. The surface area of the top of the cone can be calculated by Eqn 1.7:

$$A_{cone} = \int dA = \int_{\theta=0}^{\theta=\theta_c} 2\pi r \sin\theta \, r \, d\theta = 2\pi r^2 \left(1 - \cos\theta_c\right) \tag{1.7}$$

The light that is inside the cone and escapes is then given by Eqn 1.8:

$$\frac{A_{cone}}{A_{sphere}} = \frac{2\pi r^2 \left(1 - \cos\theta_c\right)}{4\pi r^2} = \frac{1}{2}\left(1 - \cos\theta_c\right) \tag{1.8}$$

The Fresnel reflection loss at the semiconductor-epoxy surface is found with Eqn 1.9:

$$T = 1 - R = \frac{4 n_s n_e}{\left(n_s + n_e\right)^2} \tag{1.9}$$

and at the epoxy-air interface with Eqn 1.10:

$$T = 1 - R = \frac{4 n_e}{\left(1 + n_e\right)^2} \tag{1.10}$$

The extraction efficiency C_{ex} for a single surface is then calculated by multiplying the transmission at the epoxy-air interface by the solid angle or escape cone and by the transmission at the semiconductor-epoxy interface using Eqn 1.10:[1,44]

$$C_{ex} = \frac{4n_e}{(1+n_e)^2} \times \frac{1}{2}(1-\cos\theta_c) \times \frac{4n_s n_e}{(n_s+n_e)^2} \tag{1.10}$$

For semiconductor materials, the index of refraction is usually large and therefore the extraction efficiency will be just a few percent for a single surface, planar LED. To improve this low extraction efficiency value, many different techniques have been investigated, including surface roughening,[45-47] mirrors/distributed Bragg reflectors (DBRs),[48-52] photonic crystals,[53-61] chip-shaping,[62-64] remote phosphor design,[65-67] and micro-patterning.[68-72] These techniques are described briefly below. Record extraction efficiencies of up to 75% have been achieved for blue LEDs based on OSRAM's ThinGaN technology, where a laser lift-off removes the GaN film from the sapphire substrate.[73-75]

Surface roughening increases the extraction efficiency by reducing losses due to light reflection at the surface, typically enhancing the extraction efficiency by 1.5 to 2 times as compared to a non-roughened surface. Because most semiconductors have very narrow escape cones into epoxy or air, a roughened surface presents many different angles or facets and is thus more likely to allow the light to pass through. The use of mirrors/DBRs in LEDs will be discussed in more detail in section 5.5. Photonic crystals can increase light extraction by enhancing spontaneous emission in favorable modes and inhibiting emission in other modes. By eliminating guided modes, the extraction efficiency has been predicted to exceed 90% when using a 2D photonic crystal.[54] Similar to the idea of surface roughening, chip-shaping aims to increase the probability of a

photon impinging on a surface at low angles of incidence. The most successful design of chip-shaping is the truncated-inverted-pyramid (TIP) LED which redirects photons from the sidewalls to the top surface and from the top surface to the sidewalls at low angles of incidence, resulting in an external quantum efficiency of 55%.[62] The remote phosphor design places the phosphor layer at a distance from the LED chip that is larger than the width of the chip, which reduces the probability of light that is scattered from the phosphor particles being reabsorbed by the chip. Micro-patterning is a collection of techniques that are based on increasing the outcoupling of light, such as microlens arrays or microdisks.

1.7 Objective and overview of the dissertation

The objective of this dissertation is to investigate an alternative method for achieving white LEDs based on the use of monodisperse, small, white-light emitting cadmium selenide (CdSe) nanocrystals. Several issues related to the characteristics of an ideal white LED, including a balanced emission over the entire visible spectrum with little to no UV or infrared emission, low self-absorption or scattering losses, high device efficiency, inexpensive and simple manufacturing process, and a long lifetime, will be discussed with respect to CdSe white LEDs. Chapter 2 introduces CdSe nanocrystals and their application to LEDs. Chapter 3 gives an overview of the methods and techniques that were used to characterize the CdSe nanocrystals and the properties of the devices fabricated based on this material. In particular, the absorption and photoluminescence spectroscopy of nanocrystal solutions and encapsulated nanocrystal films, thickness measurements of encapsulated nanocrystal films, and use of inductively coupled plasma

mass spectrometry and inductively coupled plasma optical emission spectrometry to determine the concentration of nanocrystals in solution will be discussed.

Chapter 4 focuses on the encapsulation of CdSe nanocrystals to form phosphor-conversion white LEDs, and characterization of the absorbance and photoluminescence properties of the encapsulated nanocrystal films. Chapter 5 presents methods to increase the efficiency of CdSe phosphor LEDs, including the optimization of film thickness and excitation wavelength, and simulations of dielectric mirrors that could be used to redirect light that would otherwise not escape the LED package. As the efficiency of most phosphor-conversion LEDs is limited by scattering of light by the phosphors, Chapter 6 discusses the size-dependent scattering properties of both common, micron-sized phosphor particles and ultrasmall CdSe nanocrystals. Measurements of the extinction coefficient of CdSe nanocrystals are also presented and compared to previous reports. Chapter 7 summarizes the highlights of this dissertation and suggests areas for future research and further improvements of CdSe nanocrystal-based LEDs. Appendices A and B present detailed procedures for Ar-Kr laser excitation and integrating sphere emission measurements, respectively. Appendices C and D display the Matlab code used to calculate the reflectance for a dielectric mirror and the scattering properties of particles in the Rayleigh and Mie regimes, respectively.

CHAPTER II

CADMIUM SELENIDE NANOCRYSTALS

2.1 Introduction

Nanocrystals are particles of nanoscale dimension (e.g. < 100 nm) that have a single-crystalline structure. If they are composed of a semiconductor material, such as cadmium selenide (CdSe), they are sometimes referred to as quantum dots. The most common methods for synthesis of nanocrystals include molecular beam epitaxy (MBE), metallorganic vapor phase epitaxy (MOVPE), laser ablation, ion implantation, organometallic, and other organic, solution phase reactions. CdSe nanocrystals are most often synthesized using organometallic or other organic solution phase reactions.[76,77] Due to the phenomenon of quantum confinement,[78,79] the absorption and emission properties of CdSe nanocrystals are tunable by changing their size, as illustrated in Figures 2.1 and 2.2.[80,81] For CdSe nanocrystals of size smaller than the bulk Bohr exciton radius, the properties of the nanocrystals can be treated as analogous to the one-dimensional particle-in-a-box model. The bulk Bohr exciton radius is the natural separation distance between an electron and a hole, and is approximately 5.6 nm for CdSe.[82] Thus, for CdSe nanocrystals below roughly 10 nm in diameter, the energy levels of the nanocrystal can be treated as discrete. For the particle-in-a-box, the energy levels are inversely proportional to the square of the width of the box. Likewise, as the nanocrystal diameter becomes smaller, the exciton becomes more confined, which increases the spacing between energy levels and causes the nanocrystal absorption and

emission to occur at higher energies (shorter wavelengths). Consequently, for smaller nanocrystals, the absorption and emission will shift to shorter wavelengths, and for larger nanocrystals, the absorption and emission will shift to longer wavelengths.

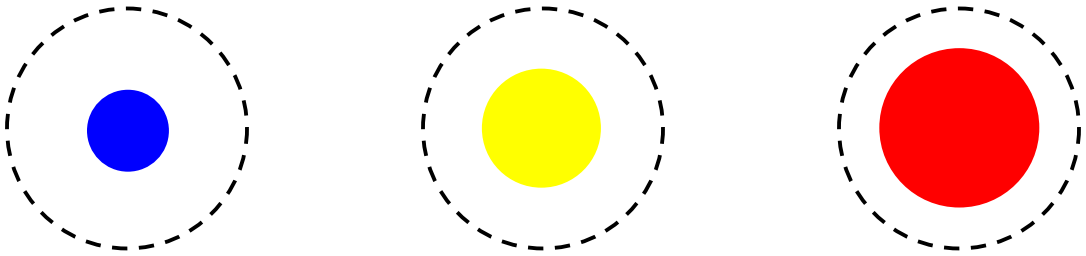

Figure 2.1: Diagram of the bulk Bohr exciton radius (dashed line), which is 5.6 nm for CdSe, compared to the size of a nanocrystal and its corresponding emission color. Smaller nanocrystals will emit at shorter wavelengths, while larger nanocrystals emit at longer wavelengths. These are not drawn to scale, but used to illustrate the size-tunable emission property.

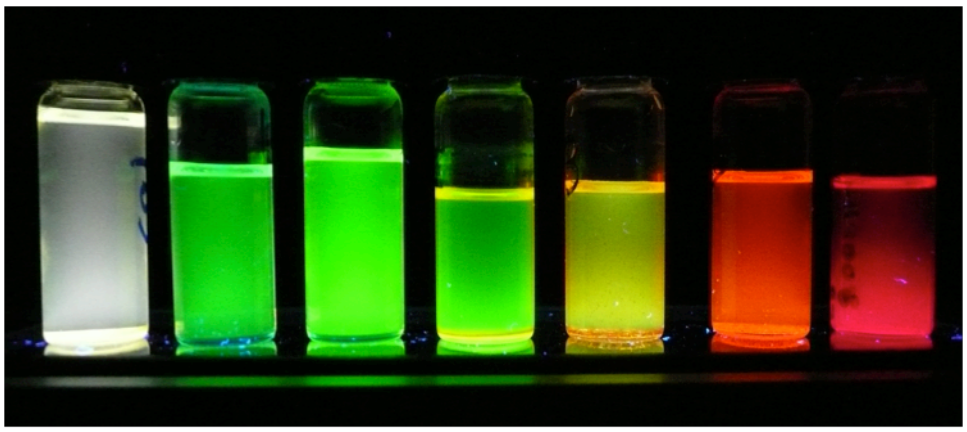

Figure 2.2: Emission of different sizes of CdSe nanocrystals, from the smallest on the left (1.5 nm diameter) to the largest on the right (5.0 nm diameter). As will be discussed in Section 2.2, the smallest nanocrystals on the far left emit white light.

The unique property of size-tunable absorption and emission, along with a surface that is accessible for chemical modification and narrow absorption and emission bands,

makes nanocrystals attractive for applications in medicine[83-91] and sensing.[92-96] Other important nanocrystal qualities, including thermal, electrical, and photo-oxidative stability, and high quantum efficiency, are important for lighting applications such as the emissive component of light-emitting diodes. Typically, nanocrystals emit in a narrow wavelength band and are thus incorporated into monochromatic LEDs. To use nanocrystals in a white-light emitting solid-state lighting device, several sizes of nanocrystals must be mixed together.[97-104] This method requires complex color mixing to achieve high-quality white light and suffers from losses due to self-absorption.

2.2 Nanocrystal-based LEDs

The first nanocrystal-based LEDs were reported in 1994, and used a single size of CdSe nanocrystals to produce a single-color light source.[105] Later devices have used either a single size or multiple sizes of nanocrystals of various materials combined with organic emitting layers to produce monochromatic light[106-116] or white light.[97,101,117,118] Other devices have used colored or UV LEDs to excite nanocrystals and generate white light.[98-100,102-104,119] Less common approaches to nanocrystal-based LEDs include nanocrystals encapsulated in direct charge injection layers of GaN,[120] and nonradiative energy transfer to nanocrystals from a quantum well.[121,122] Many of the issues that other white LEDs face also cause problems for these nanocrystal-based white LEDs, including the halo effect, complex mixing of colors, and efficiency losses due to self-absorption from combining different phosphors or sizes of nanocrystals.

2.3 Ultrasmall nanocrystals

Many of the issues that plague nanocrystal-based and other white LED designs could be resolved by utilizing single-sized, ultrasmall (~1.5 nm diameter) CdSe nanocrystals that emit broad spectrum white light, as shown in Figure 2.3.[123-127] The monodisperse nature of the nanocrystals minimizes self-absorption while the broadband emission obviates the need for complex color mixing. Recent work by the Rosenthal group has shown that for CdSe nanocrystals with diameters < 2 nm, the nanocrystal emission is no longer dominated by the band-edge emission, which is seen in larger, single-color nanocrystals.[128,129] While the band-edge absorption peak will continue to shift to lower wavelengths as the nanocrystal size decreases, the first emission feature does not appear to shift, but appears to be pinned at a certain wavelength. The origin of this pinned emission is believed to be trap states on the surface of the nanocrystal, and can be influenced by the surface ligands.

The emission characteristics of the white-light ultrasmall CdSe nanocrystals are distinct from other ultrasmall CdSe nanocrystals that have been reported using different synthesis methods. The synthesis method for the white-light ultrasmall nanocrystals is provided in Section 2.4. The non-white-light ultrasmall CdSe nanocrystals possess a band-edge absorption peak near 414 nm, which is similar to that of white-light ultrasmall nanocrystals.[130,131] However, the non-white-light ultrasmall nanocrystals show a broad, red-shifted emission spectra without emission in the blue region, and thus do not provide high-quality white light.[132]

Characterization of ultrasmall white-light CdSe nanocrystals and exploration of their use is the subject of Chapters 4-6. One key issue related to these nanocrystals that

will not be discussed in depth in this dissertation is quantum yield. The quantum yield for these nanocrystals was originally 3% when first discovered in 2005.[123] Since then, the quantum yield has steadily increased to 10% through the use of different phosphonic acids during the nanocrystal synthesis. For single-color nanocrystals, the quantum yield is typically increased by adding a shell of a wider band-gap material such as ZnS. These core-shell nanocrystals have a higher quantum yield due to the passivation of surface nonradiative recombination sites. For ultrasmall nanocrystals, however, the surface states are believed to be the cause for the broad spectrum emission. This means that the traditional method of increasing the quantum yield cannot be used for ultrasmall nanocrystals, and thus another method must be discovered which preserves these surface states.

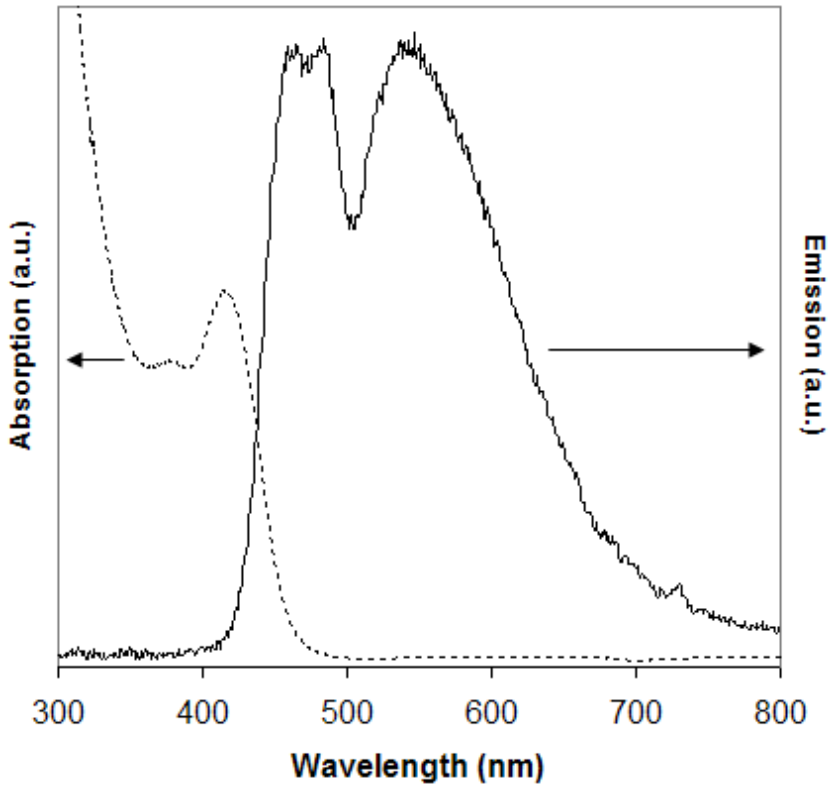

Figure 2.3: Absorption (dashed line) and emission spectra (solid line, with λ_{ex} = 367 nm) of white-light emitting CdSe nanocrystals in solution.

Several other groups have recently reported white light emission from a single size of nanocrystals. One method involves the doping of LaF_3 nanoparticles with Eu^{3+}, Tb^{3+}, and Tm^{3+} ions to emit red, green, and blue light.[133] This approach is similar to the idea of mixing different color phosphors and comes with the same disadvantages, such as self-absorption losses and difficult color control by having to maintain precise blending ratios to attain high-quality white light. A similar method used an "onionlike" CdSe/ZnS/CdSe/ZnS core-shell-shell structure that emits one wavelength from the core and another from the shell due to their different sizes and materials, which combine to give white light, and thus has the same issues as the doped-LaF_3 nanoparticle approach.[134] A recent report involved the use of Mn^{2+}-doped CdS nanocrystals, where the surface-state emission from CdS and the dopant emission from Mn^{2+} contribute different colors to achieve white light.[135] The chromaticity of the white light depends on the relative proportions of the CdS and Mn^{2+} emission which leads to a complex fabrication. Also, the quantum yield of these particles is currently very low (2%) and thus any devices based on these particles will have a low efficiency. Later work by Shea-Rowher and co-workers on CdS quantum dots synthesized in inverse micelles have resulted in quantum yields as high as 37%, though the current color quality (CRI < 75 and yellowish-white color coordinates) could limit the applications of these materials.[119,136,137]

2.4 Cadmium selenide nanocrystal synthesis

The method used to synthesize nanocrystals for this work was based on a cadmium oxide precursor and results in nanocrystals with phosphonic acid ligands. Tri-

n-octylphosphine oxide (TOPO, 90% tech. grade), hexadecylamine (HDA 90% tech. grade) and octadecene (ODE, 90% tech. grade) were purchased from Sigma-Aldrich and used as received. CdO (99.999% Puratrem), tri-*n*-butylphosphine (TBP, 97%), and selenium powder (200 mesh) were purchased from Strem and used as received. Dodecylphosphonic acid (DPA) was synthesized via the Arbuzov reaction from triethylphosphite and 1-dodecylbromide followed by acid work up with concentrated HCl and recrystallization from cold ethyl acetate.[138] All other solvents were HPLC grade and purchased from Fisher Scientific unless otherwise noted.

A 1.0 M stock solution of selenium in TBP was produced by dissolving 11.84 g selenium powder in 150 mL of TBP. The injection solution was produced by further diluting a 0.2 M Se:TBP solution with TBP. This solution was stable for several days stored in a capped bottle, under nitrogen or argon at room temperature. The reaction solvent was mixed from a unit quantity of TOPO and HDA (7.0 g and 3.0 g respectively) along with 0.128 g of CdO and 0.496 g of DPA (scaled as necessary). These chemicals were placed in a 100 mL three-neck flask, with a temperature probe, a bump trap, and a septum in the three necks. A needle was placed in the septum to allow for an argon purge until the reaction solution reached 150 ºC, at which point the reaction vessel was considered water and oxygen free.

The reaction continued to be heated under argon with vigorous stirring up to 320 ºC. Upon reaching reaction temperature, 4.25 mL of the 0.2 M Se:TBP solution along with 2.00 mL of ODE solution were mixed in a syringe and swiftly injected. Following this injection the temperature of the reaction flask was maintained between 270 ºC and 240 ºC. To achieve ultrasmall nanocrystals (e.g. < 20 Å), a second syringe of

butanol (typically 10 mL) was injected to reduce the reaction temperature to <130 ºC within 2-10 seconds after the initial injection (depending on the desired size). Further cooling using compressed air, applied to the outside of the reaction flask, cooled the solution to <100 ºC. The nanocrystals were then removed from the coordinating solvents using methanol and hexanol washes, before being suspended in toluene.

For larger CdSe nanocrystals, the butanol shot was injected when the nanocrystals had grown to their desired size, usually within several minutes. Alternatively, the reaction can be slowed down with just compressed air for larger nanocrystals, as the nanocrystal growth is more rapid at the beginning. If a range of different nanocrystal sizes is needed, small pulls of the reaction solution can be taken after the Se:TBP injection as the nanocrystals grow in size. This was done, for example, to achieve a number of nanocrystal sizes for the extinction coefficient measurements in Section 6.5.

CHAPTER III

EXPERIMENTAL TECHNIQUES

3.1 Absorption spectroscopy

Absorption spectroscopy measurements were acquired with a Varian Cary 5000 UV-VIS spectrophotometer. This instrument allows for measurement of the absorption spectra, which is simply the absorbance as a function of wavelength. The absorbance can be obtained by measuring the initial intensity of the incident light, $I_0(\lambda)$, as well as the intensity of the light transmitted through the sample, $I(\lambda)$. These measured quantities are then related to the absorbance with Eqn 3.1, assuming negligible reflectance:

$$A(\lambda) = -\log T = -\log\left(\frac{I(\lambda)}{I_0(\lambda)}\right) \tag{3.1}$$

It should be noted that frequently the terms absorbance and optical density are used interchangeably. Also, if the material of interest is dissolved in a solvent with nonzero absorbance in the examined wavelength range, or likewise if the cuvette that the solution is placed in or the substrate that the film is deposited on has a nonzero absorbance, then a reference absorbance spectrum must be taken to subtract its contribution from the sample's absorbance spectrum. When measured in solution, the CdSe nanocrystals were typically dissolved in toluene and placed in a glass cuvette for measurement. CdSe nanocrystal films were typically deposited onto glass microscope slides.

The absorbance (A) of the sample can be related to the molar extinction coefficient (ε, in L/mol/cm), the concentration (c, in mol/L), and the path length or

thickness that light travels through the sample (l, in cm) using the Beer-Lambert Law in Eqn 3.2:

$$A = \varepsilon c l \tag{3.2}$$

Thus, if the thickness of the sample and its molar extinction coefficient are known, the concentration can be calculated by measuring the absorbance. This is beneficial because the concentration of a nanocrystal solution is notoriously difficult to measure directly. The determination of the extinction coefficient for CdSe nanocrystals is discussed in detail in Section 6.5. Absorbance measurements can also be used to infer the size of a nanocrystal, as it has been shown that the band-edge absorption wavelength is directly related to the nanocrystal diameter. A sizing curve, such as the one shown in Figure 6.8, is established by measuring the diameters of a range of CdSe nanocrystals using transmission electron microscopy and measuring the band-edge absorption wavelength using absorbance measurements of the same solutions nanocrystals in solution.

3.2 Photoluminescence spectroscopy

Photoluminescence spectroscopy measurements were made via multiple instruments and experimental setups. Briefly, photoluminescence is the spontaneous emission of light from a material upon optical excitation with a light source of higher energy (shorter wavelength). The absorption of a photon causes an electron to be excited to a higher energy state, followed by a return to a lower energy state and the emission of a photon. Photoluminescence measurements can be used to determine the band-gap energy of a semiconductor material based on the wavelength of the emission peak. For nanocrystals, photoluminescence measurements allow for the calculation of the

nanocrystal quantum yield,[139] and the wavelength of the emission peaks can help determine the sources of the emission,[140] such as band-edge, defect, and deep-trap emission. In this work, photoluminescence measurements were typically performed to determine the emission intensity and color quality of thin films of nanocrystals.

One photoluminescence measurement system used in this work was an ISS PC1 photon counting spectrofluorometer. This system consists of a 300 W high-pressure xenon arc lamp with a monochromator used for excitation, with another monochromator and a Model R928P photomultiplier tube by Hamamatsu used to measure the photoluminescence from 240-900 nm. Another similar instrument used was a HORIBA Jobin Yvon FluoroLog-3 spectrofluorometer, which used a 450 W xenon lamp and the same Hamamatsu R928P detector; both the light source and the detector use monochromators to selectively pass desired wavelength ranges.

The third photoluminescence apparatus consisted of either a Labsphere SLMS-LED-040 (four-inch diameter) or SLMS-LED-1050 (ten-inch diameter) integrating sphere system that was fiber-optically coupled to a CDS 500 CCD-based spectrometer that measured the emission from 350-850 nm. An integrating sphere is a spherical enclosure with a highly reflective inner surface, where all of the light emitted by a sample placed inside the sphere can be used for measurement instead of only a small portion of the emission measured by planar detectors. The inner surface of the sphere approximates that of an ideal Lambertian scatterer, meaning that the light is scattered uniformly in all directions. A measurement at the exit port of the sphere is then representative of the entire emission from a sample. After calibration with a source of

known spectrum and intensity, several radiometric and photometric properties, including the spectral features and emission intensity of the sample, can be accurately determined.

The four-inch integrating sphere has a higher sensitivity than the ten-inch integrating sphere because it has a smaller surface area and thus more light will be incident on the exit port for detection. The ten-inch integrating sphere, however, allows for larger samples/sources to be measured and has a small stage for mounting of sample holders or other equipment, whereas the four-inch sphere only has two alligator clips to deliver power to the source or hold the sample. Excitation sources used with the integrating spheres included UV or blue LEDs with peak wavelengths of 365, 375, 385, 395, 405, 410, or 423 nm (from Nichia and Roithner LaserTechnik), and the UV lines (350-355 nm) of a Coherent Innova 70C Spectrum Ar-Kr laser. A detailed procedure for using the Ar-Kr laser for excitation can be found in Appendix A. The LEDs were typically powered at approximately 20 mA and 4 V using a Keithley 2400 sourcemeter. The software included with the Labsphere system calculated the radiant flux, luminous flux, CIE chromaticity coordinates, correlated color temperature (CCT), and color rendering index (CRI) based on the emission spectrum. A detailed procedure for using the Labsphere integrating sphere system is found in Appendix B.

3.3 Film thickness measurements

Thickness measurements of nanocrystal and polymer films were performed using either a Veeco DekTak 150 profilometer or a digital micrometer. A profilometer is a tool that uses a small stylus that is scanned laterally across a sample to trace the surface height variations of the sample. Profilometer scans allows for the calculation of film thickness

and surface roughness based on the measured surface profile. The Dektak 150 has a vertical resolution of 1 Å (0.1 nm) with a step height repeatability of < 6 Å as specified by the manufacturer. The profilometry measurements were made by starting in a corner of the samples on glass slides where there was no film to get a baseline. The speed of the profilometer tip was typically set to 100 μm/s, and was scanned for at least 3-5 mm. This was done to scan over at least half of the film, which allows for the measurement of the peak film thickness. The maximum thickness that could be measured by this instrument was found to be approximately 250 μm. For films above this thickness, a digital micrometer with an accuracy of ± 1 μm was used to make 3 thickness measurements at different spots on the film, with an average of these measurements taken as the film thickness. A range of films below 250 μm in thickness was measured using both the profilometer as well as the digital micrometer, and were in agreement within an error of ± 2%. The dropcasting method employed for the fabrication of our nanocrystal films resulted in a thin ridge around the edge of the film that was typically ~ 20-30% higher than the average film thickness. Excluding this thin ridge, the thickness of the remainder of the film typically had a variation < 5%.

3.4 Inductively coupled plasma mass spectrometry measurements

An inductively coupled plasma mass spectrometer (ICP-MS) is an instrument used to measure the concentration of ions of metals as well as several non-metals in a liquid or solid sample. In this work, ICP-MS was used to measure the concentration of nanocrystals in a solution. First, the samples must be prepared for ICP-MS measurement. A solution of CdSe nanocrystals was measured for absorbance, and then left to dry in a

vial inside a fume hood for several days. With the sample dried, 570 μL of aqua regia (3:1 ratio of hydrochloric acid (HCl) to nitric acid (HNO_3)) was added to the vial and left closed inside a fume hood for one hour to ensure that all of the CdSe nanocrystals were digested. Next, this solution was added to 9.43 mL of water to make a 10 mL sample with 1% nitric acid. At the same time, a 1% nitric acid blank was prepared. The samples were all given to Rossane DeLapp in the Department of Civil and Environmental Engineering at Vanderbilt University for ICP-MS measurement.

The ICP-MS instrument employed was a Perkin-Elmer ELAN DRC II. The instrument uses an inductively coupled plasma, or ionized gas, of argon gas to produce excited atoms or ions of the material that is being tested. Though solid samples can be measured using ICP-MS by vaporizing the sample using a laser or heated cell, liquid samples are more commonly used. To introduce the sample into the instrument, a nebulizer converts the sample into very small droplets, which are then carried into the plasma by a spray chamber. The atoms in the droplets are then ionized by the plasma and sent to the mass spectrometer, which separates and measures the ions based on their mass-to-charge ratio.

To perform the ICP-MS measurements, calibration standards with a known concentration of a particular element and a blank sample of 1% nitric acid in water were first measured. The calibration standards were used to normalize the concentration values in the same range of the samples to be measured. The blank is used to subtract any contribution from the water and aqua regia used to dissolve the sample. The specific instrument settings used in the measurements can be found in Table 3.1. The results from

the measurements of Cd-114 and Se-78 are in terms of counts per second, which can be transformed into concentration in µg/L using the data from the calibration standards.

Table 3.1: Instrument settings for ICP-MS using a Perkin-Elmer ELAN DRC II.

Nebulizer flow:	0.95	L/min
Radio Frequency (RF) Power:	1300	W
Plasma Gas Flow:	15	L/min
Lens Voltage:	6.5	volts
Auto Lens:	On	
Analyte in Standard Mode:	Cd	
Analyte in DRC Mode:	Se	
DRC (dynamic reaction cell with oxygen)		
Internal Standard:	In	
Replicates per reading:	3	
Dwell Time per AMU:	100	ms
Integration Time:	1000	ms
Scan Mode:	Peak Hopping	

3.5 Inductively coupled plasma optical emission spectrometry measurements

An inductively coupled plasma optical emission spectrometer (ICP-OES) was also used to measure nanocrystal concentration as a means of verifying the results obtained from ICP-MS. Traditionally, either atomic absorption spectroscopy (AAS) or ICP-OES has been used for elemental analysis of samples. The advantage of AAS is that it has high sensitivity, typically sub-ppb (part per billion), while ICP-OES sensitivity is on the order of ppb to ppm (part per million). ICP-OES has the capability to detect multiple elements simultaneously, whereas AAS is a single-element technique. With the advent of ICP-MS, the high sensitivity of AAS and the multi-element analysis of ICP-OES are combined in the same instrument. ICP-MS sensitivity can be as low as ppt (part per trillion) up to ppm depending on the instrument. For poorly ionizing elements,

which include both Cd and Se, the use of ICP-MS is advantageous because of its high sensitivity. To verify the results found in this work using ICP-MS, less dilute samples that were in the dynamic range of both instruments were used.

The ICP-OES instrument is very similar to ICP-MS, where an inductively coupled plasma produces excited atoms or ions, though it measures the wavelength of emission that corresponds to a certain element instead of the mass-to-charge ratio as in ICP-MS. These ions will lose electrons and recombine in the plasma repeatedly, where the photons generated by this process will be emitted at wavelengths characteristic of the elements found in the sample. The sample preparation for ICP-OES was the same as for ICP-MS, which is detailed in Section 3.4. Calibration standards and a blank were employed in a manner similar to that described in Section 3.4. The ICP-OES instrument used was a Perkin-Elmer Optima 7000 DV. The instrument settings used for ICP-OES are given in Table 3.2. The Cd concentration was measured at λ=228.802 nm, and the Se concentration was measured at λ=196.026 nm.

Table 3.2: Instrument settings for ICP-OES using a Perkin-Elmer Optima 7000 DV.

Plasma Gas Flow:	15	L/min
Auxiliary Gas Flow:	0.2	L/min
Nebulizer Gas Flow:	0.8	L/min
Pump Flow Rate:	1.50	mL/min
Radio Frequency (RF) Power:	1300	W

CHAPTER IV

NANOCRYSTAL ENCAPSULANTS

4.1 Introduction

The discovery of white-light emitting CdSe nanocrystals, described in Section 2.2, offers an opportunity to explore LED designs that minimize issues of color balance, self-absorption, and scattering losses that challenge current white-light LEDs. In this chapter, encapsulation of the CdSe nanocrystals in a suitable material is explored for a phosphor-conversion white LED device. The encapsulant must keep the nanocrystals from oxidizing and protect them from the heat of an excitation LED junction. In addition, an encapsulant would ideally provide good adhesion to the LED surface and inhibit nanocrystal aggregation. To find a suitable encapsulant for the nanocrystals, thirteen different materials were evaluated based on their ability to mix well with the nanocrystals, cure as a robust film, and preserve the broad spectrum white-light emission from the nanocrystals. The encapsulated nanocrystals were deposited on glass slides as thin films or in molds that could be placed atop dome-shaped LEDs for optical measurements. Figure 4.1 shows a schematic and digital photo of the white CdSe phosphor LED as envisioned in its final form.

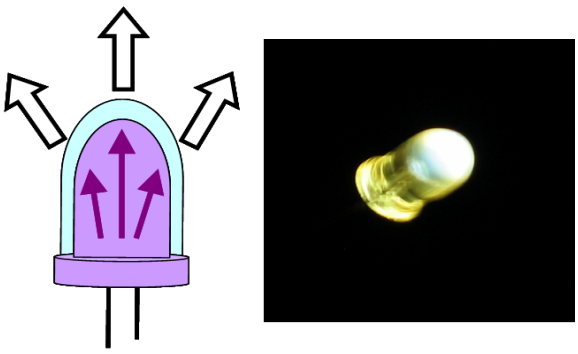

Figure 4.1. On the left is a schematic of a white-light device based on a UV LED coated with encapsulated, white-light emitting CdSe nanocrystals. On the right is an image of an actual device, where a UV LED was coated with nanocrystals and powered at 20 mA, and is showing white-light emission.

4.2 Methods

White-light emitting CdSe nanocrystals were synthesized using the method given in Section 2.4. After synthesis, the nanocrystals were placed in a toluene solution. A coating of organic ligands prevented the nanocrystals from aggregating. A number of different materials that are optically clear were used as potential encapsulants for the nanocrystals, and are listed in Table 4.1. The encapsulants were prepared according to the instructions provided by the supplier or manufacturer. The nanocrystals were added to the encapsulant while in the toluene solution and mixed thoroughly, and then the encapsulant was cured according to its directions. Most encapsulants required the mixing of two parts at a certain weight or volume ratio, though some were melted (Halowax) or suspended in a solution (biphenyl perfluorocyclobutyl, or BP-PFCB, polymer). Absorption measurements were performed as described in Section 3.1, while photoluminescence was measured in either a spectrofluorometer or an integrating sphere as described in Section 3.2.

Table 4.1: List of materials used as encapsulants for white-light emitting CdSe nanocrystals.[124]

Encapsulant Name	Encapsulant Type	Supplier
Easy Cast Castin' Craft	Epoxy Polyester	Environmental Technologies Inc.
EpoTek 301-2	Epoxy	Epoxy Technologies
510PTA-B RTVS61	Silicone Silicone	Insulcast
6100-1AB	Epoxy	Aptek Labs
EP965LVLX clear EP961 clear	Epoxy Epoxy	Resinlab/Ellsworth Adhesives
Series 40 Series 2300	Halowax Halowax	Halocarbon Prod. Corp.
Aqua Clear	Epoxy	Artmolds
TSE3033	Silicone	GE Silicones
Biphenyl-PFCB	Thermoplastic fluoro-carbon chain polymer	Tetramer Technologies, L.L.C

4.3 Encapsulant testing

To determine the encapsulant with the optimal properties, the different encapsulants were first tested not only for their ability to mix well with the nanocrystals while in solution, but also to see if they would cure as designed with the nanocrystals. The Series 40 and 2300 Halowaxes had melting points that prohibited nanocrystal encapsulation. The Series 40 wax is a liquid at room temperature, while the melting point of the Series 2300 wax (>132 ºC) is greater than the boiling point of toluene. Similarly, the EP965 and Easy Cast epoxies did not cure according to their schedule due to reactions between the epoxy hardeners and excess organics from the nanocrystal synthesis. The hardener in the polyester encapsulant oxidized the nanocrystals, which destroyed any absorbance or fluorescence. All of the other encapsulants were able to mix and cure well with the nanocrystals and allowed the nanocrystals to retain some of their original absorption and emission properties.

The fluorescence of thin films of white-light nanocrystals in several different encapsulants is shown in Figure 4.2. The other encapsulants that are not shown either had problems during mixing as mentioned before, had very low emission, and/or altered the nanocrystal emission spectrum dramatically such that a white LED device could not be achieved. The BP-PFCB polymer performed best, displaying the strongest emission without modifying the spectral shape of the nanocrystal emission. The silicone TSE 3033 resulted in half the emission intensity of the BP-PFCB polymer and a loss of some of the blue emission from the nanocrystals, especially in the peak near 450 nm.

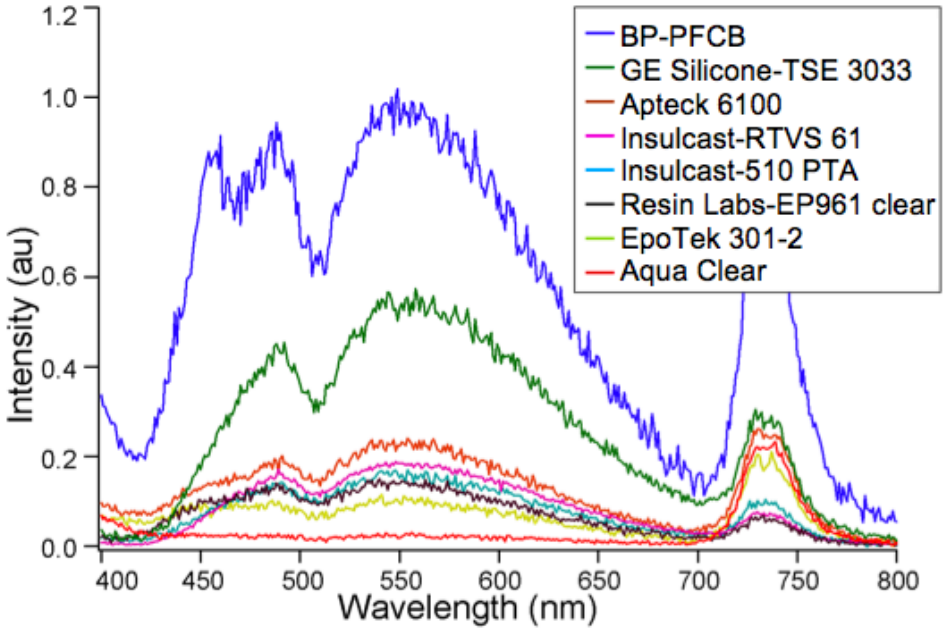

Figure 4.2: The emission from ultrasmall single-sized nanocrystals in various encapsulants. The samples were all 50 ± 3 μm thick films and at 9% weight concentration nanocrystal to polymer loading.

The cause for the difference in emission intensity among the various encapsulants is believed to be due to light scattering effects. When nanocrystals aggregate, scattering effects can become significant. The white-light fluorescence images seen in Figure 4.3

clearly show nanocrystal aggregation in some encapsulants. The silicone encapsulant RTVS61 caused the largest nanocrystal aggregates (up to 10 μm in diameter, shown in Figure 4.3a) among the three encapsulants tested, while the epoxy encapsulant EpoTek 301-2 caused smaller aggregates to form (around 1 μm in diameter, shown in Figure 4.3b). Monodisperse nanocrystal aggregation was achieved only using BP-PFCB (shown in Figure 4.3c). The data from Figures 4.2 and 4.3 suggests that aggregation of nanocrystals in the thin films is directly related to the difference in emission intensity among the different encapsulants. The scattering properties of nanocrystals are investigated and compared to larger phosphor particles in Chapter 6.

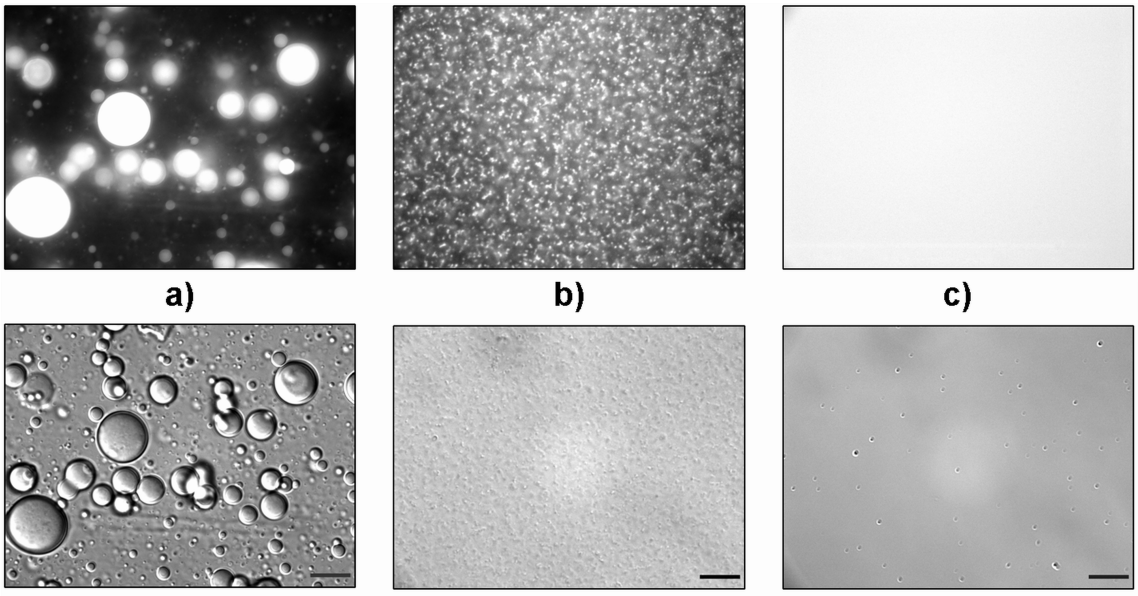

Figure 4.3: Representative white-light fluorescence (top) and bright field differential interference contrast (bottom) micrographs of encapsulated nanocrystals at 5% weight concentration loading in: **a)** RTVS61 silicone **b)** EpoTek 301-2 epoxy **c)** BP-PFCB polymer. All images were acquired with an exposure time of 5 ms, displayed with equivalent thresholds, and at the same thickness (~2 μm). The scale bars are 10 μm on all the images. The uniform fluorescence illustrated in **c)** is representative of disperse nanocrystal fluorescence in BP-PFCB and is not an artifact due to overexposure of the image.

The nanocrystals encapsulated in BP-PFCB not only exhibit the highest intensity emission spectrum, but they also, as shown in Figure 4.4, have almost identical absorption and emission spectra as exhibited in solution prior to encapsulation. This suggests that the size distribution of the nanocrystals did not change during the encapsulation process. CIE chromaticity coordinates for the sample shown in Figure 4.4 in solution (0.326, 0.342) were only slightly changed when encapsulated (0.328, 0.349), where both of these coordinates are within the limits of white light. Furthermore, the quantum yield of the nanocrystals was unaffected by the encapsulation process.

In addition to superior emission properties, nanocrystals encapsulated in BP-PFCB were more robust than the other encapsulated nanocrystal films. BP-PFCB encapsulated nanocrystal films that were heated to 190 ºC for 48 hours showed very little change in spectral characteristics. Most other encapsulated films became extremely discolored upon the same heat treatment, and the emission decreased to an almost unobservable level in all but the TSE 3033 and RTVS61 films. The BP-PFCB encapsulation that provides protection against heating is critical for devices that incorporate these nanocrystals. At the standard operating temperatures of LED junctions, nanocrystals would aggregate and sinter if not properly protected by an encapsulant.

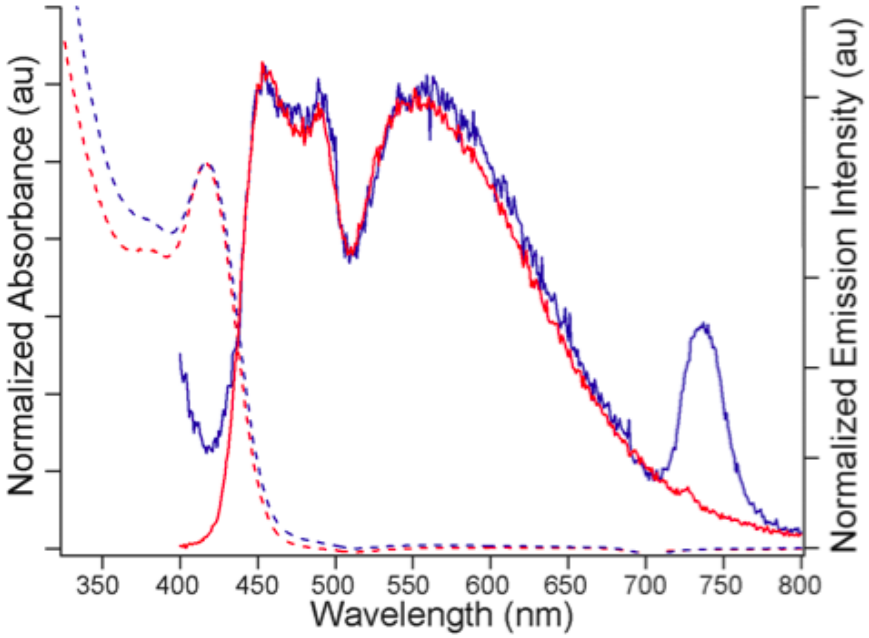

Figure 4.4: Absorbance and emission of CdSe white-light nanocrystals. The dashed lines are absorbance spectra, while the continuous lines show the emission of the nanocrystals. The red spectra are nanocrystals solvated in toluene; the blue spectra are 12% weight concentration nanocrystals in biphenyl-perfluorocyclobutyl polymer (BP-PFCB).

4.4 Absorption with BP-PFCB

Given the superior properties of the BP-PFCB encapsulant, the optical properties of films with this encapsulant were probed in more detail. First, the absorption spectra for white-light nanocrystals in BP-PFCB are shown in Figure 4.5 for 1%, 2%, 5%, and 10% concentration by weight, as well as for BP-PFCB alone. The spectrum of BP-PFCB alone shows a gradual decrease in absorption from 350 to 700 nm, suggesting that BP-PFCB could absorb some of the UV light emitted by the nanocrystals, which could lead to a distortion of their emission spectrum. The band-edge absorption peak of the white-light nanocrystals is located at 414 nm, which also can be seen in the spectra of the nanocrystals in BP-PFCB. The presence of this peak in the spectrum suggests that the nanocrystals have not grown in size after encapsulation. As discussed in Section 2.1, the

band-edge absorption wavelength is directly related to the nanocrystal size. With just 1% by weight nanocrystals in the film, the absorption spectrum is similar to the curve of BP-PFCB alone. As the concentration is increased, the level of band-edge absorption increases and more closely resembles the absorption of nanocrystals in solution, as expected. This trend is more clearly shown in the inset of Figure 4.5, where the absorbance of the same samples in addition to the absorption of the nanocrystals in solution is displayed, with the spectra normalized at the band-edge absorption wavelength. Figure 4.5 also shows that for a given concentration, the absorbance changes with wavelength. For photoluminescent LEDs based on these nanocrystal films, a change in the peak wavelength of the excitation LED could lead to changes in the emission intensity and device efficiency, which will be discussed further in Section 5.4.

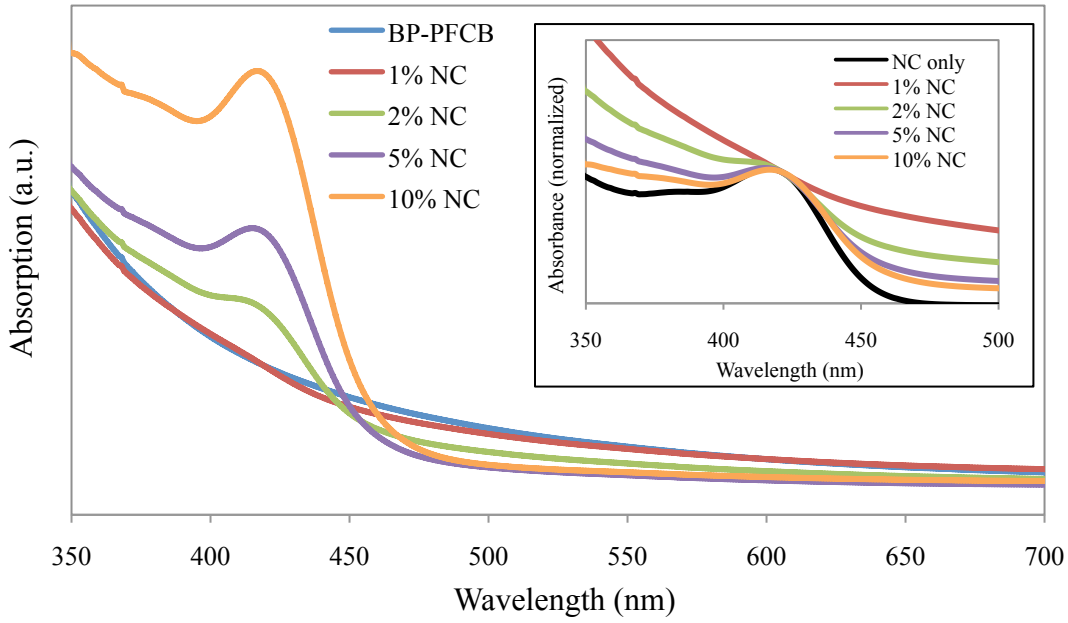

Figure 4.5: The absorption spectra of BP-PFCB alone, and 1%, 2%, 5%, and 10% by weight white-light CdSe nanocrystals in BP-PFCB. The films have a thickness of approximately 200 μm. The inset shows the absorbance for the same NC/BP-PFCB samples along with the nanocrystals used in those films in solution, normalized at the band-edge absorption wavelength.

4.5 Photoluminescence with BP-PFCB

In addition to the absorbance, the photoluminescence of BP-PFCB encapsulated nanocrystal films was also investigated, which allows for the evaluation of color quality and emission intensity. The nanocrystal concentration had a noticeable effect on the emission color, which is easily detectable by the naked eye. To demonstrate this effect, Figure 4.6 displays digital camera images of three 385 nm LEDs by themselves, along with images of 1% and 2% nanocrystals by weight in BP-PFCB on top of the three LEDs. The 1% sample has a more blueish-white emission, while the 2% sample has more of a yellowish-white emission, which is confirmed by the photoluminescence data in Figure 4.7. The emission spectra for BP-PFCB films alone and for 1%, 2%, 5%, and 10% nanocrystals by weight in BP-PFCB when excited by a 365 nm LED are shown in Figure 4.7. The emission from BP-PFCB polymer only films is strongly blue with little emission above 500 nm. As nanocrystals are added to the polymer films, the emission becomes less blue and more characteristic of the intrinsic nanocrystal emission that can be seen in Figure 2.3. With higher nanocrystal concentrations in the films, more excitation light is absorbed and thus more light is emitted by the nanocrystals. In addition, a higher concentration of nanocrystals should lead to more absorption by the nanocrystals of the blue light that is emitted by the polymer. Furthermore, it is possible that an energy-transfer process could lead to emission that is more characteristic of the nanocrystals at higher concentrations. The effect of various device parameters on the colorimetric properties is studied in more detail in Chapter 5.

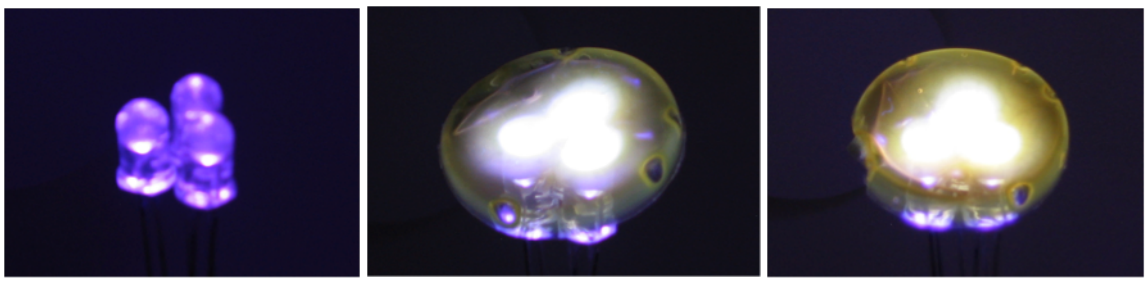

a) **b)** **c)**

Figure 4.6: Digital camera images showing three 385 nm LEDs powered at 20 mA and 4V **a)** alone and with white-light CdSe nanocrystals in BP-PFCB polymer at concentrations of **b)** 1% and **c)** 2% by weight placed on top. The different concentrations give rise to changes in emission color.

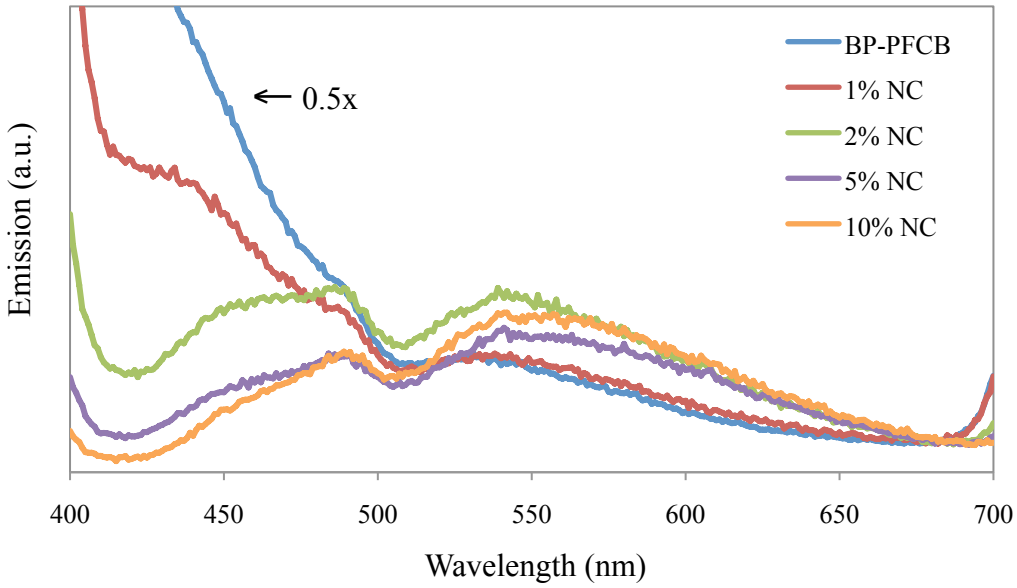

Figure 4.7: The emission spectra of BP-PFCB alone, and 1%, 2%, 5%, and 10% by weight white-light CdSe nanocrystals in BP-PFCB. The excitation source was a 365 nm LED. The BP-PFCB spectrum was multiplied by 0.5 to be shown on the same scale as the other spectra. The films have a thickness of approximately 200 μm.

While Figure 4.7 shows the spectral effect of increasing nanocrystal concentration, Figure 4.8 shows the effect of nanocrystal concentration on emission intensity. For nanocrystal loading greater than approximately 3%, changes to the

nanocrystal loading did not significantly modify the spectrum of emitted light; however, the emission intensity increases sharply as the nanocrystal loading increases from 5% to 9% weight concentration as shown in Figure 4.8. Below a concentration of 5%, there is little change in intensity, though this could be due to the limit of the detection system. Above 9%, there is a gradual increase in intensity up to 18%, which was the highest concentration tested. Note that the Insulcast RTVS61 and EpoTek 301-2 encapsulants exhibited a similar trend in changes to the emission intensity. However, their emission intensities saturated at nanocrystal concentrations of 0.36% and 0.25%, respectively. It is possible that this behavior is due to scattering resulting from nanocrystal aggregation.

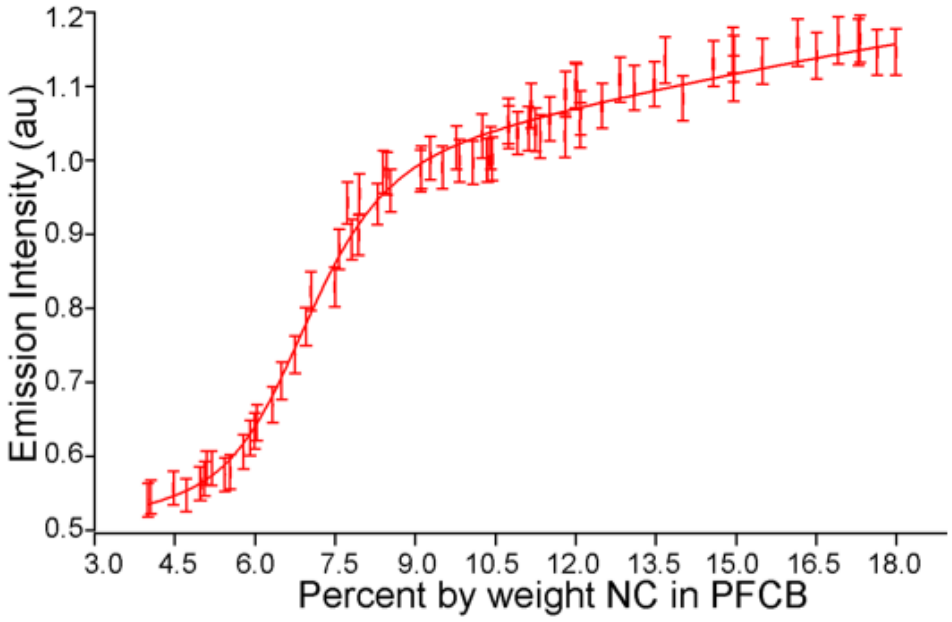

Figure 4.8: Integrated emission intensity of CdSe white-light nanocrystals in BP-PFCB vs. percent by weight loading. The line drawn is meant only as a guide for the eye.

With appropriate design, devices fabricated using BP-PFCB encapsulated nanocrystals resulted in impressive color qualities. For example, the CIE chromaticity

coordinates for a 365 nm emitting LED coated with a 1% weight concentration nanocrystal layer were (0.324, 0.322), with a measured CRI of 93. Other designs with excellent color quality are discussed in Chapter 5. The color quality of the CdSe white LEDs is superior to those of typical commercially available white LEDs. While the color qualities are superior, the luminous efficacy of CdSe white LEDs is typically only several lm/W. Although this efficacy is below that of other lighting technologies and the DOE goals for solid-state lighting, there are several areas where improvements can be made to increase the efficiency, which will be explored in Chapter 5. Briefly, the nanocrystal quantum yield and the UV LED efficiency are both near 10%, and are the main factors in the lower efficiency. Other areas of improvement can be found in using longer wavelength LEDs to reduce the Stokes energy loss, and increasing the light extraction efficiency.

4.6 Conclusions

The experiments in this chapter focused on investigating the properties of ultrasmall white-light CdSe nanocrystals when encapsulated in various materials, such as silicones, epoxies, and polymers. It was found that the emission of the films was greatly affected by the encapsulant material used. Of the thirteen encapsulants studied, only BP-PFCB was a practical option for encapsulation, creating a rugged, color-stable environment for the nanocrystals. Encapsulation in BP-PFCB allowed the nanocrystals to be combined with UV LEDs to create a potentially viable, solid-state white-light source. An increase in the concentration of nanocrystals in BP-PFCB caused a small decrease in the amount of blue emission from the device, believed to be due to self-

absorption of the nanocrystal emission. This resulted in a warmer white color at higher concentrations of nanocrystals in BP-PFCB.

The luminous efficacy of the devices was likewise affected by the nanocrystal concentration of the films. The level of UV light absorbance by the samples was shown to vary with wavelength, which causes a change in the amount of emission power and device efficiency depending on the peak wavelength of the LED. In the same way, the concentration of nanocrystals will alter the efficiency of the samples. By adding more nanocrystals to the same amount of polymer, more UV light will be absorbed by the films. Initial attempts at coating UV LEDs were successful in meeting two out of three of the DOE's goals for general illumination: CIE chromaticity coordinates (0.324, 0.322) and a CRI of 93. With the color qualities found to be superior to commercial devices, future chapters will be aimed at improving the luminous efficiency of devices to a commercially realistic value.

CHAPTER V

EFFICIENCY OF NANOCRYSTAL LEDS

5.1 Introduction

In chapter 1, it was shown that the overall device efficiency for photoluminescent devices is given by Eqns 5.1 and 5.2:

$$Efficiency = Excitation\ LED\ efficiency \times \eta_{phos} \times C_{ex} \tag{5.1}$$

$$\eta_{phos} = \eta_{abs} \times \eta_{conv} \times \frac{E_{emit}}{E_{exc}} \tag{5.2}$$

There are several methods to be investigated that could increase the efficiency of these devices. The most obvious way would be to increase the efficiency of the excitation LED. There are has been much recent effort aimed at increasing the efficiency of UV LEDs not only for their use in solid-state lighting, but for biosensing, communications, purification, and disinfection as well.[141-143] While recent reports of UV LED efficiencies in a laboratory setting have approached 40%, the LEDs used in these experiments had efficiencies between 5% and 10%. Experiments are ongoing to increase the quantum yield, but are not the subject of this dissertation. This chapter will focus on other approaches to efficiency improvements.

First, the dependence of the encapsulated nanocrystal film thickness on the absorbance and emission intensities was investigated along with the color qualities of the CdSe nanocrystal films. Thicker films should absorb more excitation light, leading to stronger emission intensity, but if the film is too thick, self-absorption may play a role and change the white light color balance. A second area of investigation was to lower the

Stokes loss by using a longer wavelength LED for excitation. Since blue LEDs are more efficient than UV LEDs, the intensity and efficiency should be greater with longer wavelength LEDs. However, any excitation light that leaks out of the device could imbalance the white-light spectrum and thus worsen the color quality. The final approach examined the use of dielectric mirrors to increase the extraction efficiency by redirecting unabsorbed excitation light, as well as white light emitted by the nanocrystals, towards the LED die.

5.2 Methods

The CdSe nanocrystals used in this work were synthesized and purified according to the method described in Section 2.4, and solvated in toluene. The white-light emitting nanocrystals were mixed with BP-PFCB in solution, dropcast onto glass slides, and cured at 100 ºC until hardened. Based on prior nanocrystal loading experiments in BP-PFCB,[124] a 10% weight concentration loading was chosen. A large range of film thicknesses from approximately 5 - 1200 μm was produced by using different volumes of dropcast solution on the glass slides. Absorbance, photoluminescence, and thickness measurements were performed according to the methods in Section 3.1, 3.2, and 3.3, respectively.

5.3 Film thickness

The emission characteristics of polymer-encapsulated white-light CdSe nanocrystal films are investigated in a configuration mimicking that of a typical phosphor LED, where the nanocrystal film is placed between the excitation source and the detector.

Previous work has shown that the thickness of a film with encapsulated nanocrystals and other phosphors can have a significant effect on emission intensity[144-146] as well as color characteristics.[146-148] For phosphor-conversion, nanocrystal-based LEDs, ideally a very thin nanocrystal film would be applied to the outside of a commercial UV LED, or the nanocrystals in the encapsulant would replace the commercial clear epoxy bulb and encase a UV LED die. In either case, it would be desirable to have a film thickness sufficient to absorb all of the UV light without affecting the emission intensity or color qualities. To this end, this work experimentally analyzes the influence of film thickness on the absorbance, emission intensity, and color qualities (CRI, CIE coordinates) of the white CdSe phosphor LED.

Figure 5.1 shows the wavelength-dependent absorbance of several CdSe nanocrystal films. As expected, the absorbance increases as the film thickness increases. Moreover, for wavelengths below 400 nm, the absorbance is nearly constant for a given film thickness. The fraction of light absorbed at the band-edge absorption wavelength (~415 nm) is plotted in the inset of Figure 5.1 as a function of film thickness. In accordance with the Beer-Lambert Law, the absorbance increases linearly with film thickness until the absorption reaches ~100%, which occurs for film thicknesses above 150 μm. Hence, it is expected that for CdSe phosphor LEDs, the thickness of the encapsulated films need not be greater than ~150 μm.

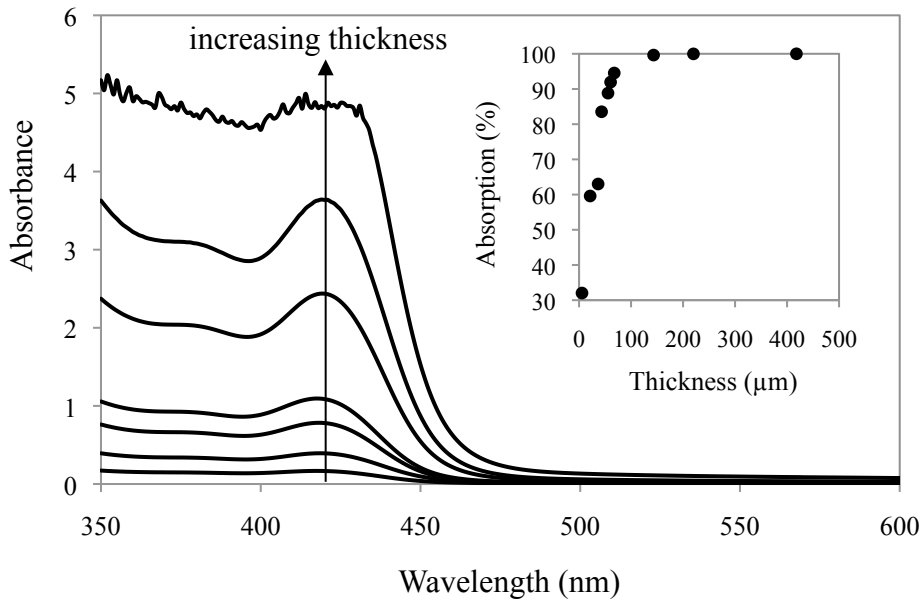

Figure 5.1: The absorbance of nanocrystal-polymer films as a function of wavelength at a few film thicknesses, with the arrow pointing in the direction of increasing film thickness (6 μm, 21 μm, 43 μm, 61 μm, 143 μm, 220 μm, and 418 μm). The inset shows the absorption (in percent) at the band-edge absorption peak (approximately 415 nm) as a function of film thickness.

The nanocrystal films were first excited using UV laser lines (350-355 nm) to analyze their intrinsic light emission properties without confounding excitation light. As seen in Figure 5.2, the thinnest films had a mostly balanced but weaker emission spectrum overall than the thicker samples. As the thickness is increased, more blue light gets re-absorbed by the film until, with the thickest film, the emission becomes somewhat yellow. Additionally, the emission intensity begins to decrease with the thickest films, which is also attributed to re-absorption by the nanocrystals in the film.

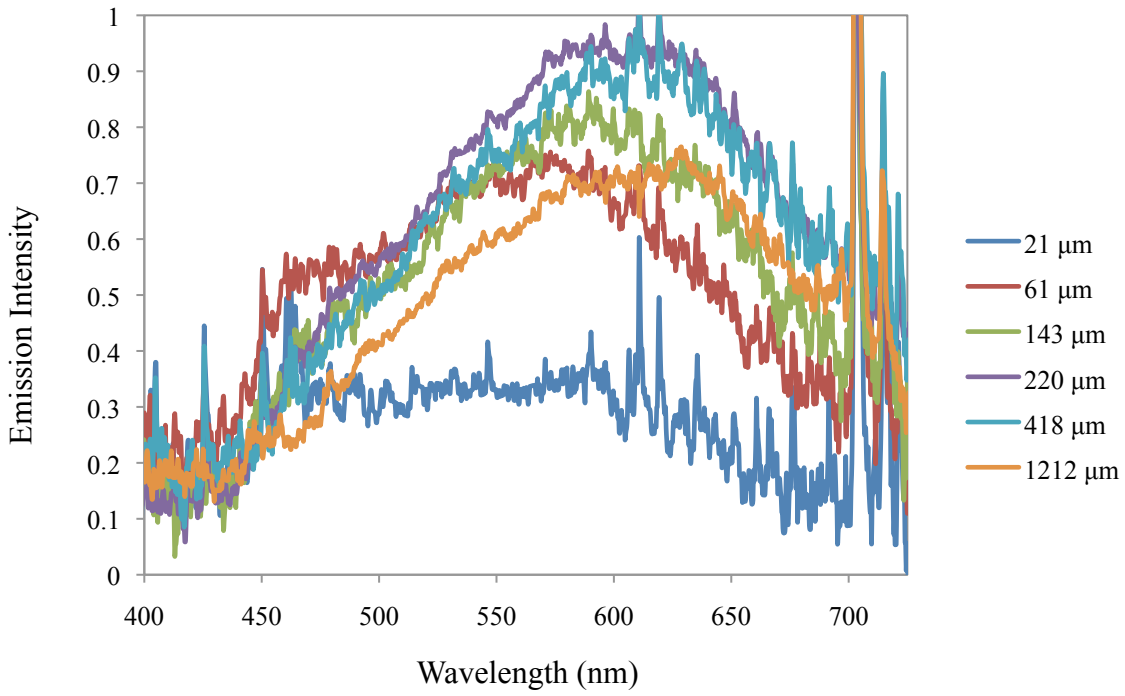

Figure 5.2: The photoluminescence spectra of nanocrystal-polymer films excited by a UV laser at a few different film thicknesses. The two spikes near 700 nm are the second-order peaks from the two main laser lines.

This effect is more clear in Figure 5.3, which shows the normalized luminous flux as a function of thickness. The data indicate that the largest emission intensity was achieved with films in the 200 µm range. Thus, for films below this thickness, the emission intensity and absorbance both increase linearly with thickness. However, due to self-absorption, the emission intensity begins to decrease above 200 µm. Though self-absorption for this material is lower than for the larger, single-color nanocrystals, when they are used at high concentrations and in very thick films the absorption in the yellow and red regions of the spectrum can become significant. For example, the ~ 400 µm film absorbed 5% of the incident light at 550 nm while the ~ 1200 µm film absorbed nearly 50%.

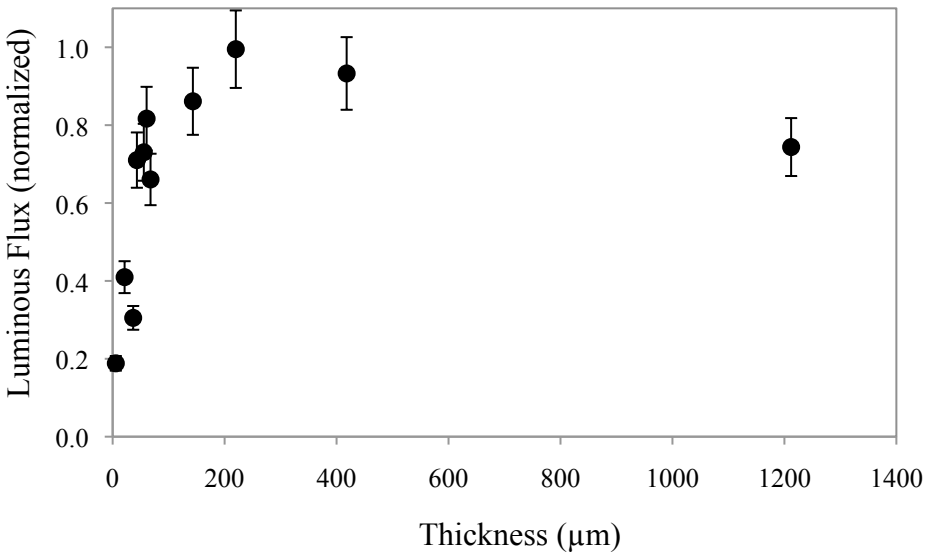

Figure 5.3: The normalized luminous flux of nanocrystal-polymer films excited by a UV laser as a function of film thickness.

5.4 Excitation wavelength

Since these films are designed to be used as the phosphor layer of a white LED, any excitation light that leaks through the film must be considered in the overall device emission properties. Thus, the photoluminescence of the same films was then measured using different wavelength LEDs to determine which LED resulted in optimal emission properties. Figure 5.4 displays the emission intensity as a function of wavelength for a few film thicknesses using a 365 nm LED for excitation. Figure 5.5 is a photograph of the emission of nanocrystal-polymer films excited by a 365 nm UV lamp at a range of film thicknesses, with increasing thickness from left to right. The luminous flux of the films, excited by different wavelength LEDs and normalized to the output power of the LED alone, can be seen in Table 5.1. The films were placed on top of the LEDs to simulate a typical device configuration. As was seen with the laser excitation, the emission intensity increases linearly with thickness and then drops off for larger

thicknesses. Whereas with the laser excitation the optimal thickness was 200 μm, the highest emission intensity using 365 nm and 385 nm LED excitation was near 150 μm. This is likely due to LED excitation light that is not absorbed by the film and thus contributes to the overall luminous flux of the device. This light is not converted by the nanocrystals, which leads to a higher luminous flux than the films that absorb all of the excitation light. The effect is even more apparent for the nanocrystal films with 405 nm LED excitation, as the highest emission intensity occurs for films < 50 μm thick.

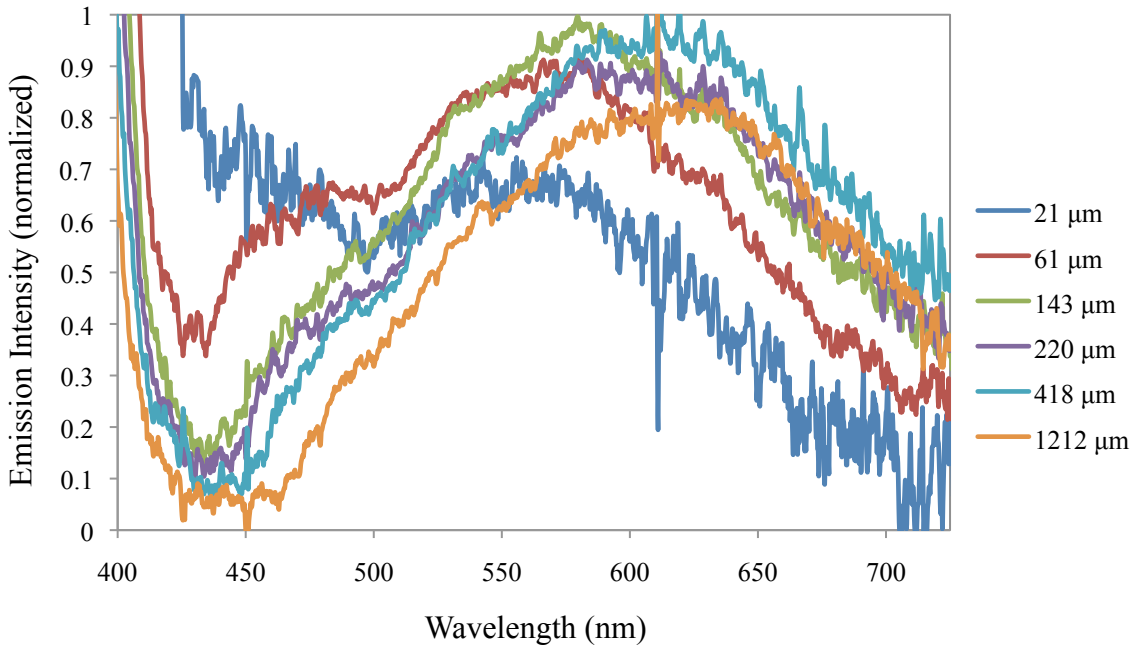

Figure 5.4: The photoluminescence spectra of nanocrystal-polymer films excited by a 365 nm LED at a few different film thicknesses. The emission near 400 nm is a result of LED excitation light that has either reflected off of or leaked out the side of the glass slide.

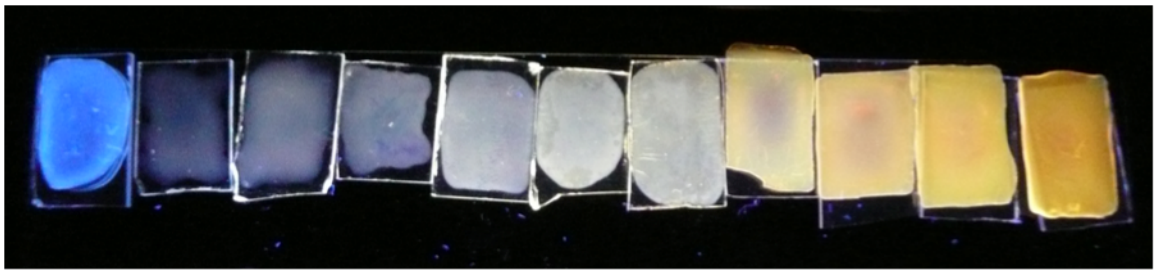

Figure 5.5: The emission of nanocrystal-polymer films excited by a 365 nm UV lamp at a range of film thicknesses. The film on the far left is a BP-PFCB only film, with the rest at increasing thicknesses from approximately 5 – 1200 μm from left to right.

Table 5.1: The luminous flux (in lumens) of nanocrystal-polymer films (10% loading) excited by different wavelength UV LEDs at various film thicknesses divided by the output power of the UV LED alone (in W), as well as the corresponding CIE chromaticity coordinates and CRI. A value of zero in the CRI column indicates that the spectrum is too unbalanced to be considered white light.

Thickness (μm)	365 nm			385 nm			405 nm		
	lm/W	CIE	CRI	lm/W	CIE	CRI	lm/W	CIE	CRI
6	2.7	0.24,0.17	0	3.1	0.21,0.09	0	2.2	0.18,0.02	0
21	4.5	0.28,0.26	88	4.1	0.23,0.14	0	4.2	0.19,0.06	0
61	4.9	0.35,0.37	86	5.1	0.31,0.28	82	3.8	0.23,0.13	0
143	5.0	0.40,0.42	84	5.3	0.38,0.38	82	3.1	0.31,0.26	74
220	4.5	0.41,0.42	88	4.7	0.39,0.38	87	3.1	0.35,0.33	90
418	4.7	0.44,0.43	88	4.5	0.41,0.39	86	2.6	0.37,0.34	88
1212	3.9	0.46,0.45	86	4.1	0.42,0.39	84	2.5	0.38,0.34	86

In addition to the emission intensity, the color characteristics of the emitted light must be taken into consideration when determining the most appropriate parameters for the nanocrystal phosphor LEDs. Table 5.1 also shows the CIE coordinates and CRI for the range of film thicknesses when excited with the various UV LEDs. As expected, when the wavelength of the LED is increased for the same thickness, the emission becomes more blue as the excitation light passing through the films is at longer

wavelengths. Also, as the film thickness is increased for the same wavelength LED, the emission changes from blue-white to pure white and eventually yellowish-white due to self-absorption.

The best device characteristics resulted from films in the 60-140 μm range when excited with a 365 nm or 385 nm LED. While the luminous efficacy of these devices is near 1 lm/W, increases in the nanocrystal quantum yield and UV LED efficiency (both typically ~5-10% in these measurements) could significantly improve the efficiency of these devices. Although not addressed in this work, photostability is an important consideration for the encapsulated nanocrystal films. Non-shelled CdSe nanocrystals have been shown to degrade via the photo-oxidation of surface selenium atoms[149] unless the nanocrystals are kept in an inert atmosphere.[150] Thus, it will be important for future devices to be fabricated under inert conditions and for the nanocrystal LEDs to be packaged in a material that is impermeable to oxygen.

5.5 Dielectric mirror simulations

The basic design of an LED was for many years based on planar shapes. However, the large refractive index differences between semiconductors and epoxy, silicone, or air limits the light extraction efficiency for planar surfaces to just a few percent because of total internal reflection. A large efficiency increase can be realized by improving the light extraction in LEDs, and as a result many different methods for doing this have been explored, as detailed in Section 1.6.4. Unfortunately, most of these methods are only directly applicable for monochromatic light sources. In addition, the

complexity of some of the techniques to increase the light extraction makes them not ideal for use in commercial devices due to cost concerns.

To increase the extraction efficiency of the nanocrystal-based LEDs for all wavelengths in the visible region of the spectrum, the use of dielectric thin film mirrors was explored. The basic idea of this approach is illustrated in Figure 5.6. Two thin film dielectric mirrors are incorporated, one on top of the UV LED die (M1) and the other on top of the nanocrystal phosphor layer (M2), to (1) enable a larger fraction of the white light to escape the device, (2) prevent UV photons from escaping the device, and (3) allow UV photons not initially converted to white light to continue to interact with the CdSe nanocrystals. As shown in Figure 5.6, mirror M1 with high reflectance throughout the visible and high transmission in the UV is deposited onto the UV LED die. UV excitation light passes through the thin film structure to enable absorption and conversion into white light by the CdSe nanocrystals. M1 also reflects any white light propagating towards the die and directs it out of the device, eliminating a major source of loss (i.e., re-absorption) in solid-state lighting devices. M2 with high reflectance in the UV region and high transmission in the visible region is deposited on the nanocrystal layer. UV light that would otherwise escape the device is reflected back towards the nanocrystals for additional excitation, increasing the efficiency of the device and also preventing harmful UV radiation from being emitted. M2 is also designed such that visible light will be able to pass through the thin film structure.

Simulations of these mirror designs were performed to assess the viability of this approach for increasing white-light LED efficiency. Monte Carlo simulations have been previously performed to study the conversion efficiency of UV to white light and

extraction of white light in a system consisting of scattering, micron-sized red, yellow, and blue phosphors dispersed beneath a multilayer stack omnidirectional mirror.[151] It is anticipated that these ultrasmall nanocrystals would have significantly reduced scattering and thus took a more straightforward approach for this analysis, which includes design criteria for the dielectric mirrors.

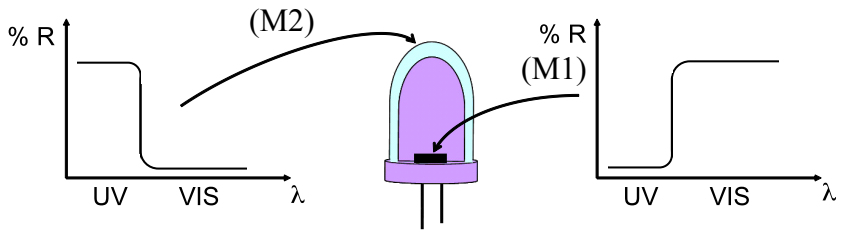

Figure 5.6: Structure of a white-light NC-based LED device consisting of a UV LED externally coated with encapsulated ultrasmall CdSe nanocrystals. A mirror with high reflectance in the visible region is deposited on top of a UV LED die, while a mirror with high reflectance in the UV region is deposited on top of a layer of encapsulated nanocrystals.

Theoretical calculations were done to evaluate the feasibility and potential for light extraction improvement by the different designs.[152] Simulations were carried out using Matlab on a dielectric, thin film mirror/filter design, with the code given in Appendix C. The reflectance of the thin film design was calculated using transfer matrix theory[153,154] as a function of wavelength for different numbers of periods of alternating, dielectric layers. The structure of the mirror is quarter-wavelength stacks of alternating quarter-wavelength layers of SiO_2 ($n_1 = 1.46$) and HfO_2 ($n_2 = 2.00$), with a substrate of SiO_2 ($n_s = 1.46$). These materials were selected for their low absorbance in the UV and visible regions. A graphic of this design can be seen in Figure 5.7. The reflections from each of the interfaces in the structure will interfere constructively, which leads to a high

reflectance over a chosen wavelength range. The wavelength is selected by ensuring that the thickness t of the layers is as given in Eqn 5.3:

$$t = \frac{\lambda_0}{4n} \tag{5.3}$$

where n is the index of refraction and λ_0 is the center wavelength of the desired spectral region of high reflectance. Another design that was simulated was a chirped mirror structure, as seen in Figure 5.8. Instead of keeping the center wavelength and hence thickness of the two layers the same throughout the depth of the mirror, the center wavelength is varied, and layers with varying thickness are formed, to achieve a larger reflectance bandwidth.

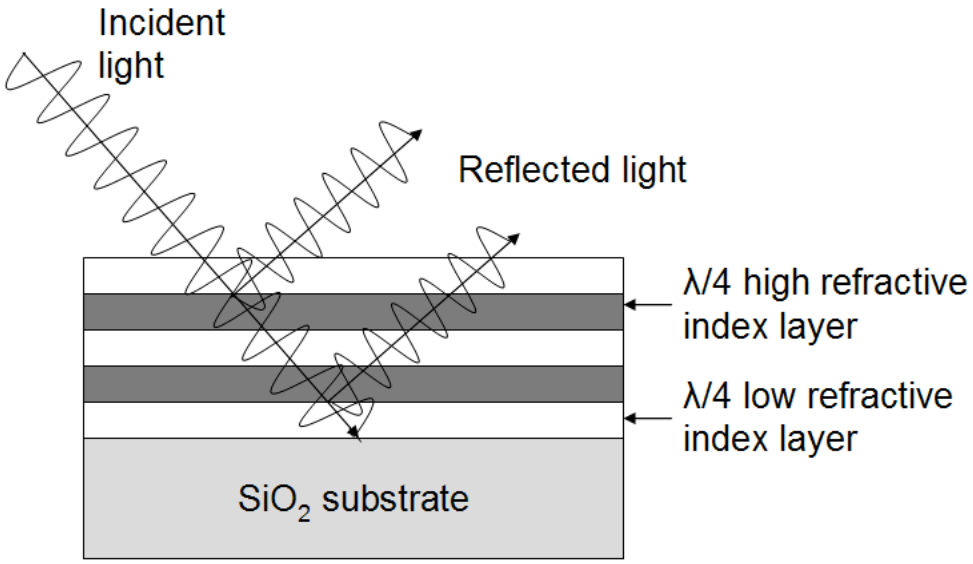

Figure 5.7: Illustration of the design of a dielectric mirror, showing alternating low and high refractive index layers each with λ/4 thickness. While reflection occurs at all interfaces, only two representative reflected light rays are shown for simplicity.

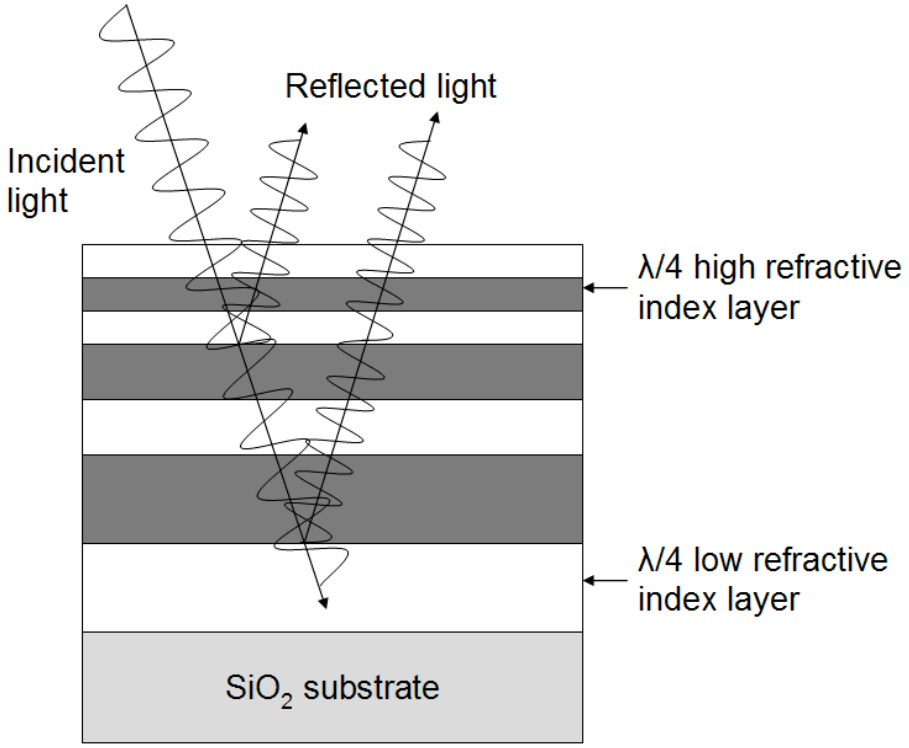

Figure 5.8: Illustration of the design of a chirped mirror with alternating low (SiO_2) and high (HfO_2) refractive index layers. The λ/4 thickness of each layer is varied throughout the structure as the design wavelength for high reflectance is varied to obtain a larger reflection bandwidth. While reflection occurs at all interfaces, only two representative reflected light rays are shown for simplicity.

Additionally, the simulations were performed for different angles of incidence to determine the effect on the reflectance. As the angle of incidence increases, the reflectance stopband shifts to shorter wavelengths.

5.5.1 Single dielectric mirror

To investigate the feasibility of using a HfO_2/SiO_2 mirror stack for the white-light nanocrystal-based LED devices, simulations were first carried out for a basic mirror structure for both the UV (M2) and visible (M1) ranges. Figure 5.9 shows the reflectance for a single dielectric mirror centered at 365 nm using five, ten, and fifteen periods of low

and high index layers. The use of only five periods may not be sufficient for M2 both due to the lack of a sharp long wavelength reflectance stopband edge that allows some blue light to be reflected and its slightly lower peak reflectance in the UV. In general, as the number of periods is increased, the percentage of incident light that is reflected also increases, such that stacks with greater numbers of periods have higher peak reflectance and sharper stopband edges. Using ten or fifteen periods results in a mirror with the necessary characteristics to prevent UV photons from escaping the device and maintain a relatively high transmission in the visible range, which allows white light from the nanocrystals to be emitted out of the device.

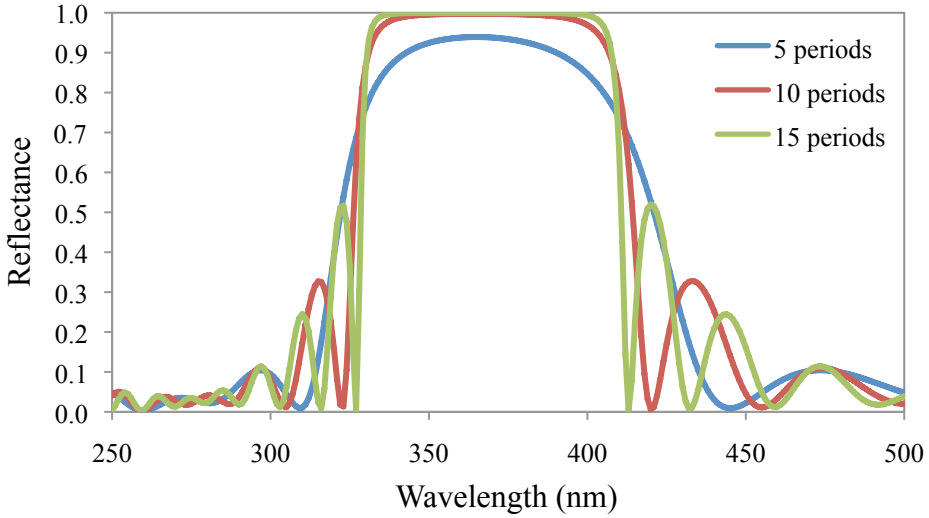

Figure 5.9: Reflectance of a single HfO_2/SiO_2 mirror, with a center wavelength of 365 nm and five, ten, or fifteen periods of low and high-index layers. With greater than ten periods, this mirror is suitable for M2.

Figure 5.10 shows the reflectance for a single mirror centered at 550 nm for five, ten, and fifteen periods. While the mirrors with ten and fifteen periods have very high peak reflectance near 550 nm, the reflectance bandwidth of 125 nm (high reflectance

from 500-625 nm) is too narrow to cover the entire visible region. Hence, this simple mirror stack design is not sufficient for M1. To increase the reflectance bandwidth, either using materials with a larger refractive index contrast or a more complex mirror structure is needed. Due to the limitation of available materials that do not absorb light in the UV or visible region and are compatible with growth in a single instrument, a more complex structure for the visible mirrors was investigated.

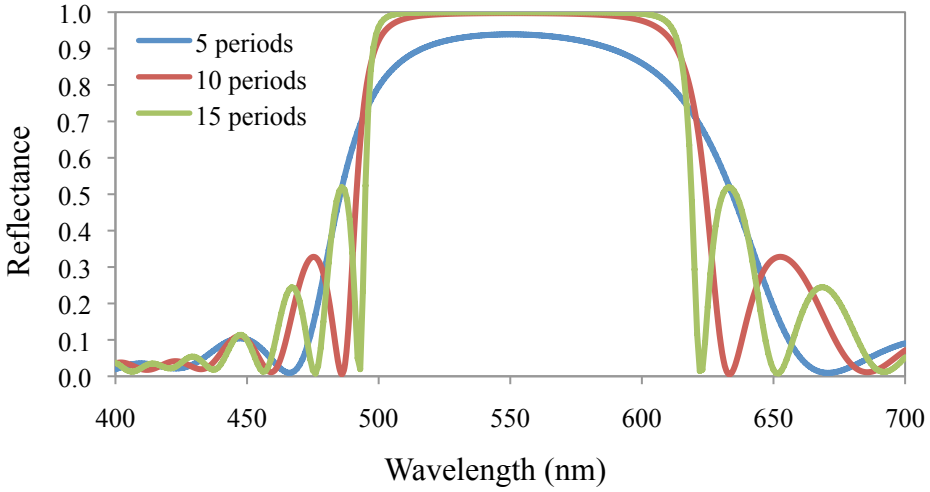

Figure 5.10: Reflectance of a single HfO_2/SiO_2 mirror, with a center wavelength of 550 nm and five, ten, or fifteen periods of low and high-index layers. This mirror is not suitable for M1 due to insufficient bandwidth.

5.5.2 Multiple dielectric mirror stacks

The next set of simulations was carried out for a structure based on mirrors that are stacked on top of each other. By stacking two or more mirrors, the reflectance bandwidth can be increased to span more of the visible range so that the balanced white light emitted by the CdSe nanocrystals can be directed out of the device, which is a necessary requirement for M1. The reflectance for two and three stacked mirrors is shown in Figures 5.11 and 5.12, respectively. Again, the reflectance is calculated using five, ten, and

fifteen periods of HfO_2 and SiO_2 layers. As the number of periods is increased, the peak reflectance of each mirror increases and the reflectance stopband squares off, as shown in previous simulations. Thus, for greater than ten periods, the reflectance bandwidths of each mirror overlaps to ensure a continuous spectral region of high reflectance. Stacking two mirrors centered at 490 nm and 610 nm results in a bandwidth of about 225 nm (450-675 nm), while three mirrors centered at 450 nm, 550 nm, and 650 nm gives a bandwidth of 325 nm (400-725 nm) and covers nearly the entire visible spectrum. Therefore, to have high reflectance throughout the visible region, these simulations suggest that at least three stacked mirrors with ten periods of HfO_2 and SiO_2 layers per mirror are needed, resulting in more than sixty deposited layers.

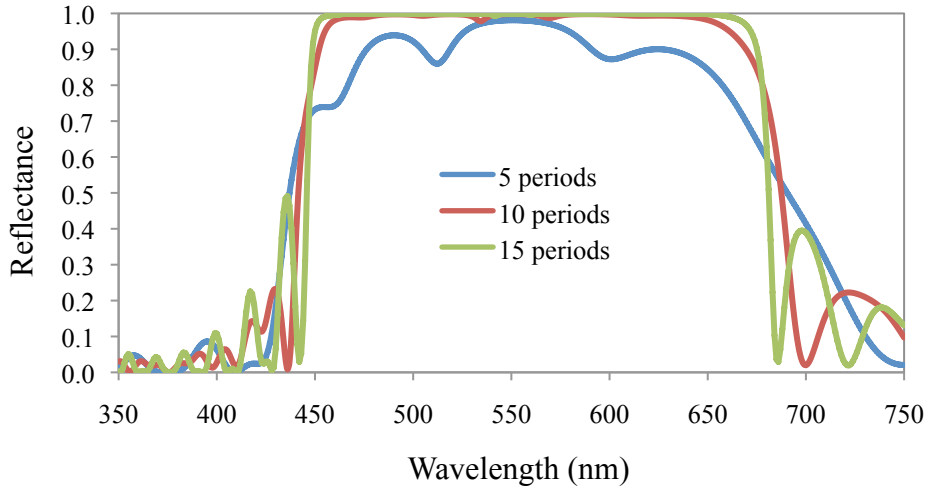

Figure 5.11: Reflectance of two stacked HfO_2/SiO_2 mirrors, centered at 490 nm and 610 nm with five, ten, or fifteen periods of low and high-index layers. These two mirrors are not sufficient to produce high reflectance across all visible wavelengths.

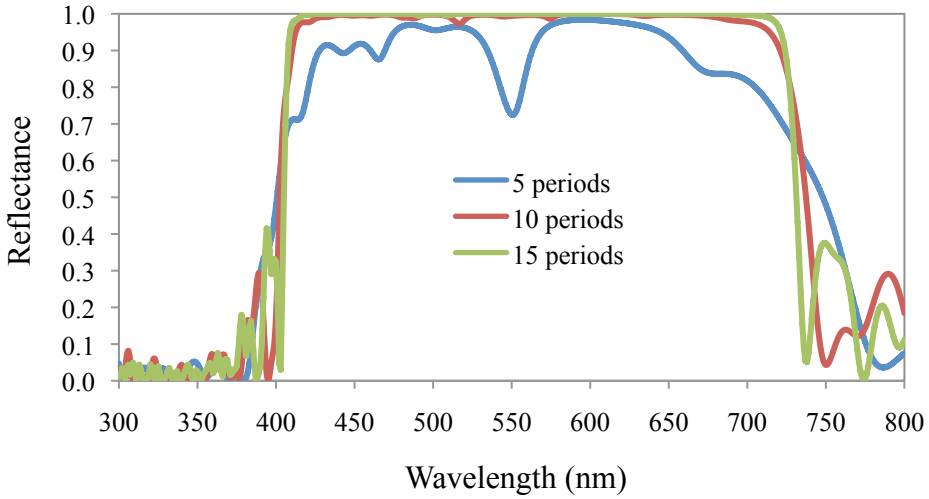

Figure 5.12: Reflectance of three stacked HfO_2/SiO_2 mirrors, centered at 450 nm, 550 nm, and 650 nm with five, ten, or fifteen periods of low and high-index layers. With greater than ten periods in each of the three mirrors, the resultant reflectance bandwidth is sufficient to uniformly reflect all visible wavelengths. This design would be suitable for mirror M1.

5.5.3 Chirped Mirrors

A third set of simulations was performed on a device structure known as a chirped mirror, which is commonly used as a laser mirror. The chirped mirror structure is based on the idea that the designed center reflection wavelength is not constant, but is varied so that a larger reflectance bandwidth can be obtained. An illustration of this type of structure was displayed earlier in Figure 5.8. It is similar in design to the stacked mirror structures investigated earlier, but with both a smaller increment between center reflection wavelengths and a smaller number of periods designed for each wavelength. The results of calculations based on this chirped design can be seen in Figures 5.13 and 5.14. The reflectance was calculated for a center wavelength increment of 5 nm and one period at each increment starting with 450 nm and ending at 700 nm, 10 nm and one period, and 10 nm and two periods (Figure 5.13), as well as an increment of 20 nm and

one, two, three, or four periods at each increment (Figure 5.14). Even with only a few periods at each mirror wavelength, the overall reflectivity is very high and the reflection bandwidth can be easily tuned, making this an attractive design. These structures will require at least fifty total layers of HfO_2 and SiO_2 to be deposited to achieve the necessary reflectance, which is slightly less than the amount required for the stacked mirror designs. Further optimization of the design of these chirped mirrors could lead to a structure that requires even fewer deposited layers while maintaining their high reflection throughout the visible region.

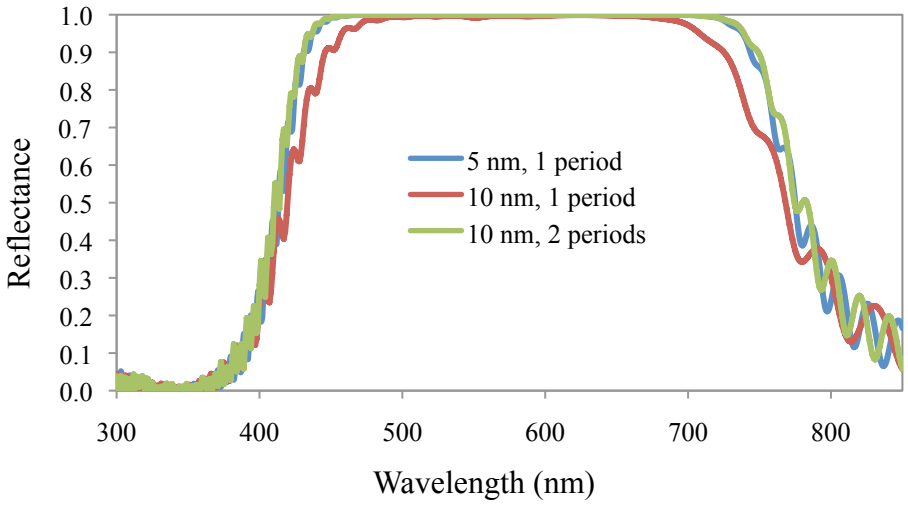

Figure 5.13: Reflectance of chirped HfO_2/SiO_2 mirrors with an increment of 5 nm and one period, 10 nm and one period, and 10 nm and two periods at each increment. These mirrors are suitable for M1.

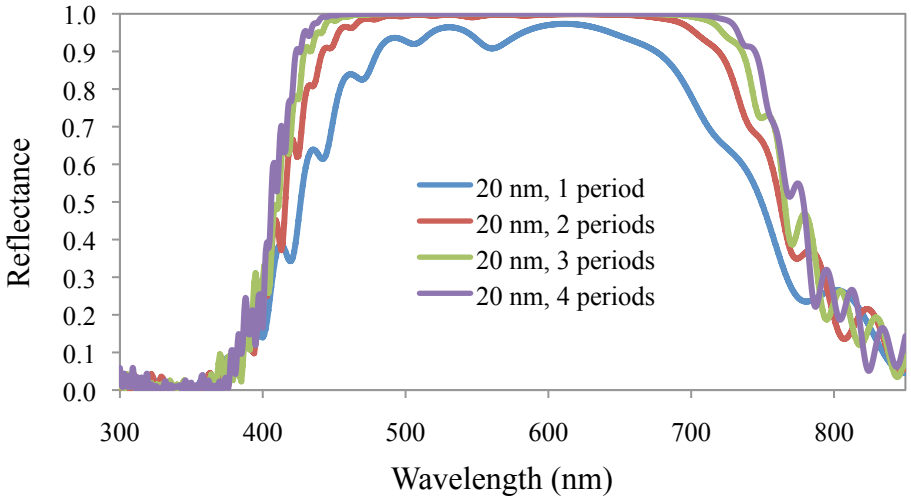

Figure 5.14: Reflectance of chirped HfO_2/SiO_2 mirrors with an increment of 20 nm and one, two, three, or four periods at each increment. For greater than one period, these mirrors are suitable for M1.

5.5.4 Light at non-normal incidence

One challenge that is faced by using dielectric mirrors is their behavior across a wide range of incident angles. The reflectance stopband shifts to shorter wavelengths as the incident angle is increased. Therefore, it is possible that a mirror designed to reflect a particular wavelength at normal incidence will transmit that wavelength at large incident angles. To study the extent of this issue with these mirror designs, the reflectance as a function of incidence angle was also calculated and is shown in Figures 5.15 and 5.16. Figure 5.15 shows the reflectance bandwidth changes for a single UV mirror centered at 365 nm with ten periods, while Figure 5.16 shows the effects for the visible, chirped mirror design with an increment of 20 nm and three periods at each increment.

These simulations show that above 30°, the reflectance bandwidth shifts would compromise the white-light LED device performance. The UV mirror designed to reflect a 365 nm LED does not have high reflectance at this wavelength for high incident angles.

Thus, UV photons incident on M2 at these large angles of incidence would escape from the device. In addition, the chirped, visible mirror will begin to have a high reflectance above 30° at 365 nm, causing UV excitation light at higher incident angles to be reflected back towards the LED die before reaching the nanocrystals. These reflected UV photons will be reabsorbed by the die and lost instead of reaching the nanocrystal layer where it can be converted to white light, lowering the overall device efficiency. For general lighting applications for which highly directional light is not a requirement, epoxy domes can be designed to limit the excitation light to near-normal incidence at M2. In this case, scattering from the phosphor layer would be the main cause of higher incident angles. As shown in Chapter 6, based on Mie theory, there will be minimal scattering from the 1.5 nm CdSe nanocrystals at near-UV and visible wavelengths. Thus, the design of M2 should be sufficient to achieve higher device efficiency. For M1, the loss of red light reflection at higher incident angles will be problematic, as well as the higher reflectance for UV photons trying to pass through M1. One potential solution is to only coat the base of the UV LED outside of the region taken up by the UV die. Since the die size is small compared to the LED size, only a small fraction of the visible photons would be reflected towards and absorbed by the die. Outside of the die region, the reflection of UV photons at higher incident angles would be favorable, as it would enable additional nanocrystal excitation. The only design criterion is to ensure that the mirror reflects red light at higher incident angles (i.e., broaden the reflectance stopband).

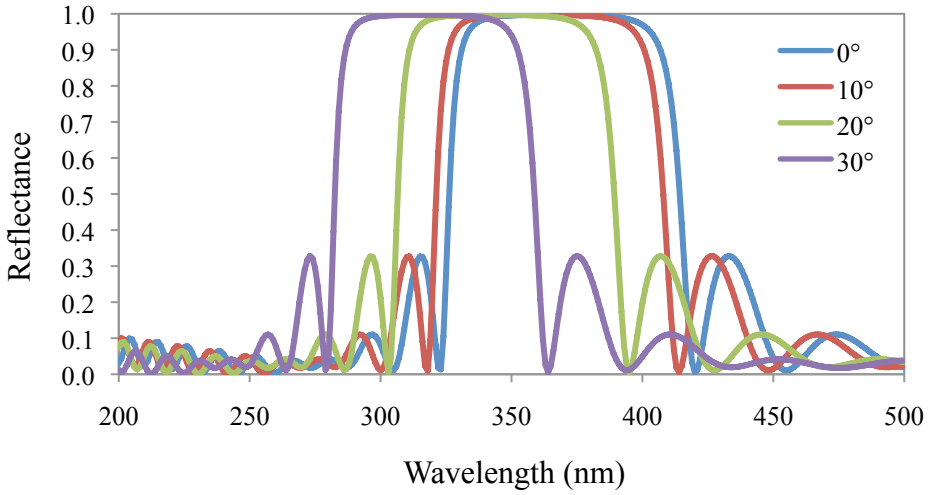

Figure 5.15: The reflectance of a single HfO_2/SiO_2 dielectric mirror, having a center wavelength of 365 nm and with ten periods of low and high refractive index layers for 0°, 10°, 20°, and 30° angles of incidence.

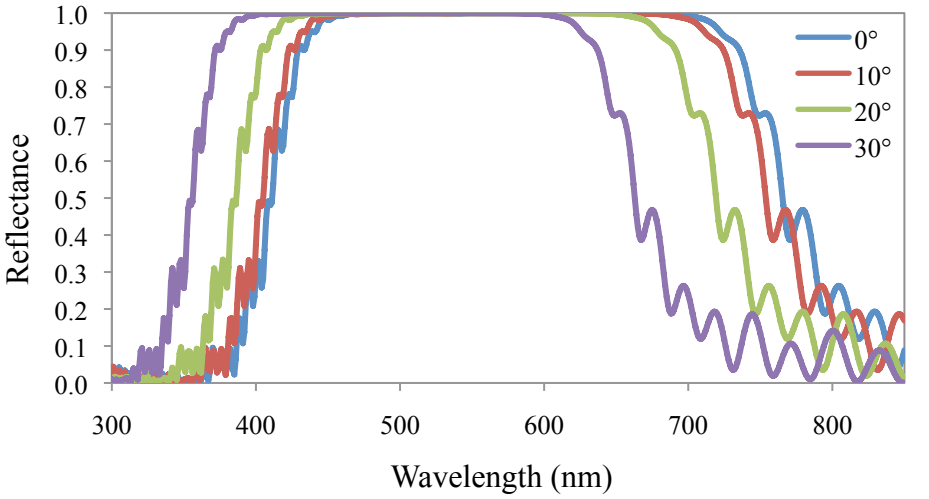

Figure 5.16: The reflectance of a chirped HfO_2/SiO_2 dielectric mirror, starting at 450 nm and ending at 700 nm with an increment of 20 nm and three periods of low and high refractive index layers at each increment for 0°, 10°, 20°, and 30° angles of incidence.

5.6 Conclusions

The thickness of white CdSe nanocrystal phosphor films and choice of LED excitation wavelength play significant roles in the overall power and color quality of nanocrystal phosphor LEDs. Films that are too thin do not absorb the majority of the LED excitation light, compromising the emitted white light power and unbalancing the white light spectrum. Films that are too thick suffer from nanocrystal self-absorption, which compromises both the color quality and emitted power. It was found that the nanocrystal film absorbance approached 100% and the emission intensity was maximum for film thicknesses near 150 μm when excited via 365 nm and 385 nm LEDs.

While these films exhibited good white light color quality (CRI > 80, CIE coordinates near pure white), slightly thinner films resulted in an emission color even closer to pure white light. While the overall trends will remain the same, ongoing research efforts to increase the quantum efficiency of these nanocrystals may result in different optimal film thicknesses or excitation LED wavelengths. For example, a higher weight concentration concentration of CdSe in BP-PFCB polymer could be used to improve the emission intensity. In doing this, the optimal thickness would likely change due to increased absorbance at the same thickness as well as increased re-absorption of the nanocrystal emission, altering the color characteristics.

The potential for using thin film mirrors and longer wavelength excitation LEDs as a means to increase the efficiency of ultrasmall CdSe nanocrystal-based white-light LEDs has also been studied. While a single dielectric mirror with at least ten periods was found to be suitable for M2, a single mirror or two stacked mirrors of HfO_2/SiO_2 did not possess a wide enough reflection bandwidth to cover the entire visible region. Mirror M1

will require either three stacked mirrors or a chirped mirror design. Since the chirped mirror has a bandwidth that can be easily tuned and a design that needs fewer deposited layers than stacking three mirrors, it was found to be the more attractive option for M1. By optimizing the design of dielectric thin film mirrors and increasing the absorption efficiency of CdSe nanocrystals in devices with more efficient blue excitation LEDs, higher quality solid-state lighting sources can be anticipated.

CHAPTER VI

SCATTERING PROPERTIES OF NANOCRYSTALS AND PHOSPHORS

6.1 Introduction

In traditional phosphor-conversion white-light LEDs, the size of the phosphor particles is on average several microns in diameter. Through the use of Mie scattering theory, it can be shown that for the visible and near-UV regions of the spectrum, the scattering coefficient increases with increasing particle size. For white-light LEDs with micron-size phosphor particles, the amount of scattering is significant and results in a reflectance of up to 50% for the blue excitation light. This reflected excitation light is then re-absorbed by the blue LED die, and is thus a major source of loss for these types of devices.

Because the scattering coefficient decreases with decreasing particle size, nanometer-size particles scatter very little compared to micron-size particles. By utilizing nano-size phosphors, the extraction efficiency will then be much higher, and is an approach that is currently under investigation.[155-157] The problem with this approach is that the quantum yield of the phosphor is decreased due to nonradiative losses attributed to surface states. White-light emitting CdSe nanocrystals, however, have a high quantum yield and at the same time should scatter very little, keeping the extraction efficiency high.

To this end, the use of semiconductor nanocrystals in optoelectronic devices such as solar cells[158,159] and LEDs[105,106,111,114] has shown great promise in recent years. As

nanocrystal use becomes more widespread, it is important that all of their properties be measured precisely to better understand their behavior in devices. One of these values, the extinction coefficient or molar absorptivity, is important because it determines the amount of light absorbed by a sample. Despite its importance, it has been less rigorously documented than other nanocrystal properties.

Accurate knowledge of the extinction coefficient allows the amount of light absorbed by a sample, such as a nanocrystal thin film for a solar cell or an LED, to be calculated. This value is critical to the design and simulation of nanocrystal-based devices. As will be shown later, differences in the extinction coefficient between this work and previous research were as high as a factor of 4 for a nanocrystal diameter of 2 nm, which would lead to a difference in the absorbance of the same factor of 4. Clearly, it is crucial that the extinction coefficient for these nanocrystals be calculated as accurately as possible.

In this chapter, the scattering properties of CdSe nanocrystals will be calculated and compared to common, larger phosphor particles. The theoretical results will then be verified with experimental data of thin films of nanocrystals. Finally, an accurate curve of the extinction coefficient of CdSe nanocrystals as a function of their diameter will be established and compared to previous reports.

6.2 Methods

When discussing the theory of light scattering, the most often used frameworks are the Rayleigh approximation and Mie theory.[160,161] The Rayleigh approximation is only valid for spherical particles that are much smaller than the wavelength of light in

consideration. Mie theory applies to spherical particles of any size. For extremely large particles, Mie theory converges with geometrical optics solutions. Mie theory is likewise valid for extremely small particles, but due to the ease of use of the Rayleigh approximation, is generally reserved for particles larger than one-tenth of the wavelength of the light that is being scattered. The derivation of the equations used by these two frameworks is well-known and can be found in several texts on light scattering.[162,163] Thus only the results of these derivations and a few other relevant equations are presented here.

The scattering cross section for the Rayleigh approximation is given by Eqn 6.1:

$$\sigma_{Ray} = \frac{8\pi a^6}{3}\left(\frac{2\pi n_{med}}{\lambda_0}\right)^4\left(\frac{m^2-1}{m^2+2}\right)^2 \tag{6.1}$$

where a is the particle radius, λ_0 is the wavelength of scattered light, n_{med} is the index of refraction of the medium, and m is the ratio of the index of refraction of the particle to that of the medium. The Mie scattering cross section is given by Eqn 6.2:

$$\sigma_{Mie} = \left(\frac{2\pi}{k_{med}^2}\right)\sum_{n=1}^{\infty}(2n+1)\left(|a_n| + |b_n|\right) \tag{6.2}$$

where $k_{med} = 2\pi n_{med} / \lambda_0$. The coefficients a_n and b_n are known as Mie coefficients and are calculated using spherical Bessel and Hankel functions.[163] The cross section can be converted to a scattering coefficient (ε) using Eqn 6.3:

$$\varepsilon = N\sigma \tag{6.3}$$

where N is the number concentration of the particles.

While the above equations account for the process of light scattering, the other process that must be considered is the absorption of incident radiation by the particles. The absorption cross section of absorbing particles can be calculated using Eqn 6.4:[164]

$$\sigma_{\text{abs}} = \frac{8\pi^2 m_3}{\lambda} \text{Re}(i\alpha) \tag{6.4}$$

where α is the polarizability of the particle, which is given by Eqn 6.5:

$$\alpha = \frac{m_1^2 - m_3^2}{m_1^2 + 2m_3^2} a^3 \tag{6.5}$$

where m_1 and m_3 are the complex refractive indices of the particle and the surrounding medium, respectively.

The extinction cross section and coefficient represent the loss of incident radiation due to both scattering and absorption as given in Eqns 6.6 and 6.7:

$$\sigma_{ext} = \sigma_{abs} + \sigma_{sca} \tag{6.6}$$

$$\varepsilon_{ext} = N\sigma_{ext} \tag{6.7}$$

The Beer-Lambert law can be used to relate the absorbance to the molar extinction coefficient, as given in Eqn. 3.2. The above equations were entered into a Matlab code to calculate numerical values for the scattering, absorption, and extinction coefficients and cross sections using both the Rayleigh approximation as well as Mie theory. The code can be found in Appendix D.

6.3 Theoretical calculations

6.3.1 Mie regime

Calculations of the scattering properties of a YAG:Ce^{3+} phosphor having a typical particle diameter between 1 and 2 μm are shown in Figures 6.1, 6.2, and 6.3. The wavelength of 450 nm was chosen since this is the typical wavelength of LEDs used to excite the phosphor. Mie scattering equations were employed because the size of the phosphor particles considered were on the order of twice the wavelength of light. The calculations suggest that both absorption and scattering contribute significantly to the extinction of light. The absorption cross section of the YAG:Ce^{3+} phosphor is on the order of 10^{-6} cm^2 and the extinction cross section is on the order of 10^{-7} cm^2. The ripple seen in the Mie scattering cross section curve in Figure 6.2 is characteristic of Mie scattering solutions and has been attributed to the resonance of the electric and magnetic fields internal to the particle.[165]

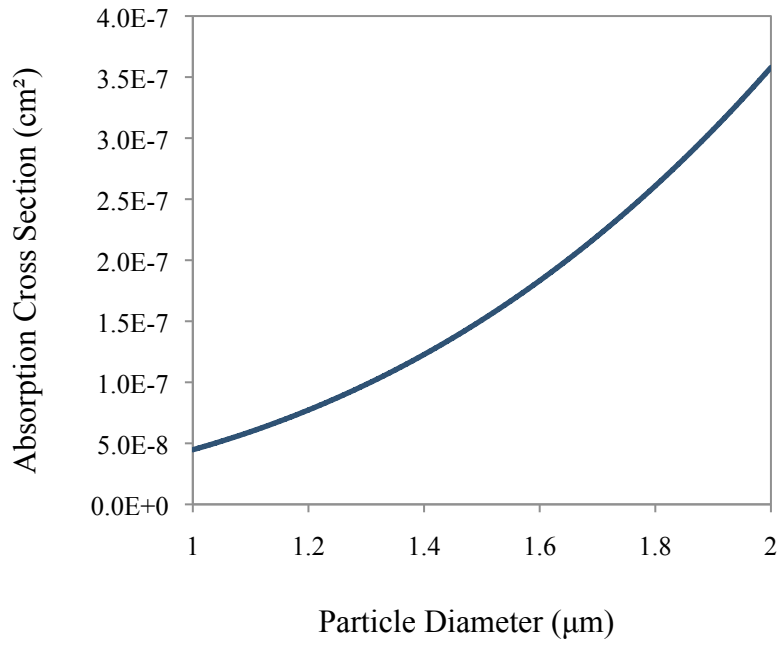

Figure 6.1: Absorption cross section for a micron-sized phosphor particle at a wavelength of 450 nm.

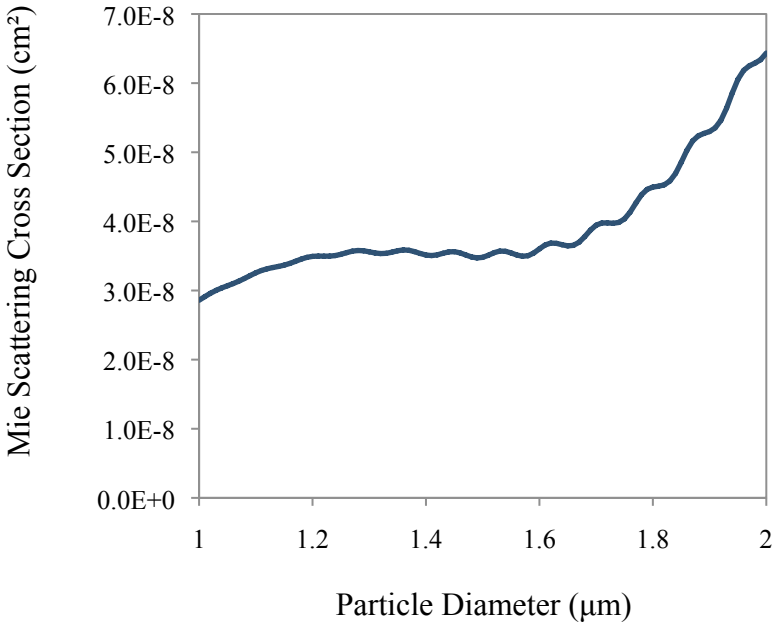

Figure 6.2: Mie scattering cross section for a micron-sized phosphor particle at a wavelength of 450 nm.

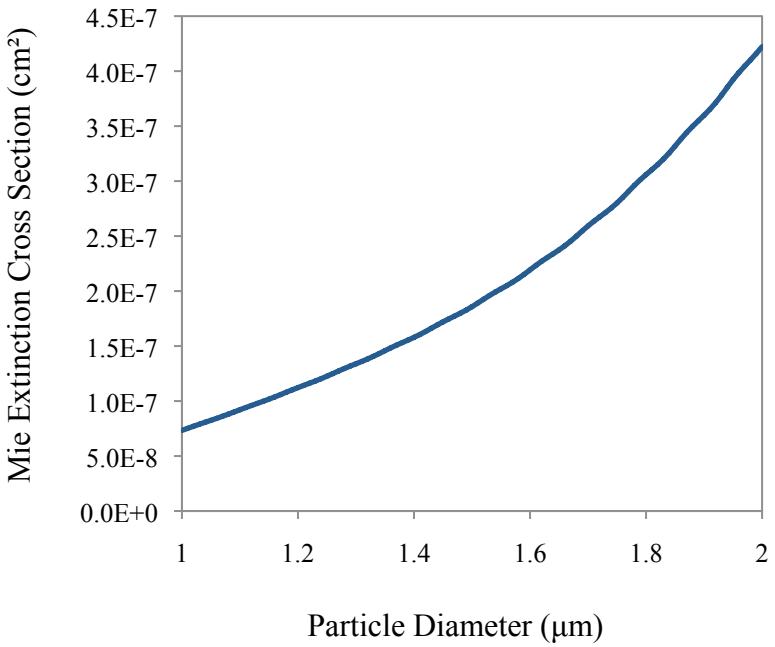

Figure 6.3: Mie extinction cross section for a micron-sized phosphor particle at a wavelength of 450 nm.

6.3.2 Rayleigh regime

Scattering properties of ultrasmall CdSe nanocrystals were calculated at wavelengths of 405 and 450 nm, as shown in Figures 6.4, 6.5, and 6.6. The single-size, white-light emitting nanocrystals are approximately 1.5 nm in diameter and are typically excited with near-UV or violet LEDs up to about 425 nm. The Rayleigh approximation was used for the nanocrystal calculations since the diameter of the nanocrystals is on the order of one hundredth of the wavelength. The extinction cross section is dominated by the absorption cross section contribution; hence, scattering of light from the nanocrystals can be neglected. The scattering cross section (10^{-20} cm^2) is five orders of magnitude lower than the absorption cross section (10^{-15} cm^2). The absorption cross section of the

nanocrystals is substantially smaller than that of the YAG:Ce^{3+} particles due to the vast size disparity between the two phosphors.

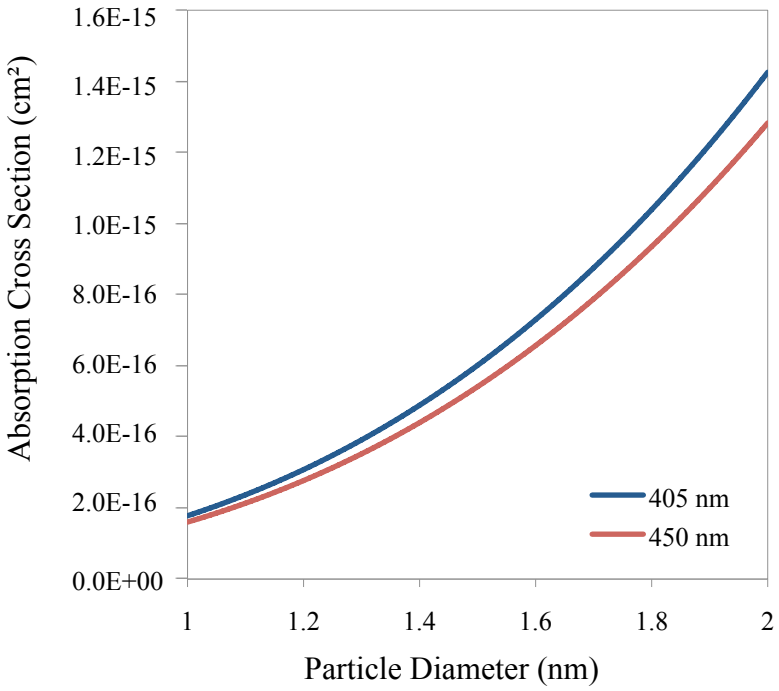

Figure 6.4: Absorption cross sections for ultrasmall CdSe nanocrystals at wavelengths of 405 nm (blue) and 450 nm (red).

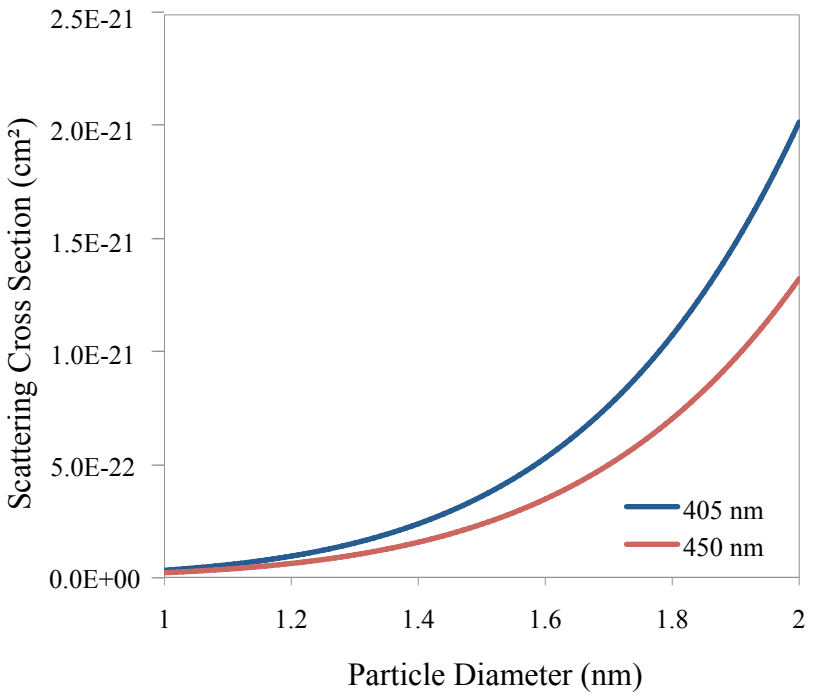

Figure 6.5: Rayleigh scattering cross sections for ultrasmall CdSe nanocrystals at wavelengths of 405 nm (blue) and 450 nm (red).

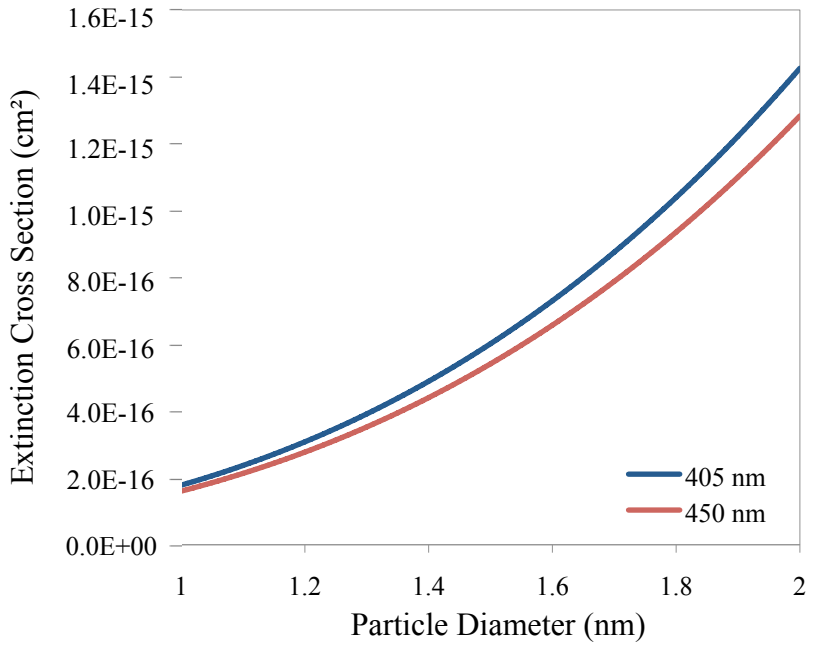

Figure 6.6: Rayleigh extinction cross sections for ultrasmall CdSe nanocrystals at wavelengths of 405 nm (blue) and 450 nm (red).

The absorption properties of CdSe nanocrystals can then be compared to the absorption properties for bulk CdSe. The extinction coefficient for bulk CdSe has been reported to be in the range of $10^5 - 10^3$ cm^{-1} for wavelengths between 400 nm and 750 nm, respectively.[166-168] In order to directly compare these values to the absorption cross section of CdSe nanocrystals, the following conversion from extinction coefficient to absorption cross section must be performed. The extinction coefficient in units of cm^{-1} is first converted to the molar extinction coefficient in terms of L/mol/cm by dividing by the molar concentration (mol/L). The molar concentration (30.36 mol/L for CdSe) is calculated by dividing the mass density (5.81 g/cm^3 for CdSe) by the molar mass (191.371 g/mol for CdSe) and multiplying by (1000 cm^3 / 1 L). The molar extinction coefficient (ε) is then converted to the absorption cross section (σ, in cm^2) using Eqn 6.8:

$$\sigma = \frac{2303\varepsilon}{N_A} \tag{6.8}$$

where N_A is Avogadro's number, or 6.02×10^{23} particles/mol. Using this conversion method, the absorption cross section for bulk CdSe is found to be in the range of $10^{-17} - 10^{-19}$ cm^2 for wavelengths between 400 and 750 nm, respectively. Thus, the absorption cross section for CdSe nanocrystals is one to three orders of magnitude higher than for bulk CdSe, depending on the wavelength. Consequently, in addition to their unique emission properties, CdSe nanocrystals have the further advantage of absorbing a larger fraction of incident light compared to an equivalent size unit of bulk CdSe.

In comparing the results of the calculations for micron-sized phosphor particles and nanometer-sized white-light nanocrystals, it is clear that scattering should only play a role for traditional phosphor-based white LED efficiency losses. Calculations showed

that for micron-sized phosphors, the extinction is affected by both scattering and absorption and thus will lead to scattering losses when incorporated into an LED device. The CdSe nanocrystals, however, had a scattering cross section five orders of magnitude lower than the absorption cross section. Therefore, scattering losses can be ignored for a photoluminescent device based on these white-light emitting nanocrystals, as the extinction cross section of the nanocrystals was found to be on the order of 10^{-16} cm^2 for near-UV excitation. Other sources of loss, including internal quantum efficiency and absorption efficiency, are expected to be the dominant factors in device efficiency of CdSe nanocrystal-based white LEDs. The use of CdSe nanocrystals as a white-light phosphor could lead to higher quality and more efficient solid-state lighting devices.

6.4 Experimental verification of calculations

For experimental verification of the above calculations, the Beer-Lambert law given in Eqn. 3.2 was applied. The thickness of the films was measured according to the method in Section 3.3, and absorbance measurements of the films were performed using the procedure in Section 3.2. The concentration of the nanocrystals in the dropcasting solution was determined using a method as described in Yu *et al*.[169] By using a known volume of the dropcasting solution of nanocrystals in the polymer, the total number of nanocrystals in that solution can be calculated. When the film has cured, the total number of nanocrystals is divided by the volume of the film to determine the particle concentration of the film.

Since the calculations of absorption and scattering cross sections of the ultrasmall nanocrystals assume that the nanocrystals are well-dispersed, experiments were

conducted to verify that there was no aggregation of the nanocrystals when encapsulated into a phosphor film.[170] The experiments reported here represent the first measurements of the extinction cross sections and coefficients of white-light nanocrystal phosphors. While prior white-light fluorescence and bright field differential interference contrast micrographs of CdSe nanocrystals encapsulated in BP-PFCB suggested that the nanocrystals were well-dispersed,[124] comparison of theoretical and experimental values of extinction cross section and coefficient verify that there is negligible agglomeration of the nanocrystals when encapsulated in the phosphor film. Table 6.1 shows the comparison and good agreement between the theoretical and experimental values. It is noted that the molar extinction coefficient is reported in the table since this is the value found directly from the measurements. The extinction coefficient given in Eqn 6.7, which has units of 1/cm, can be converted to the molar extinction coefficient with units of L/mol/cm, by dividing by the concentration in mol/L.

Table 6.1. Experimental and theoretical comparison of the scattering properties of thin films of CdSe nanocrystals.

Band-Edge Absorption Wavelength (nm)	405 ± 2
Particle Diameter (nm)	1.60 ± 0.02
Concentration (mol/L)	$(9.93 \pm 0.03) \times 10^{-5}$
Rayleigh Extinction Cross Section (cm^2)	7.44×10^{-16}
Measured Extinction Cross Section (cm^2)	$(1.85 \pm 0.04) \times 10^{-16}$
Rayleigh Extinction Coefficient (L/mol/cm)	1.15×10^5
Measured Extinction Coefficient (L/mol/cm)	$(1.11 \pm 0.02) \times 10^5$

6.5 Extinction coefficient of CdSe nanocrystals

To calculate the extinction coefficient, as was done in Section 6.4, the Beer-Lambert law (Eqn. 3.2) is most often used. While the absorbance and thickness are

straightforward to measure, the measurement of the concentration is more difficult. In Section 6.4, the concentration was determined using the method described in Yu *et al.*[169] In this section, the concentration will be measured directly and used to calculate the extinction coefficient of CdSe nanocrystals and then compare these results to previous reports.

There have been several previous investigations into the extinction coefficient of CdSe nanocrystals,[164,169,171-173] and comparison of them shows inconsistent results. The most likely reason for the discrepancies is due to the measurement of the nanocrystal concentration. Schmelz *et al.*[171] first reported the extinction coefficient to have a cubic dependence on the nanocrystal diameter. Atomic absorption spectroscopy (AAS) was used to measure the Cd concentration in a sample of known mass. While a good method to measure the Cd concentration, an excess of Cd precursor that is left over from the pyrolitic synthesis method[169,174] can cause an inaccuracy in the particle concentration calculation.

Striolo *et al.*[172] investigated the extinction coefficient of CdSe nanocrystals, and like Schmelz *et al.* found a cubic dependence on the particle diameter. Particle concentration was calculated by dissolving a known mass of dried nanocrystals into a known volume of solvent. Through the use of membrane osmometry, the molecular weight of the nanocrystals was calculated after assuming that there was no excess Cd, Se, or ligands in the solution. Previous research[169,174] has shown that there is a significant amount of excess Cd precursor after synthesis and before cleaning, which can be up to 90% of the initial amount, causing a large error in the assumption that there is no excess material if it is not removed completely.

Later reports by Leatherdale *et al.*[164] and Yu *et al.*[169], like Schmelz *et al.,* assumed a spherical particle shape and 1:1 Cd to Se ratio when determining how many Cd atoms were in each nanocrystal. Previous research has shown that the ratio of Cd to Se for TOPO-capped nanocrystals is 1.2:1,[174] and that their particle shape is non-spherical,[175] which will cause further discrepancies in the concentration calculation. Recently, Jasieniak *et al.*[173] investigated the extinction coefficient of CdSe nanocrystals using ICP-OES to determine the Cd concentration and two different synthesis methods to achieve a range of nanocrystal sizes. Though their data agreed well with Yu *et al.* at larger nanocrystal sizes, there was a large difference between these reports at smaller nanocrystal sizes.

To address these issues, an alternative approach was used to measure the concentration of the nanocrystals and obtain a more accurate measurement of the extinction coefficient. Inductively-coupled plasma mass spectrometry (ICP-MS) was used to measure the concentration of both Cd and Se atoms, in addition to using a more precise model of a CdSe nanocrystal taking into account its true non-spherical shape and Cd to Se ratio. Also, a more comprehensive sizing curve based on a compilation of multiple reports of nanocrystal diameter and their corresponding band-edge absorption wavelength was utilized.

The nanocrystal synthesis method, detailed in Section 2.4, is based on a CdO precursor and results in nanocrystals coated with phosphonic acid ligands. By varying the duration of the reaction, nanocrystal sizes were synthesized from approximately 1.5 nm to 3 nm in diameter, and showed a low size distribution as evidenced by a narrow band-edge absorption peak. The smallest nanocrystals did not require etching or a

separate synthesis method as in previous reports, as they can be directly synthesized with a diameter of ~1.5 nm.[123,125,124] The nanocrystals were purified by precipitating and centrifuging the nanocrystals in methanol, followed by redissolving and centrifuging the nanocrystals in hexanol. Repeating this process twice removed the majority of excess matter such as free ligands and precursors from the solution, as determined by Rutherford backscattering spectroscopy (RBS).

After synthesis, the absorption spectrum of the nanocrystals was measured in a solution of toluene in ambient air, with a selection of the results shown in Figure 6.7. To determine the diameter a sizing curve was used, relating the band-edge absorption wavelength of the nanocrystals to their diameter. The sizing curve used in this work, which can be seen in Figure 6.8, was formed by compiling the results of multiple reports of the diameter and the band-edge absorption wavelength.[77,169,176,177] In these previous reports, the nanocrystal diameter was established by transmission electron microscopy (TEM) measurements on larger nanocrystals and x-ray diffraction (XRD) measurements on smaller nanocrystals. An empirical fit to the data is given by Eqn 6.9:

$$d(nm) = (50.23) + (0.51)\lambda - \left(1.89\text{x}10^{-3}\right)\lambda^2 - \left(3.05\text{x}10^{-6}\right)\lambda^3 + \left(1.82\text{x}10^{-9}\right)\lambda^4 \tag{6.9}$$

where d is the nanocrystal diameter (nm).

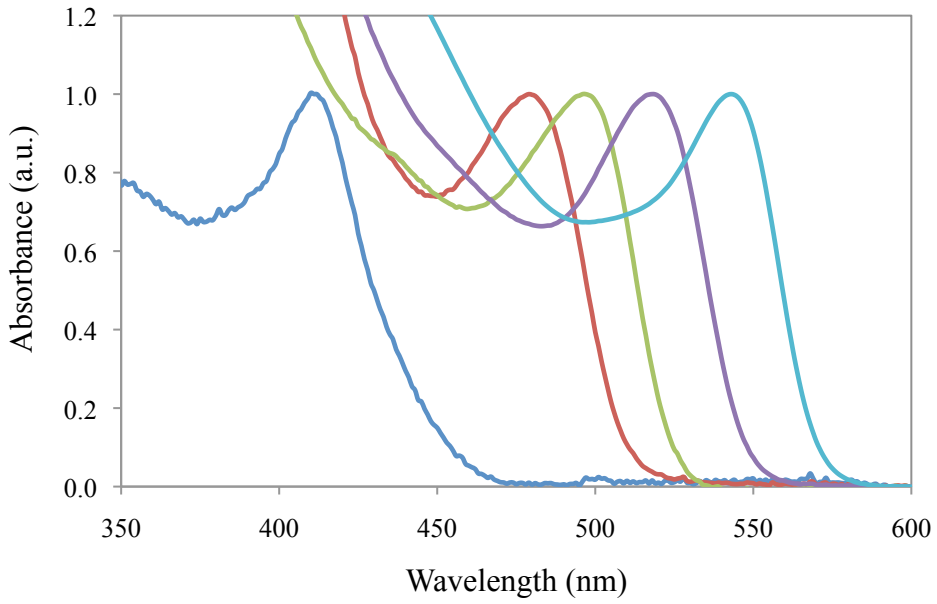

Figure 6.7: Absorption spectra of different nanocrystal sizes in solution, with just a selection shown for ease of display.

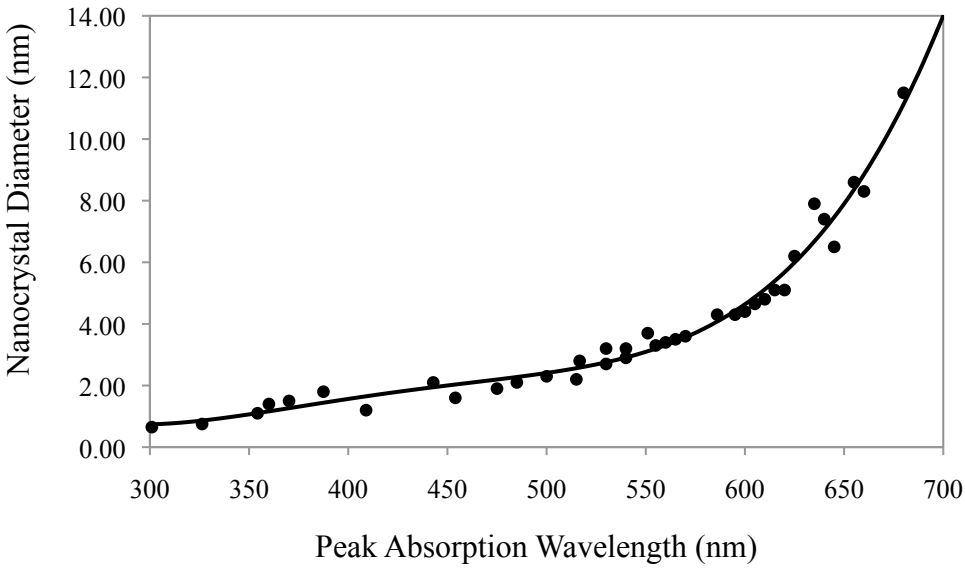

Figure 6.8: Sizing curve for CdSe nanocrystals. The solid line represents a curve fit to the data using Eqn 6.9.

The diameter was then used to determine the total volume per nanocrystal as well as the number of Cd and Se atoms per nanocrystal. Previous research[174,175] used TEM to analyze the shape of a CdSe nanocrystal, which was found to be non-spherical for all nanocrystal sizes studied, and determined the volume based on several size and shape parameters. Because of the non-spherical shape, the nanocrystal diameter used in this work is the average of the short and long axes. Using this non-spherical structure resulted in a smaller volume and a lower total number of atoms per nanocrystal, and thus a lower extinction coefficient by as much as 10%, as compared to assuming a spherical particle shape.

In addition, RBS was previously used to determine the Cd to Se ratio, which was found to be approximately 1.2:1.[174] If the Cd concentration is used for the extinction coefficient calculation as in previous reports, a Cd to Se ratio of 1.2:1 will result in a 9% higher extinction coefficient value compared to using the 1:1 ratio that is usually assumed. In this work, as will be discussed below, the Se concentration was instead used for the calculation of the extinction coefficient, and thus a Cd to Se ratio of 1.2:1 will result in a 9% lower extinction coefficient compared to a ratio of 1:1.

With the absorbance determined from Figure 6.7, the total Cd and Se concentrations were then measured using ICP-MS, which are given in μg/L. The method of standard additions was used along with a multiple point calibration, yielding the most precise concentration determination. The ICP-MS samples were prepared by allowing a solution of nanocrystals with known absorbance to dry in a vial in a fume hood at room temperature over several days. Next, 570 μL of aqua regia (3:1 by volume concentrated $HCl:HNO_3$) was added to the vials and then closed, allowing 1 hour to digest the dried

nanocrystals. This solution was added to 9.43 mL of deionized water for a total of 10 mL at 1% HNO_3 for ICP-MS measurements. The Se concentration found from the ICP-MS measurements was used to calculate the particle concentration needed for the extinction coefficient calculation. As was mentioned earlier, a large amount of Cd precursor is left over after synthesis and can be as much as 90% of the initial amount, causing the appearance of a higher particle concentration and thus a lower extinction coefficient. Even after thorough cleaning, it is possible that some Cd precursor would remain. For this reason, the Se concentration leads to a more accurate representation of the particle concentration, and likewise a more accurate extinction coefficient. Using the atomic masses for Cd and Se and Avogadro's number, the concentration was converted to units of mol/L.

Next, the extinction coefficient is calculated using Eqn. 3.2. The results of these calculations for a range of nanocrystal diameters from 1.5 to 3 nm, which corresponds to a band-edge absorption peak of roughly 400 to 550 nm, as well as a comparison to previous reports is summarized in Table 6.2 and displayed in Figure 6.9. The data labeled as Cd is calculated by using the Cd concentration from the ICP-MS measurements instead of Se, even though there is likely at least a slight excess of Cd remaining from the precursor. The Cd calculation was done to show that when the Cd concentration is used, as was done in previous reports, the data from this work agrees closely with data from Yu *et al*. The calculated data using both the Cd and Se concentrations, with the latter believed to be more accurate, are graphed individually as a function of nanocrystal diameter in Figure 6.10. Using the Se concentration data, an

empirical fit as given in Eqn 6.10 of the extinction coefficient vs. nanocrystal diameter can be obtained, where d is given in nm:

$$\varepsilon(\text{L/mol/cm}) = 22256.1 + \left(882.546 \times d^{4.54}\right) \quad (6.10)$$

The extinction coefficient can then be converted to the absorption cross section per particle (σ, in cm^2) using Eqn 6.8. The empirical fit is as follows:

$$\sigma(\text{cm}^2) = 8.514\text{x}10^{-17} + \left(3.376\text{x}10^{-18} \times d^{4.54}\right) \quad (6.11)$$

The goodness of fit can be measured with the reduced chi-square value,[178] where a value of close to 1.0 signifies a good fit to the data. The reduced chi-square values for the Cd and Se concentration data were 1.77 and 1.18, respectively. This indicates that there is more scatter in the Cd data, and thus the use of the Se data results in higher precision.

Table 6.2. Summary of data for extinction coefficient calculations at various nanocrystal sizes.

Band-Edge Absorption Peak	Diameter	Total atoms per NC	Absorbance	Cd Extinction Coefficient	Se Extinction Coefficient
(nm)	(nm)			(L/mol/cm)	(L/mol/cm)
407	1.63	45	0.007	5.47E+03	2.83E+04
412	1.68	49	0.012	1.92E+04	4.73E+04
442	1.94	76	0.010	6.63E+03	2.32E+04
480	2.24	117	0.015	5.16E+04	6.07E+04
490	2.32	130	0.011	6.15E+04	5.60E+04
497	2.38	141	0.021	8.50E+04	8.83E+04
500	2.41	146	0.014	2.61E+04	3.67E+04
506	2.47	157	0.031	3.73E+04	7.97E+04
519	2.61	185	0.046	7.52E+04	1.13E+05
536	2.84	240	0.055	1.05E+05	1.09E+05
540	2.91	257	0.077	1.52E+05	1.53E+05
544	2.98	276	0.132	9.55E+04	1.38E+05

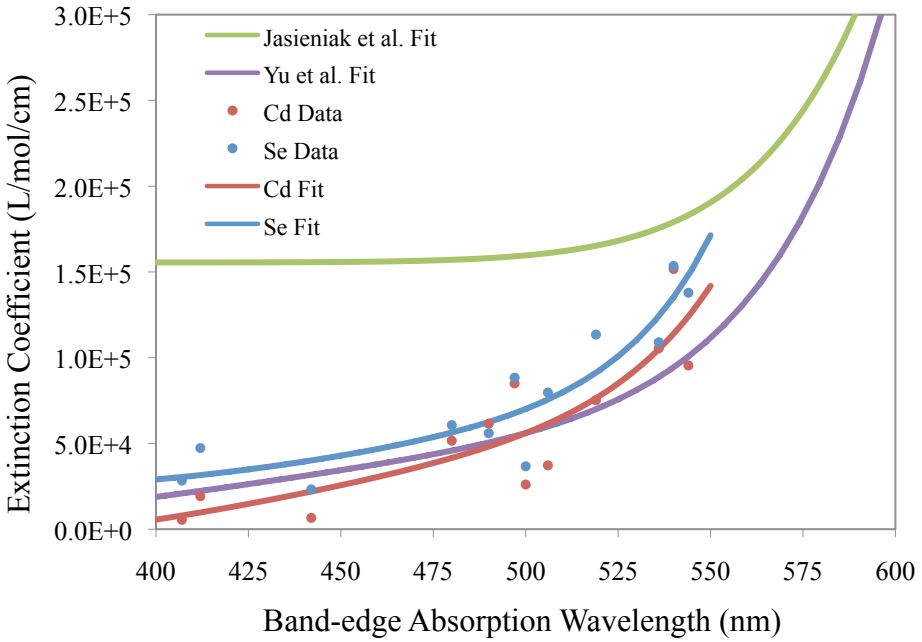

Figure 6.9: Molar extinction coefficient at the band-edge absorption wavelength, using Cd (red) and Se (blue) concentrations. The red line represents an empirical fit to the Cd concentration data (reduced chi-square = 1.77) and the blue line is a fit to the Se concentration data (reduced chi-square = 1.18). The purple line represents the empirical fit function from Yu *et al.*[169] and the green line is the fit function from Jasieniak *et al.*[173] which was converted from a function of the band-edge absorption energy to the band-edge absorption wavelength.

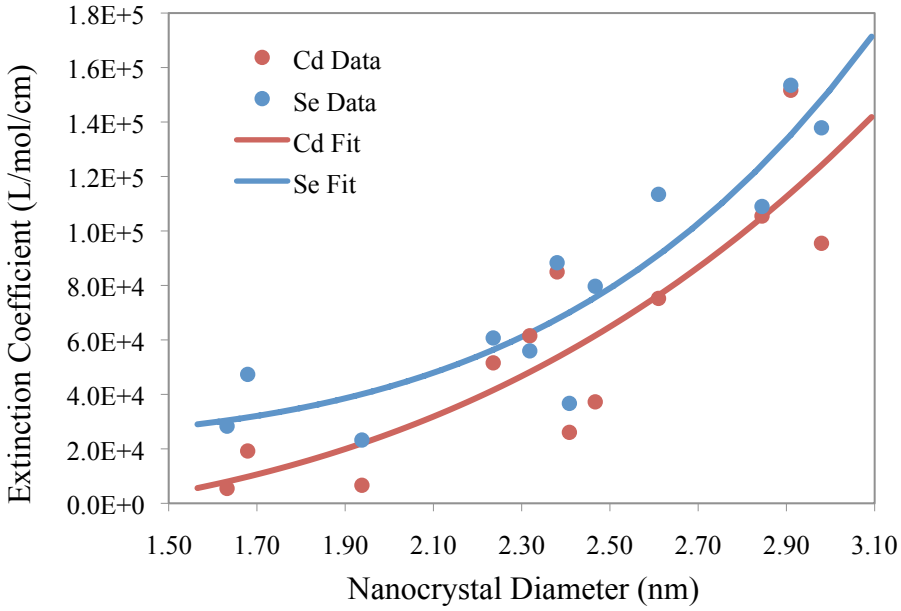

Figure 6.10: Molar extinction coefficient at the band-edge absorption wavelength, using Cd (red) and Se (blue) concentrations. The red line represents an empirical fit to the Cd concentration data (reduced chi-square = 1.77) and the blue line is a fit to the Se concentration data (reduced chi-square = 1.18).

The data from this work differ from some previous reports, which can be accounted for by considering several factors. First, the use of ICP-MS and the standard additions method to measure the Se concentration ensures that any excess Cd precursor left in the solution after synthesis and cleaning will not factor into the concentration calculation. Second, a more accurate model of the non-spherical shape and nonstoichiometric Cd to Se ratio yields a more precise value of the concentration and thus extinction coefficient. Third, a more comprehensive sizing curve based on a compilation of multiple reports was used to convert from the band-edge absorption wavelength to the effective nanocrystal diameter. Finally, initial results of samples with varying digestion times in aqua regia has shown that the concentration of Cd and Se decreases over time,

possibly due to the formation of volatile species such as $CdCl_2$ and SeO_2. Using a three-day digestion time in aqua regia, as used in Jasieniak *et al.*,[173] the concentration of both Cd and Se decreased significantly compared to a five-minute digestion time. Thus, it might be helpful to digest the nanocrystals in a different solution (e.g. nitric acid) that has lower volatility with Cd and Se, and to use a short digestion time to minimize the formation of volatile species.

6.6 Conclusions

In this chapter, the scattering properties of common micron-sized phosphor particles and ultrasmall CdSe nanocrystals for white LEDs were analyzed. Calculations show that for micron-sized phosphors, the extinction is affected by both scattering and absorption and thus will lead to scattering losses when incorporated into an LED device. The CdSe nanocrystals, however, had a scattering cross section five orders of magnitude lower than the absorption cross section. Therefore, scattering losses can be neglected for a photoluminescent device based on these white-light emitting nanocrystals. The extinction cross section of the nanocrystals was found to be on the order of 10^{-16} cm^2 for near-UV excitation. Nanocrystal films were used to verify the calculations, with good agreement found between the theoretical and experimental values. This was done using a method from previous reports of the extinction coefficient of CdSe nanocrystals in solution. After using this method, it was found that some of the assumptions used in these previous reports were not accurate, and thus a more accurate approach to determining the extinction coefficient of CdSe nanocrystals was investigated.

The same trend was observed with the extinction coefficient increasing as the nanocrystal diameter becomes larger, as seen in earlier reports. The data in this work differed quantitatively, however, due to more accurate considerations of the nanocrystal shape and Cd to Se ratio, as well as a more accurate determination of the nanocrystal concentration via ICP-MS measurements using the method of standard additions. A more accurate curve of the extinction coefficient vs. nanocrystal diameter can be used to make a convenient determination of the concentration of nanocrystals in solution via Eqn 3.2 by performing a routine absorption measurement. Likewise, this same method and calibration curve can be used for encapsulated nanocrystals in a thin film with the addition of a film thickness measurement.

CHAPTER VII

CONCLUSION

7.1 Summary

In this work, experiments and simulations were completed in pursuit of a CdSe nanocrystal-based, white light-emitting diode. Following the discovery of monodisperse, ultrasmall, white-light emitting CdSe nanocrystals, the first challenge was to find a material that could be used to encapsulate these nanocrystals. Encapsulated nanocrystals are less prone to oxidation and are better protected from the heat emitted by an LED junction. In addition, a suitable encapsulant would inhibit the nanocrystals from aggregating and allow for good adhesion to an LED surface. Thirteen different encapsulants were studied to see which material would mix well with the nanocrystals in solution, cure as designed, and maintain the desirable properties of the ultrasmall CdSe nanocrystals. It was found that the BP-PFCB polymer had over twice the emission intensity of the next best encapsulant, and also did not modify the spectral shape of the nanocrystal emission or decrease the nanocrystal quantum yield. Furthermore, the BP-PFCB encapsulant allowed for a much higher loading percentage than the other materials, which leads to high UV light absorption at a fraction of the thickness that the other encapsulants required. Nanocrystal-BP-PFCB films that were heated to 190 ºC for 48 hours showed very little change in optical properties, which indicates that the polymer provides protection against heating. It is believed that one reason for the higher emission intensity when using BP-PFCB was due to much lower nanocrystal aggregation than was

found in silicone or epoxy-encapsulated films. Finally, the nanocrystal concentration dependence on the emission properties was examined. An increase in the nanocrystal concentration resulted in a small decrease in the blue emission, which was attributed to self-absorption by the nanocrystals. The color qualities of these nanocrystal-polymer films were impressive when compared to commercial devices, with CIE coordinates of (0.324, 0.322) and a CRI of 93.

Although these films had excellent color qualities, the efficiency was found to be just several lm/W. The main causes of this low device efficiency were the quantum yield of the nanocrystals and the efficiency of the UV excitation LED, both typically between 5 and 10% in these experiments. Improving these causes of efficiency loss was beyond the scope of this work. However, several other approaches were investigated as possible areas for efficiency improvements. First, the nanocrystal-polymer film thickness dependence on the absorbance and emission properties was examined using a nanocrystal concentration of 10% weight concentration in BP-PFCB. The optical density was found to increase as the film thickness increased, which was expected in accordance with the Beer-Lambert law. Also, the absorbance was nearly constant for wavelengths below 400 nm, indicating that deeper UV LEDs would likely not result in a larger efficiency. Furthermore, the data showed that a film thickness above ~150 μm resulted in an absorbance of ~100%, implying that a thickness of 150 μm results in optimal absorption properties. Next, the dependence of film thickness on the emission properties was analyzed using both a UV laser and various peak wavelengths of UV LEDs for excitation. UV laser excitation showed that an increasing thickness generally resulted in a higher emission intensity but also greater self-absorption of nanocrystal emission. The

thickest films (on the order of 1 mm) exhibited a decreased emission intensity and emitted a somewhat yellowish light. Next, the films were excited using different peak wavelength UV LEDs to determine the optimum excitation wavelength and film thickness combination. Similar to the laser excitation data, the emission intensity increased linearly with thickness but dropped off at larger film thicknesses. In addition, as the peak wavelength of the UV LED is increased for the same film thickness, the emission becomes more blue due to excitation light that leaks through the films at longer wavelengths. It was found that the optimum device parameters were using a 365 nm or 385 nm LED to excite a film in the 60-140 μm range. Finally, dielectric mirrors were simulated as a possible approach to increasing the absorption and extraction efficiency of a nanocrystal-based LED. Two mirror designs were simulated. One was designed to have a high UV reflectance and high visible transmittance to redirect UV light that leaks through the nanocrystal film but let visible, emitted light pass. The other mirror was designed to have high visible reflectance and high UV transmittance to redirect emitted light away from the LED die and out of the device while letting UV excitation light pass through. For the first design, ten periods of HfO_2/SiO_2 layers centered at 365 nm was found to be suitable for high UV reflectance and high visible transmittance. However, layers centered at a single wavelength were not sufficient for the second mirror design due to a limited reflectance bandwidth that is a result of a small refractive index difference between the two layer materials. For this mirror design, a chirped structure, where the center wavelength is varied throughout the layers, was found to be the most attractive option because it would require fewer deposited layers than a structure where

multiple mirrors are simply stacked one on top of another to achieve a wide reflectance bandwidth.

The final area of investigation in this work is the scattering properties of the nanocrystals, which is related to the previous experiments on optical properties and device efficiency. A major source of loss in commercial LEDs is due to the significant scattering by micron-sized phosphor particles, where the excitation light is reflected back towards the LED die and gets re-absorbed. A nanometer-sized particle, on the other hand, scatters much less than micron-sized particles, which could lead to more efficient LEDs. Calculations using Mie theory showed that both scattering and absorption contributions to the extinction coefficient were significant, and lead to efficiency losses in LED devices. The absorption cross section for common YAG:Ce^{3+} phosphor particles is on the order of 10^{-6} cm^2 and the extinction cross section is on the order of 10^{-7} cm^2. Using the Rayleigh approximation, which is valid for particles much smaller than the wavelength of light under investigation, showed that the extinction properties are dominated by absorption in the ultrasmall CdSe nanocrystals. Hence, there is virtually no scattering of light by nanocrystals in the near UV and visible light ranges, and thus scattering can be neglected. The scattering cross section (10^{-20} cm^2) was found to be five orders of magnitude lower than the absorption cross section (10^{-15} cm^2). Nanocrystal-polymer films were used to verify the calculations, with good agreement between the theoretical and experimental values. This was done via the Beer-Lambert law, along with results from previous reports of the extinction coefficient of CdSe nanocrystals in solution. Upon further investigation, it was found that some of the assumptions used in these previous reports were not accurate. To address these issues as well as measure the

extinction coefficient of white-light emitting CdSe nanocrystals to see how they compare to previous reports as well as to larger CdSe nanocrystals, a more accurate approach to determining the nanocrystal concentration and thus the extinction coefficient was investigated. ICP-MS measurements using a standard additions method and multiple point calibration was used to determine the atomic concentration of both Cd and Se in a solution of nanocrystals with a known absorbance. Likewise, an aggregation of multiple reports led to a more comprehensive sizing curve, which compares the nanocrystal diameter to the band-edge absorption wavelength. Moreover, this approach took into account a previous study that determined the shape of CdSe nanocrystals to be non-spherical and the cadmium to selenium ratio to be nonstoichiometric. Finally, an excess of cadmium left over from the nanocrystal synthesis implies that the Se concentration should be used instead of the Cd concentration to determine the extinction coefficient. The same trend as previous reports of an increasing extinction coefficient as the diameter becomes larger was found, though it differed somewhat quantitatively. A more accurate extinction coefficient can be used to make a better determination of the concentration of nanocrystals in solution with a routine absorption measurement, or for a nanocrystal film with an additional thickness measurement.

7.2 Future Research

Alhough this work represents a significant contribution to the development of a photoluminescent, white-light nanocrystal-based light-emitting diode, there are several opportunities for future research and experiments. To increase the extraction efficiency of these devices, the dielectric mirror designs could be fabricated and tested to determine

the efficiency improvement that they provide. Though the simulations were initially done with the intent to fabricate these mirrors, after the simulations were completed it was found that the number of layers required for high reflectance and transmittance in the desired regions and the sensitivity of the layer thickness on the optical properties of the mirror was beyond the capabilities that were available. In addition, there are other methods for increasing the extraction efficiency for LEDs that could be investigated. Some of these methods, as detailed in Section 1.6.4, include surface roughening, photonic crystals for out-coupling, chip-shaping, a remote phosphor design, and micro-patterning, among many others. Additionally, other researchers have found that the distance between the excitation LED die and the phosphor film can greatly impact the device efficiency. Thus, the capability to fabricate devices with the nanocrystals directly on top of the die or at varying distances from the die could reveal further efficiency improvements.

Another area for future research concerns the lifetime of these nanocrystal devices. A typical method for increasing the lifetime of nanocrystal luminescence is to fabricate a shell around the nanocrystal core, known as a core-shell nanocrystal. This shell provides protection against photo-oxidation and greatly improves the device lifetime. Non-shelled nanocrystals degrade via the photo-oxidation of surface selenium atoms, though keeping them in an inert atmosphere will greatly reduce the rate of this photo-oxidation. Initial testing indicated that the photostability of white-light nanocrystals, which cannot be shelled without the loss of white-light emission, is improved somewhat by the polymer encapsulation. Synthesizing the nanocrystals and

fabricating these devices entirely under inert conditions, and packaging them in a material that is impermeable to oxygen could realize further lifetime improvements.

The experiments detailed in this work have shown that white-light, CdSe nanocrystal-based LEDs have excellent color qualities that surpass the Department of Energy requirements for general lighting. The main focus herein was to discover and develop approaches to device efficiency increases, as it is currently on the order of a few lm/W. In addition to the methods examined earlier, the main focus in the future will need to be on improving the efficiency of the UV LEDs used for excitation, as well as the nanocrystal quantum yield, both typically between 5 and 10% in these experiments. Many research groups and companies are working to increase UV LED efficiencies, as they are not only important for lighting applications but also in other areas such as UV curing of materials, air and water purification, counterfeit money identification, medical instrumentation, and forensic analysis, among quite a few others. Similarly, the Rosenthal group at Vanderbilt has been working to increase the white-light nanocrystal quantum yield from 3% when initially discovered to over 10% just a few years later. Improvements in either of these efficiencies would directly improve the device efficiency of the white-light phosphor-conversion LEDs, and could lead to solid-state lighting devices that are more economical and of a higher quality. With the current thrust for energy conservation and continued research into nanocrystal properties, the prospect for these materials is encouraging. Several companies have started up in recent years to develop nanocrystals for use in lighting applications such as LEDs as well as LCD televisions, with other uses likely to come as efficiencies and color properties are further improved.

APPENDIX A

AR-KR LASER OPERATION

TO TURN THE LASER ON:

1. Make sure that you have read the Coherent Operator's Manual, especially the sections on laser safety. Use safety glasses for UV or the laser safety goggles for Visible.
2. Turn the three yellow handles on the wall where the water pipes are run from BYPASS to flowing through the chiller.
3. Make sure that the fuse box above the chiller has its power switch set to ON.
4. Turn the rocker switch on the right side of the Affinity module (black box on left side of Figure A.2) to ON.
5. Turn the rocker switch on the chiller unit (large black box on floor) to ON.
6. Wait at least 10 minutes for the water running through the chiller unit to cool down enough for laser operation (will fluctuate between roughly 0° and 10-15° as displayed on the Affinity module when it has cooled sufficiently). You should see the dial on the meter on the wall in one of the water lines moving to indicate water is cycling through the chiller system, and you should also be able to feel water movement through the hoses. If there is no water moving through the system, you must not turn on the laser. If the laser is turned on without cooling water, the laser will be at risk of damage.
7. Move the switch up on the fuse box on the wall near the laser to give the laser access to power.
8. Turn the keyswitch on the power supply (black box below the table) to provide power to the laser and its control module.
9. Press the ON/OFF button on the Coherent module to start the laser, which should turn on after a delay of 50 seconds as shown on the Coherent module display.
10. To change the laser wavelength, turn the knob on the upper left corner of the rear panel of the laser box (where the large hose is).
11. To optimize the laser power, turn the knob on the lower right corner of the rear panel slowly back and forth until you find the maximum intensity. The laser output power can also be controlled by the aperture control knob near on the top of the laser box near the front as well as on the control module by adjusting the current provided to the laser. From my experience, some of the laser lines will not show up unless you have the current sufficiently high, as much as 30-35 Amps.

TO CHANGE THE LASER FROM VISIBLE TO UV OR FROM UV TO VISIBLE:

1. For UV operation, the UV optics must be inserted, which includes the output coupler on the front of the laser box as well as the high reflector on the rear of the laser box. The high reflector should be in the multiline position, which is the position closer to the laser where the light is reflected before it can reach the prism.
2. For visible operation, the visible optics must be inserted, which includes the output coupler on the front of the laser box as well as the high reflector on the rear of the laser box. The high reflector can be in the single-line or multiline position, with the single-line position being the one further from the laser where it is behind and below the prism used to select the wavelength, and the multiline position is the position closer to the laser where the 1laser light is reflected before it can reach the prism. The visible high reflector can be left in the single-line position while the UV high reflector is in the multiline position.

3. To change the high reflector, remove the two nuts at the rear of the laser box and then remove the cover. Next, while wearing gloves, slightly loosen the very small screw that holds the spring clip tight to the high reflector, rotate the spring clip off of the back of the high reflector, and carefully remove the high reflector by grabbing the frosted edge (avoid touching the smooth faces) using a hemostat (tweezers). Insert the other high reflector in the desired position, with the arrow on the edge pointed towards the laser cavity, rotate the spring clip back, and tighten the screw without overtightening. It just needs to be secure, too tight will scratch the high reflector. Put the cover back on and replace and tighten the two nuts.
4. To change the output coupler, remove the two nuts at the front of the laser box and then remove the cover. Next, while wearing gloves, slide the output coupler/beamsplitter assembly off of its rails, grab the frosty sides of the output coupler using a hemostat (tweezers), and pull the output coupler out (may need to gently rock back and forth to loosen it). Insert the other output coupler in the same position, with the arrow on the edge pointed toward the laser cavity, slide the assembly back on its rails, and then put the cover back on and replace and tighten the two nuts.
5. When switching to Visible emission, you will need to do the vertical search procedure as detailed in the Coherent Operator's Manual. Briefly, you set the laser to full current, turn the knob on the upper left of the rear panel of the laser counter-clockwise until there is less resistance and it moves pretty freely, and while slowly turning the knob on the lower right of the rear panel, rock the lever on the top of the laser box near the rear back and forth until you see lasing. If you can't move the lower right knob anymore, go back the other direction, repeating this process until you have achieved lasing. The colors should change rapidly as you are moving the lever back and forth when it is correctly aligned, as it is akin to moving the upper left knob to change the laser wavelength. From my experience, when switching from the laser aligned correctly in UV mode to Visible mode, the lower right knob will need to be turned a little bit clockwise to align it correctly for Visible mode. If you cannot achieve lasing, make sure everything is on, the current is set to max, the shutter is open, the aperture is open, and the high reflector and output coupler were installed properly and in the correct direction. If all of that fails, refer to the alignment procedures in the Operator's Manual.
6. When switching to UV emission, you will need to do roughly the same procedure as in #5 (switching to Visible) except the cover of the laser will need to be removed (8 small black screws, two in each corner). Be careful, as you are now more exposed to the high voltage of the laser with the cover off. Set the laser to full current, and slide the dust shield off of the Brewster window near the rear of the laser, and then place a small white piece of paper (a business card works great) directly below this window. Do the same procedure as in #5, except when you achieve lasing you will see flashes of a dot of blueish/purple on the white paper. Remove the paper or card, slide the dust shield back into place, and put the cover for the laser back on. From my experience, when switching from the laser aligned correctly in Visible mode to UV mode, the lower right knob will need to be turned a little bit counter-clockwise to align it correctly for UV mode. If you cannot achieve lasing, make sure everything is on, the current is set to max, the shutter is open, the aperture is open, and the high

reflector and output coupler were installed properly and in the correct direction. If all of that fails, refer to the alignment procedures in the Operator's Manual.

TO TURN THE LASER OFF:

1. Push the ON/OFF button on the Coherent module to stop the laser.
2. Next, turn the keyswitch in the black box below the table back to OFF.
3. Move the switch down on the fuse box on the wall near the laser.
4. Allow the chiller to run for at least 10 minutes to cool off the laser components. You can feel the hoses running into and out of the chiller box on the floor, and when all of them feel cool, then it is safe to turn the chiller off. Do this by first turning the rocker switch on the chiller unit to OFF, then turn the rocker switch on the Affinity module to off, and then turn the yellow handles on the wall back to BYPASS.

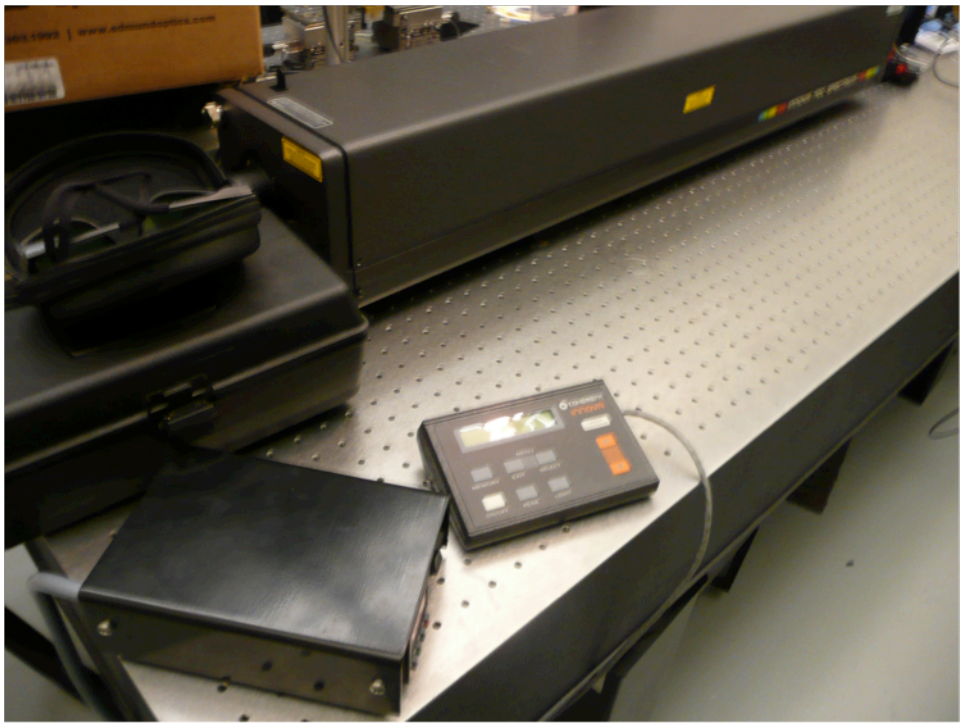

Figure A.1: The Coherent Innova 70C Spectrum Ar-Kr tunable laser used for excitation of nanocrystal-polymer films.

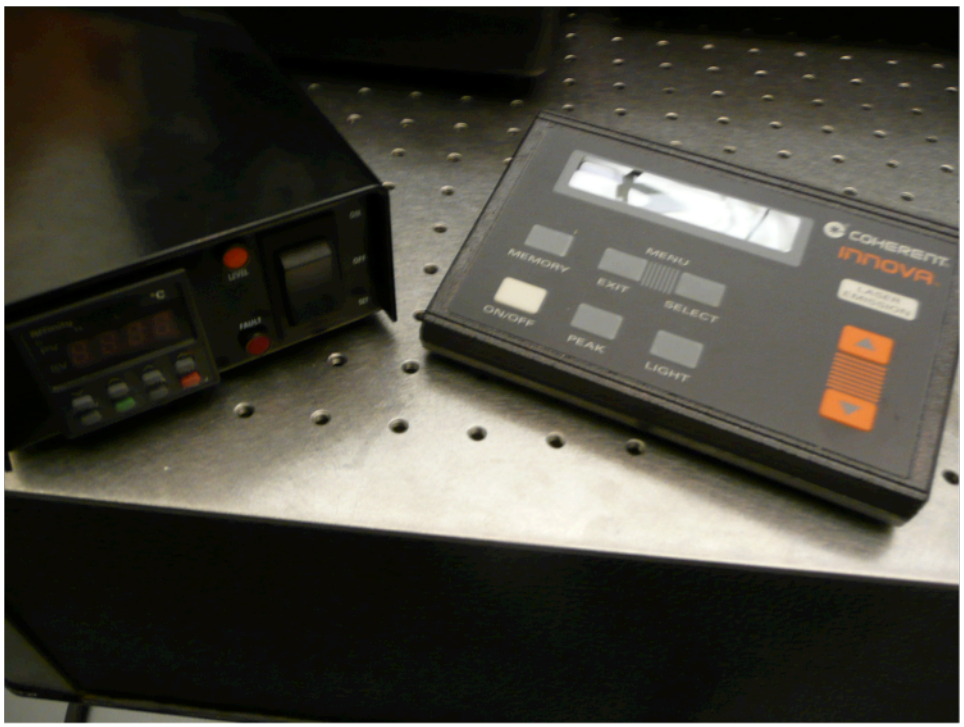

Figure A.2: The Affinity control module (left) used to change settings for the chiller and the Coherent control module (right) used to change the laser settings and read any error messages concerning the laser operation.

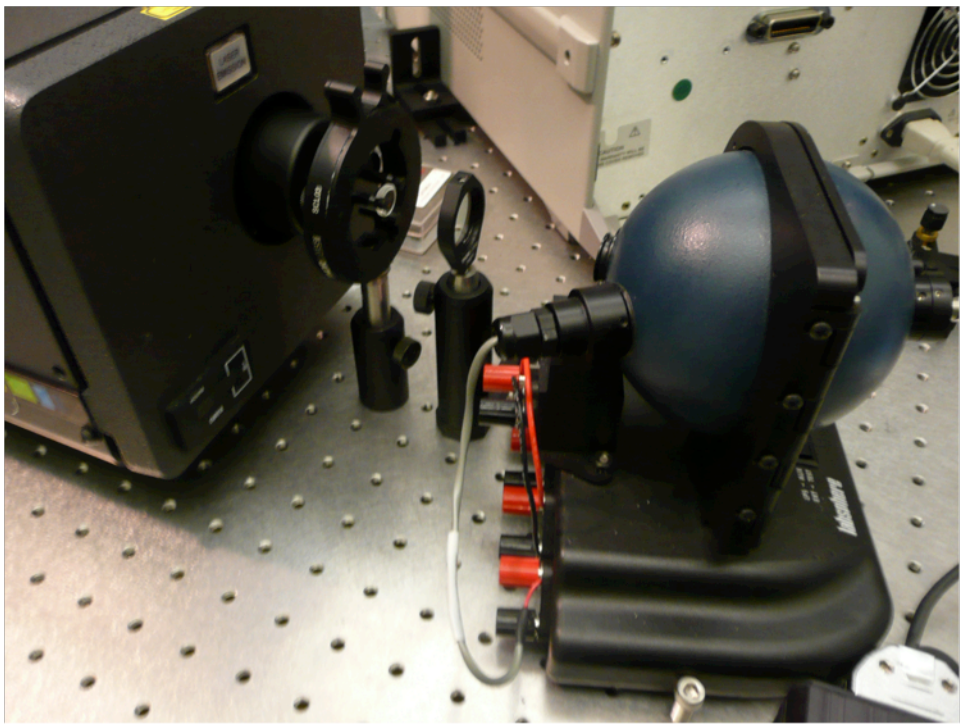

Figure A.3: The setup for laser excitation of nanocrystal-polymer films using the multiline UV setting, with a lens to diverge the laser beam, a filter to block visible light from the laser and only allow UV light through, and the 4" Labsphere integrating sphere used to collect and measure the light emitted by the film.

APPENDIX B

INTEGRATING SPHERE MEASUREMENT PROCEDURE

1. First, plug in the USB cable from the spectrometer (small black box with Labsphere logo in white on top) to the computer. Be sure to always plug the cable into the exact same port on the computer, otherwise I have found that it will try to reinstall drivers and then it will not work correctly again until you have spent hours uninstalling the program and deleted things manually from the Windows registry.
2. Make sure the fiber cable coming from the spectrometer is plugged into the exit port of the sphere you want to use, then start up the SLMS LED program.
3. It will ask you to do a dark scan, so make sure the sphere is closed and no light sources are powered inside the sphere and click OK.
4. After that has finished (it will take several minutes), you are presented with the main screen. There should already be a calibration, and it will use the files from the last time the software was run. They should be labeled something along the lines of 4inch or 10inch, depending on which sphere you are using. These settings can be changed in the Calibration menu.
5. Power on the source you want to measure, which is easily done with the Keithley Sourcemeter and the red/black plugs attached to either the cable with bare wires (10" sphere) or to the back of the junction box (4" sphere). For LEDs, polarity matters, so if your LED doesn't light up when you have the correct power supplied, just switch the wires.
6. Next, click on Set Scan Exposure to set the exposure time (in milliseconds, or ms) so that the spectrometer has sufficient light but will not be overexposed (80-85% saturation). You can type in a specific time and then test it by clicking Test Exposure, or set an initial time and click Auto Exposure, where it will keep testing different exposure times until it finds one with the saturation between 80-85%, and can take several minutes or more depending on the light level. I have found that going over 20 s, or 20000 ms, causes the signal to become more noisy, thus I stick to 20000 ms or less. With the exposure set correctly, click Apply.
7. Before executing a measurement, make sure the scan settings are how you want them. These include the number of scans to average (if your source is not as stable, increase this number, but beware it will take longer) and the wavelength aperture (basically the wavelength range that is displayed and used for calculations of the emission properties).
8. Next, click on Test Scan No Prompt to take a measurement. This can take some time depending on your exposure time and number of scans to average. Do not open the sphere while it is taking a measurement.
9. When the measurement is done, you can take more scans, up to 10 per data file. I find it best to save the .SCN file in case you need to open up your data again in the SLMS LED program, and then the .DT0 (raw spectral data) and .DT3 (calculated data report) files which you can save as .XLS files and then open up in Excel or similar. There are other reports with different parameters that it calculates that you can export, but these are just my personal favorites of how the data is displayed.
10. Any other questions, refer to the user manual (a PDF file, should be on a blue Labsphere CD in the lab somewhere).

11. Calibration note: to calibrate the 4” sphere, the Keithley must be used to power the small calibration lamp with two leads (SCL-050, Gilway 187-1 lamp) at 4.2V and 1.05A. To calibrate the 10” sphere using the larger calibration lamp that screws into the socket, the Labsphere power supply can be used. The calibration procedure is the same for both spheres, and is detailed in the user manual.

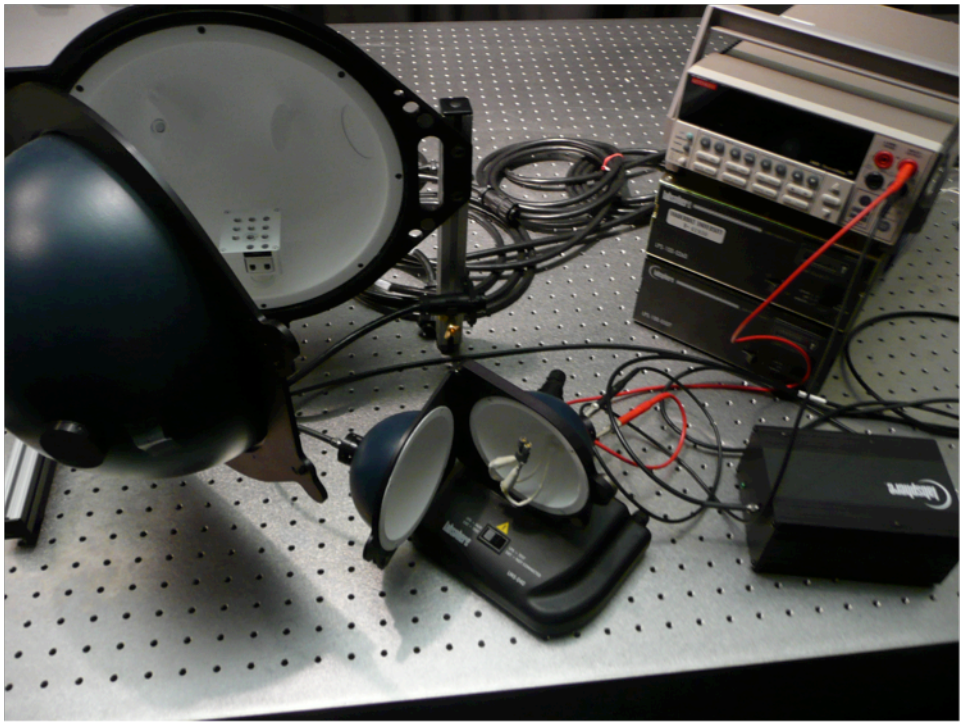

Figure B.1: The setup for measurement of LED sources and light emitted by nanocrystal-polymer films, including 4” (lower middle) and 10” (upper left) Labsphere integrating spheres, as well as the spectrometer module (lower right) and the power supplies that power the calibration lamps or LED sources (upper right).

APPENDIX C

DIELECTRIC MIRROR REFLECTANCE CALCULATION CODE

```
% Program designed to calculate the reflectivity of a dielectric
% multilayer chirped mirror.

% User specifies number of periods, design wavelength(s), substrate
% index, and indices of the dielectric materials.
% Program calculates layer thicknesses to achieve
% quarter-wavelength stack.

clear

% Enter the range and increment for the mirrors in microns
% (start:increment:end)

mirror_wavelength = 0.500:0.100:0.900;

% Enter the number of periods at each mirror wavelength

num_periods = 10;

% Enter the substrate refractive index

Substrate_index = 1.45; %SiO2

% Enter the refractive indices of the dielectric materials to be used

Dielectrica_index = 1.45; %SiO2
Dielectricb_index = 1.95; %HfO2

% Create array for wavelengths between 0.1 microns and 0.8 microns
% (increments of 0.001 microns), this is the range that the
% reflectance will be calculated over

all_wavelengths = 0.000:0.001:2.500;
wavelength_increment = 0.001;

epsilon = 8.85418781762*10^-12;   % electric permittivity constant
mu = 1.25663706144*10^-6;         % magnetic permeability constant
c1 = sqrt(epsilon/mu);            % used in coefficient of reflectivity
c2 = c1*Substrate_index;          % used in coefficient of reflectivity

count = 0;
total_thickness = 0;

% Enter the incident angle (here it is 45 degrees)

incidentangle = pi/180*45;

for j = 1:size(all_wavelengths,2)

    % sets the wavelength for the reflectivity calculation
    wavelength(j) = all_wavelengths(1) + count;

    % sets the overall matrix to 1
    M_total = 1;
```

```
% calculated low index 1/8 wavelength layer thickness for ends
Datf = mirror_wavelength(1)/(4*2*Dielectrica_index);

A(j) =2*pi*Dielectrica_index*Datf*cos(incidentangle)/wavelength(j);
B(j) = sqrt(epsilon/mu)*Dielectrica_index;

% Create characteristic matrix for each layer
M_low = [cos(A(j)), i*sin(A(j))/B(j); i*sin(A(j))*B(j), cos(A(j))];

% Characteristic matrix for entire multilayer structure
M_total = M_total*M_low;

for k = 1:size(mirror_wavelength,2)

    % calculated low index layer thickness
    Dat(k) = mirror_wavelength(k)/(4*Dielectrica_index);

    % calculated low index 1/8 layer thickness for ends
    Datf(k) = mirror_wavelength(k)/(4*2*Dielectrica_index);

    % calculated high index layer thickness
    Dbt(k) = mirror_wavelength(k)/(4*Dielectricb_index);

    A(j,k) = 2*pi*Dielectrica_index*Dat(k)
             *cos(incidentangle)/wavelength(j);
    B(j,k) = sqrt(epsilon/mu)*Dielectrica_index;
    C(j,k) = 2*pi*Dielectricb_index*Dbt(k)
             *cos(incidentangle)/wavelength(j);
    D(j,k) = sqrt(epsilon/mu)*Dielectricb_index;

    % Create characteristic matrix for each layer
    M_low = [cos(A(j,k)) , i*sin(A(j,k))/B(j,k) ;
            i*sin(A(j,k))*B(j,k) , cos(A(j,k))];
    M_high = [cos(C(j,k)) , i*sin(C(j,k))/D(j,k) ;
             i*sin(C(j,k))*D(j,k) , cos(C(j,k))];

    % Characteristic matrix for one period
    M_period = M_high*M_low;

    % Characteristic matrix for entire multilayer structure
    M_total = M_total*((M_period)^num_periods);

end

A(j,k) = 2*pi*Dielectrica_index*Datf(k)
         *cos(incidentangle)/wavelength(j);
M_low = [cos(A(j,k)) , i*sin(A(j,k))/B(j,k) ;
        i*sin(A(j,k))*B(j,k) , cos(A(j,k))];
M_total = M_total*M_high*M_low;

% Reflectivity coefficient for particular wavelength of multilayer
  structure
r = (c1*M_total(1) + c1*c2*M_total(3) - M_total(2)
    - c2*M_total(4))/(c1*M_total(1) + c1*c2*M_total(3)
    + M_total(2) + c2*M_total(4));
```

```
    % Reflectance for a particular wavelength
    Reflectance(j) = (abs(r))^2;

    % Increment count for wavelength
    count = count + wavelength_increment;
end

for p = 1:size(mirror_wavelength,2)
    total_thickness = total_thickness+(Dat(p)+Dbt(p))*num_periods;
end

% Plot reflectivity as a function of wavelength

nm = wavelength*1000;
figure
plot(nm,Reflectance,'b');

title('Dielectric Multilayer Mirror')
axis([nm(1) nm(size(nm,2)) 0 1])
xlabel('Wavelength (nm)')
ylabel('Reflectance')
grid
hold on

% Open file for data storage
fid = fopen('Data.xls','a');
fprintf(fid,'Total thickness of structure = %3.4f
microns\n',total_thickness);

% Write reflectance data to file
fprintf(fid,'wavelength (in microns),reflectivity\n');

for z=1:1:size(wavelength,2);
    fprintf(fid,'%2.6f  %2.6f\n',wavelength(z),Reflectance(z));
end

fprintf(fid,'\n\n\n');

hold off        % ensures that future curves will not be plotted on
                  this graph
fclose(fid);    % closes the file to which the data was written
```

APPENDIX D

RAYLEIGH AND MIE SCATTERING CALCULATION CODE

**Note that this code requires a .fig file named mieandrayleighgraph.fig that is used as the graphical user interface (GUI) to input parameters and display the results in graphs.*

```
function varargout = mieandrayleighgraph(varargin)
% RAYLEIGH M-file for mieandrayleighgraph.fig
% RAYLEIGH, by itself, creates lambda0 new RAYLEIGH or raises the
% existing singleton*.

% H = RAYLEIGH returns the handle to lambda0 new RAYLEIGH or the handle
% to the existing singleton*.

% RAYLEIGH('CALLBACK',hObject,eventData,handles,...) calls the local
% function named CALLBACK in RAYLEIGH.M with the given input arguments.

% RAYLEIGH('Property','Value',...) creates lambda0 new RAYLEIGH or
% raises the existing singleton*.  Starting from the left, property
% value pairs are applied to the GUI before rayleigh_OpeningFunction
% gets called.  An unrecognized property name or invalid value makes
% property application stop.  All inputs are passed to
% rayleigh_OpeningFcn via varargin.
%
% *See GUI Options on GUIDE's Tools menu.  Choose "GUI allows only one
% instance to run (singleton)".
%
% See also: GUIDE, GUIDATA, GUIHANDLES

% Edit the above text to modify the response to help rayleigh
% Last Modified by GUIDE v2.5 03-Jun-2008 13:53:08
% Begin initialization code - DO NOT EDIT
gui_Singleton = 1;
gui_State=struct('gui_Name',       mfilename, ...
                 'gui_Singleton',  gui_Singleton, ...
                 'gui_OpeningFcn', @mieandrayleighgraph_OpeningFcn, ...
                 'gui_OutputFcn',  @mieandrayleighgraph_OutputFcn, ...
                 'gui_LayoutFcn',  [] , ...
                 'gui_Callback',   []);
if nargin && ischar(varargin{1})
    gui_State.gui_Callback = str2func(varargin{1});
end

if nargout
    [varargout{1:nargout}] = gui_mainfcn(gui_State, varargin{:});
else
    gui_mainfcn(gui_State, varargin{:});
end
% End initialization code - DO NOT EDIT

% --- Executes just before rayleigh is made visible.
function mieandrayleighgraph_OpeningFcn(hObject, eventdata, handles,
varargin)
% This function has no output args, see OutputFcn.
% hObject    handle to figure
% eventdata  reserved - to be defined in lambda0 future version of
%            MATLAB
% handles    structure with handles and user data (see GUIDATA)
% varargin   command line arguments to rayleigh (see VARARGIN)
```

```
% Choose default command line output for rayleigh
handles.output = hObject;

% Update handles structure
guidata(hObject, handles);

% UIWAIT makes rayleigh wait for user response (see UIRESUME)
% uiwait(handles.figure1);

% --- Outputs from this function are returned to the command line.
function varargout = mieandrayleighgraph_OutputFcn(hObject, eventdata,
handles)
% varargout  cell array for returning output args (see VARARGOUT);
% hObject    handle to figure
% eventdata  reserved - to be defined in lambda0 future version of
%            MATLAB
% handles    structure with handles and user data (see GUIDATA)

% Get default command line output from handles structure
varargout{1} = handles.output;

function lambda0_Callback(hObject, eventdata, handles)
% hObject    handle to lambda0 (see GCBO)
% eventdata  reserved - to be defined in lambda0 future version of
%            MATLAB
% handles    structure with handles and user data (see GUIDATA)
% Hints: get(hObject,'String') returns contents of lambda0 as text
%        str2double(get(hObject,'String')) returns contents of lambda0
as lambda0 double
lambda0 = str2double(get(handles.lambda0,'String'));
% --- Executes during object creation, after setting all properties.
function lambda0_CreateFcn(hObject, eventdata, handles)
% hObject    handle to lambda0 (see GCBO)
% eventdata  reserved - to be defined in lambda0 future version of
%            MATLAB
% handles    empty - handles not created until after all CreateFcns
%            called
% Hint: edit controls usually have lambda0 white background on Windows.
%       See ISPC and COMPUTER.
if ispc && isequal(get(hObject,'BackgroundColor'),
get(0,'defaultUicontrolBackgroundColor'))
    set(hObject,'BackgroundColor','white');
end

function lambda0start_Callback(hObject, eventdata, handles)
% hObject    handle to lambda0start (see GCBO)
% eventdata  reserved - to be defined in a future version of MATLAB
% handles    structure with handles and user data (see GUIDATA)
% Hints: get(hObject,'String') returns contents of lambda0start as text
%        str2double(get(hObject,'String')) returns contents of
%        lambda0start as a double
lambda0start = str2double(get(handles.lambda0start,'String'));
% --- Executes during object creation, after setting all properties.
function lambda0start_CreateFcn(hObject, eventdata, handles)
% hObject    handle to lambda0start (see GCBO)
% eventdata  reserved - to be defined in a future version of MATLAB
```

```
% handles    empty - handles not created until after all CreateFcns
%            called
% Hint: edit controls usually have a white background on Windows.
%       See ISPC and COMPUTER.
if ispc && isequal(get(hObject,'BackgroundColor'),
get(0,'defaultUicontrolBackgroundColor'))
    set(hObject,'BackgroundColor','white');
end

function lambda0end_Callback(hObject, eventdata, handles)
% hObject    handle to lambda0end (see GCBO)
% eventdata  reserved - to be defined in a future version of MATLAB
% handles    structure with handles and user data (see GUIDATA)
% Hints: get(hObject,'String') returns contents of lambda0end as text
%        str2double(get(hObject,'String')) returns contents of
%        lambda0end as a double
lambda0end = str2double(get(handles.lambda0end,'String'));
% --- Executes during object creation, after setting all properties.
function lambda0end_CreateFcn(hObject, eventdata, handles)
% hObject    handle to lambda0end (see GCBO)
% eventdata  reserved - to be defined in a future version of MATLAB
% handles    empty - handles not created until after all CreateFcns
%            called
% Hint: edit controls usually have a white background on Windows.
%       See ISPC and COMPUTER.
if ispc && isequal(get(hObject,'BackgroundColor'),
get(0,'defaultUicontrolBackgroundColor'))
    set(hObject,'BackgroundColor','white');
end

function lambda0inc_Callback(hObject, eventdata, handles)
% hObject    handle to lambda0inc (see GCBO)
% eventdata  reserved - to be defined in a future version of MATLAB
% handles    structure with handles and user data (see GUIDATA)
% Hints: get(hObject,'String') returns contents of lambda0inc as text
%        str2double(get(hObject,'String')) returns contents of
%        lambda0inc as a double
lambda0inc = str2double(get(handles.lambda0inc,'String'));
% --- Executes during object creation, after setting all properties.
function lambda0inc_CreateFcn(hObject, eventdata, handles)
% hObject    handle to lambda0inc (see GCBO)
% eventdata  reserved - to be defined in a future version of MATLAB
% handles    empty - handles not created until after all CreateFcns
%            called
% Hint: edit controls usually have a white background on Windows.
%       See ISPC and COMPUTER.
if ispc && isequal(get(hObject,'BackgroundColor'),
get(0,'defaultUicontrolBackgroundColor'))
    set(hObject,'BackgroundColor','white');
end

function a_Callback(hObject, eventdata, handles)
% hObject    handle to a (see GCBO)
% eventdata  reserved - to be defined in a future version of MATLAB
% handles    structure with handles and user data (see GUIDATA)
% Hints: get(hObject,'String') returns contents of a as text
%        str2double(get(hObject,'String')) returns contents of a as a
%        double
```

```
a = str2double(get(handles.a,'String'));
% --- Executes during object creation, after setting all properties.
function a_CreateFcn(hObject, eventdata, handles)
% hObject    handle to a (see GCBO)
% eventdata  reserved - to be defined in a future version of MATLAB
% handles    empty - handles not created until after all CreateFcns
%            called
% Hint: edit controls usually have a white background on Windows.
%       See ISPC and COMPUTER.
if ispc && isequal(get(hObject,'BackgroundColor'),
get(0,'defaultUicontrolBackgroundColor'))
    set(hObject,'BackgroundColor','white');
end

function astart_Callback(hObject, eventdata, handles)
% hObject    handle to astart (see GCBO)
% eventdata  reserved - to be defined in lambda0 future version of
MATLAB
% handles    structure with handles and user data (see GUIDATA)
% Hints: get(hObject,'String') returns contents of astart as text
%        str2double(get(hObject,'String')) returns contents of astart
%        as lambda0 double
astart = str2double(get(handles.astart,'String'));
% --- Executes during object creation, after setting all properties.
function astart_CreateFcn(hObject, eventdata, handles)
% hObject    handle to astart (see GCBO)
% eventdata  reserved - to be defined in lambda0 future version of
%            MATLAB
% handles    empty - handles not created until after all CreateFcns
%            called
% Hint: edit controls usually have lambda0 white background on Windows.
%       See ISPC and COMPUTER.
if ispc && isequal(get(hObject,'BackgroundColor'),
get(0,'defaultUicontrolBackgroundColor'))
    set(hObject,'BackgroundColor','white');
end

function aend_Callback(hObject, eventdata, handles)
% hObject    handle to aend (see GCBO)
% eventdata  reserved - to be defined in lambda0 future version of
%            MATLAB
% handles    structure with handles and user data (see GUIDATA)
% Hints: get(hObject,'String') returns contents of aend as text
%        str2double(get(hObject,'String')) returns contents of aend as
%        lambda0 double
aend = str2double(get(handles.aend,'String'));
% --- Executes during object creation, after setting all properties.
function aend_CreateFcn(hObject, eventdata, handles)
% hObject    handle to aend (see GCBO)
% eventdata  reserved - to be defined in lambda0 future version of
%            MATLAB
% handles    empty - handles not created until after all CreateFcns
%            called
% Hint: edit controls usually have lambda0 white background on Windows.
%       See ISPC and COMPUTER.
if ispc && isequal(get(hObject,'BackgroundColor'),
get(0,'defaultUicontrolBackgroundColor'))
    set(hObject,'BackgroundColor','white');
```

```
end

function ainc_Callback(hObject, eventdata, handles)
% hObject    handle to ainc (see GCBO)
% eventdata  reserved - to be defined in lambda0 future version of
%            MATLAB
% handles    structure with handles and user data (see GUIDATA)
% Hints: get(hObject,'String') returns contents of ainc as text
%        str2double(get(hObject,'String')) returns contents of ainc as
lambda0 double
ainc = str2double(get(handles.ainc,'String'));
% --- Executes during object creation, after setting all properties.
function ainc_CreateFcn(hObject, eventdata, handles)
% hObject    handle to ainc (see GCBO)
% eventdata  reserved - to be defined in lambda0 future version of
%            MATLAB
% handles    empty - handles not created until after all CreateFcns
%            called
% Hint: edit controls usually have lambda0 white background on Windows.
%       See ISPC and COMPUTER.
if ispc && isequal(get(hObject,'BackgroundColor'),
get(0,'defaultUicontrolBackgroundColor'))
    set(hObject,'BackgroundColor','white');
end

function npart_Callback(hObject, eventdata, handles)
% hObject    handle to npart (see GCBO)
% eventdata  reserved - to be defined in lambda0 future version of
%            MATLAB
% handles    structure with handles and user data (see GUIDATA)
% Hints: get(hObject,'String') returns contents of npart as text
%        str2double(get(hObject,'String')) returns contents of npart as
%        lambda0 double
npart = str2double(get(handles.npart,'String'));
% --- Executes during object creation, after setting all properties.
function npart_CreateFcn(hObject, eventdata, handles)
% hObject    handle to npart (see GCBO)
% eventdata  reserved - to be defined in lambda0 future version of
%            MATLAB
% handles    empty - handles not created until after all CreateFcns
%            called
% Hint: edit controls usually have lambda0 white background on Windows.
%       See ISPC and COMPUTER.
if ispc && isequal(get(hObject,'BackgroundColor'),
get(0,'defaultUicontrolBackgroundColor'))
    set(hObject,'BackgroundColor','white');
end

function kpart_Callback(hObject, eventdata, handles)
% hObject    handle to kpart (see GCBO)
% eventdata  reserved - to be defined in a future version of MATLAB
% handles    structure with handles and user data (see GUIDATA)

% Hints: get(hObject,'String') returns contents of kpart as text
%        str2double(get(hObject,'String')) returns contents of kpart as
%        a double
```

```
% --- Executes during object creation, after setting all properties.
function kpart_CreateFcn(hObject, eventdata, handles)
% hObject    handle to kpart (see GCBO)
% eventdata  reserved - to be defined in a future version of MATLAB
% handles    empty - handles not created until after all CreateFcns
%            called

% Hint: edit controls usually have a white background on Windows.
%       See ISPC and COMPUTER.
if ispc && isequal(get(hObject,'BackgroundColor'),
get(0,'defaultUicontrolBackgroundColor'))
    set(hObject,'BackgroundColor','white');
end

function nmed_Callback(hObject, eventdata, handles)
% hObject    handle to nmed (see GCBO)
% eventdata  reserved - to be defined in lambda0 future version of
%            MATLAB
% handles    structure with handles and user data (see GUIDATA)
% Hints: get(hObject,'String') returns contents of nmed as text
%        str2double(get(hObject,'String')) returns contents of nmed as
%        lambda0 double
nmed = str2double(get(handles.nmed,'String'));
% --- Executes during object creation, after setting all properties.
function nmed_CreateFcn(hObject, eventdata, handles)
% hObject    handle to nmed (see GCBO)
% eventdata  reserved - to be defined in lambda0 future version of
%            MATLAB
% handles    empty - handles not created until after all CreateFcns
%            called

% Hint: edit controls usually have lambda0 white background on Windows.
%       See ISPC and COMPUTER.
if ispc && isequal(get(hObject,'BackgroundColor'),
get(0,'defaultUicontrolBackgroundColor'))
    set(hObject,'BackgroundColor','white');
end

function Nconc_Callback(hObject, eventdata, handles)
% hObject    handle to Nconc (see GCBO)
% eventdata  reserved - to be defined in lambda0 future version of
%            MATLAB
% handles    structure with handles and user data (see GUIDATA)
% Hints: get(hObject,'String') returns contents of Nconc as text
%        str2double(get(hObject,'String')) returns contents of Nconc as
%        lambda0 double
Nconc = str2double(get(handles.Nconc,'String'));
% --- Executes during object creation, after setting all properties.
function Nconc_CreateFcn(hObject, eventdata, handles)
% hObject    handle to Nconc (see GCBO)
% eventdata  reserved - to be defined in lambda0 future version of
%            MATLAB
% handles    empty - handles not created until after all CreateFcns
%            called
% Hint: edit controls usually have lambda0 white background on Windows.
%       See ISPC and COMPUTER.
if ispc && isequal(get(hObject,'BackgroundColor'),
```

```
get(0,'defaultUicontrolBackgroundColor'))
    set(hObject,'BackgroundColor','white');
end


% --- Executes on button press in calculatebutton.
function calculatebutton_Callback(hObject, eventdata, handles)
% hObject    handle to calculatebutton (see GCBO)
% eventdata  reserved - to be defined in lambda0 future version of
%            MATLAB
% handles    structure with handles and user data (see GUIDATA)
set(handles.calculatebutton,'ForegroundColor',[1 0 0]);
set(handles.calculatebutton,'String','Thinking...');
lambda0 = str2double(get(handles.lambda0,'String'));
lambda0start = str2double(get(handles.lambda0start,'String'));
lambda0end = str2double(get(handles.lambda0end,'String'));
lambda0inc = str2double(get(handles.lambda0inc,'String'));
a = str2double(get(handles.a,'String'));
astart = str2double(get(handles.astart,'String'));
aend = str2double(get(handles.aend,'String'));
ainc = str2double(get(handles.ainc,'String'));
npart = str2double(get(handles.npart,'String'));
kpart = str2double(get(handles.kpart,'String'));
mpart = (npart - i*kpart);
nmed = str2double(get(handles.nmed,'String'));
Nconc = str2double(get(handles.Nconc,'String'));

if get(handles.crossunits,'Value') == 1
    multcross = 1;
    crossunitsdisplay = 'nm';
end
if get(handles.crossunits,'Value') == 2
    multcross = 1E-6;
    crossunitsdisplay = 'um';
end
if get(handles.crossunits,'Value') == 3
    multcross = 1E-14;
    crossunitsdisplay = 'cm';
end
if get(handles.crossunits,'Value') == 4
    multcross = 1E-18;
    crossunitsdisplay = 'm';
end
if get(handles.coeffunits,'Value') == 1
    multcoeff = 1;
    coeffunitsdisplay = 'nm';
end
if get(handles.coeffunits,'Value') == 2
    multcoeff = 1E-3;
    coeffunitsdisplay = 'um';
end
if get(handles.coeffunits,'Value') == 3
    multcoeff = 1E-7;
    coeffunitsdisplay = 'cm';
end
if get(handles.coeffunits,'Value') == 4
    multcoeff = 1E-9;
    coeffunitsdisplay = 'm';
```

```
end

if get(handles.whichgraph,'String') == '1'
    all_wavelengths = lambda0start:lambda0inc:lambda0end;
    first_wavelength = all_wavelengths(1);
    m = npart/nmed;
    count = 0;
    for j = 1:numel(all_wavelengths)
        wavelength(j) = first_wavelength + count;
        xdata(j) = 2*pi*nmed*a/wavelength(j);
        kmed = xdata(j)/a;
        rho(j) = 2*xdata(j)/(abs(m-1));
        x = xdata(j);
        nmax=round(2+x+4*x.^(1/3));

        results=mie(m,x);
        qext=results(1);
        qsca=results(2);
        qabs=results(3);

        mieefficsca(j) = qsca;
        miecrosssca(j) = multcross*mieefficsca(j)*pi*a^2;
        miecoeffsca(j) = 1/multcoeff^3*Nconc*miecrosssca(j);

        crossabs(j) =
multcross*8*pi*pi*nmed/wavelength(j)*real(a^3*((mpart^2-
nmed^2)/(mpart^2+2*nmed^2)));
        efficabs(j) = 1/multcross*crossabs(j)/pi/a^2;
        coeffabs(j) = 1/multcoeff^3*Nconc*crossabs(j);

        mieefficext(j) = efficabs(j) + mieefficsca(j);
        miecrossext(j) = crossabs(j) + miecrosssca(j);
        miecoeffext(j) = coeffabs(j) + miecoeffsca(j);

        raycrosssca(j) =
multcross*8*pi/3*((2*pi*nmed/wavelength(j))^4)*(a^6*((npart/nmed)^2-
1)/((npart/nmed)^2+2)^2);
        rayefficsca(j) = 1/multcross*raycrosssca(j)/pi/a^2;
        raycoeffsca(j) = 1/multcoeff^3*Nconc*raycrosssca(j);

        raycrossext(j) = crossabs(j) + raycrosssca(j);
        rayefficext(j) = efficabs(j) + rayefficsca(j);
        raycoeffext(j) = coeffabs(j) + raycoeffsca(j);

        count = count + lambda0inc;
    end
    axes(handles.scacrossgraph);
    cla;
    plot(wavelength,miecrosssca,wavelength,raycrosssca);
    legend('Mie','Rayleigh');
    xlabel('Wavelength (nm)');
    ylabel(['Scattering Cross Section (',crossunitsdisplay,'^{2})']);
    grid;
    axes(handles.scaefficgraph);
    cla;
    plot(wavelength,mieefficsca,wavelength,rayefficsca);
    legend('Mie','Rayleigh');
```

```
xlabel('Wavelength (nm)');
ylabel('Scattering Efficiency (unitless)');
grid;
axes(handles.scacoeffgraph);
cla;
plot(wavelength,miecoeffsca,wavelength,raycoeffsca);
legend('Mie','Rayleigh');
xlabel('Wavelength (nm)');
ylabel(['Scattering Coefficient (',coeffunitsdisplay,'^{-1})']);
grid;
axes(handles.abscrossgraph);
cla;
plot(wavelength,crossabs);
xlabel('Wavelength (nm)');
ylabel(['Absorption Cross Section (',crossunitsdisplay,'^{2})']);
grid;
axes(handles.absefficgraph);
cla;
plot(wavelength,efficabs);
xlabel('Wavelength (nm)');
ylabel('Absorption Efficiency (unitless)');
grid;
axes(handles.abscoeffgraph);
cla;
plot(wavelength,coeffabs);
xlabel('Wavelength (nm)');
ylabel(['Absorption Coefficient (',coeffunitsdisplay,'^{-1})']);
grid;
axes(handles.extcrossgraph);
cla;
plot(wavelength,miecrossext,wavelength,raycrossext);
legend('Mie','Rayleigh');
xlabel('Wavelength (nm)');
ylabel(['Extinction Cross Section (',crossunitsdisplay,'^{2})']);
grid;
axes(handles.extefficgraph);
cla;
plot(wavelength,mieefficext,wavelength,rayefficext);
legend('Mie','Rayleigh');
xlabel('Wavelength (nm)');
ylabel('Extinction Efficiency (unitless)');
grid;
axes(handles.extcoeffgraph);
cla;
plot(wavelength,miecoeffext,wavelength,raycoeffext);
legend('Mie','Rayleigh');
xlabel('Wavelength (nm)');
ylabel(['Extinction Coefficient (',coeffunitsdisplay,'^{-1})']);
grid;
if get(handles.excelfile,'Value') == 1
    fid = fopen(get(handles.excelfilename,'String'),'a');
    fprintf(fid,'Particle radius (nm) \t');
    fprintf(fid,'%2.6f \n',a);
    fprintf(fid,'Refractive index of particle \t');
    fprintf(fid,'%2.6f \n',npart);
    fprintf(fid,'Refractive index of medium \t');
    fprintf(fid,'%2.6f \n',nmed);
    fprintf(fid,'N (particles per nm^3) \t');
```

```
        fprintf(fid,'%2.6f \n',Nconc);
        fprintf(fid,['Wavelength (nm) \t Absorption cross section
(',crossunitsdisplay,'^2) \t Absorption efficiency (unitless) \t
Absorption coefficient (',coeffunitsdisplay,'^-1) \n']);
        for z=1:numel(all_wavelengths);
            fprintf(fid,'%2.6f \t %2.6E \t %2.6E \t %2.6E
\n',wavelength(z),crossabs(z),efficabs(z),coeffabs(z));
        end
        fprintf(fid,['Wavelength (nm) \t Mie Scattering cross section
(',crossunitsdisplay,'^2) \t Rayleigh Scattering cross section
(',crossunitsdisplay,'^2) \t Mie Scattering efficiency (unitless) \t
Rayleigh Scattering efficiency (unitless) \t Mie Scattering coefficient
(',coeffunitsdisplay,'^-1) \t Rayleigh Scattering coefficient
(',coeffunitsdisplay,'^-1) \n']);
        for z=1:numel(all_wavelengths);
            fprintf(fid,'%2.6f \t %2.6E \t %2.6E \t %2.6E \t %2.6E \t
%2.6E \t %2.6E
\n',wavelength(z),miecrosssca(z),raycrosssca(z),mieefficsca(z),rayeffic
sca(z),miecoeffsca(z),raycoeffsca(z));
        end
        fprintf(fid,['Wavelength (nm) \t Mie Extinction cross section
(',crossunitsdisplay,'^2) \t Rayleigh Extinction cross section
(',crossunitsdisplay,'^2) \t Mie Extinction efficiency (unitless) \t
Rayleigh Extinction efficiency (unitless) \t Mie Extinction coefficient
(',coeffunitsdisplay,'^-1) \t Rayleigh Extinction coefficient
(',coeffunitsdisplay,'^-1) \n']);
        for z=1:numel(all_wavelengths);
            fprintf(fid,'%2.6f \t %2.6E \t %2.6E \t %2.6E \t %2.6E \t
%2.6E \t %2.6E
\n',wavelength(z),miecrossext(z),raycrossext(z),mieefficext(z),rayeffic
ext(z),miecoeffext(z),raycoeffext(z));
        end
        fprintf(fid,'\n\n\n');
        fclose(fid);
    end
else
    all_sizes = astart:ainc:aend;
    first_size = all_sizes(1);
    m = npart/nmed;
    count = 0;
    for j = 1:numel(all_sizes)
        sizes(j) = first_size + count;
        xdata(j) = 2*pi*nmed*sizes(j)/lambda0;
        kmed = xdata(j)/sizes(j);
        rho(j) = 2*xdata(j)/(abs(m-1));
        x = xdata(j);

        nmax=round(2+x+4*x.^(1/3));

        results=mie(m,x);
        qext=results(1);
        qsca=results(2);
        qabs=results(3);

        mieefficsca(j) = qsca;
        miecrosssca(j) = multcross*mieefficsca(j)*pi*(sizes(j))^2;
        miecoeffsca(j) = 1/multcoeff^3*Nconc*miecrosssca(j);
```

```
        crossabs(j) =
multcross*8*pi*pi*nmed/lambda0*real((sizes(j))^3*((mpart^2-
nmed^2)/(mpart^2+2*nmed^2)));
        efficabs(j) = crossabs(j)/pi/(sizes(j))^2;
        coeffabs(j) = 1/multcoeff^3*Nconc*crossabs(j);

        mieefficext(j) = efficabs(j) + mieefficsca(j);
        miecrossext(j) = crossabs(j) + miecrosssca(j);
        miecoeffext(j) = coeffabs(j) + miecoeffsca(j);

        raycrosssca(j) =
multcross*8*pi/3*((2*pi*nmed/lambda0)^4)*((sizes(j))^6*((npart/nmed)^2-
1)/((npart/nmed)^2+2)^2);
        rayefficsca(j) = raycrosssca(j)/pi/(sizes(j))^2;
        raycoeffsca(j) = 1/multcoeff^3*Nconc*raycrosssca(j);

        raycrossext(j) = crossabs(j) + raycrosssca(j);
        rayefficext(j) = efficabs(j) + rayefficsca(j);
        raycoeffext(j) = coeffabs(j) + raycoeffsca(j);

        count = count + ainc;
    end
    if get(handles.whichgraph,'String') == '2'
        axes(handles.scacrossgraph);
        cla;
        plot(sizes,miecrosssca,sizes,raycrosssca);
        legend('Mie','Rayleigh');
        xlabel('Particle Radius (nm)');
        ylabel(['Scattering Cross Section
(',crossunitsdisplay,'^{2})']);
        grid;
        axes(handles.scaefficgraph);
        cla;
        plot(sizes,mieefficsca,sizes,rayefficsca);
        legend('Mie','Rayleigh');
        xlabel('Particle Radius (nm)');
        ylabel('Scattering Efficiency (unitless)');
        grid;
        axes(handles.scacoeffgraph);
        cla;
        plot(sizes,miecoeffsca,sizes,raycoeffsca);
        legend('Mie','Rayleigh');
        xlabel('Particle Radius (nm)');
        ylabel(['Scattering Coefficient (',coeffunitsdisplay,'^{ -
1})']);
        grid;
        axes(handles.abscrossgraph);
        cla;
        plot(sizes,crossabs);
        xlabel('Particle Radius (nm)');
        ylabel(['Absorption Cross Section
(',crossunitsdisplay,'^{2})']);
        grid;
        axes(handles.absefficgraph);
        cla;
        plot(sizes,efficabs);
```

```
        xlabel('Particle Radius (nm)');
        ylabel('Absorption Efficiency (unitless)');
        grid;
        axes(handles.abscoeffgraph);
        cla;
        plot(sizes,coeffabs);
        xlabel('Particle Radius (nm)');
        ylabel(['Absorption Coefficient (',coeffunitsdisplay,'^{ -
1})']);
        grid;
        axes(handles.extcrossgraph);
        cla;
        plot(sizes,miecrossext,sizes,raycrossext);
        legend('Mie','Rayleigh');
        xlabel('Particle Radius (nm)');
        ylabel(['Extinction Cross Section
(',crossunitsdisplay,'^{2})']);
        grid;
        axes(handles.extefficgraph);
        cla;
        plot(sizes,mieefficext,sizes,rayefficext);
        legend('Mie','Rayleigh');
        xlabel('Particle Radius (nm)');
        ylabel('Extinction Efficiency (unitless)');
        grid;
        axes(handles.extcoeffgraph);
        cla;
        plot(sizes,miecoeffext,sizes,raycoeffext);
        legend('Mie','Rayleigh');
        xlabel('Particle Radius (nm)');
        ylabel(['Extinction Coefficient (',coeffunitsdisplay,'^{ -
1})']);
        grid;
        if get(handles.excelfile,'Value') == 1
            fid = fopen(get(handles.excelfilename,'String'),'a');
            fprintf(fid,'Wavelength (nm) \t');
            fprintf(fid,'%2.6f \n',lambda0);
            fprintf(fid,'Refractive index of particle \t');
            fprintf(fid,'%2.6f \n',npart);
            fprintf(fid,'Refractive index of medium \t');
            fprintf(fid,'%2.6f \n',nmed);
            fprintf(fid,'N (particles per nm^3) \t');
            fprintf(fid,'%2.6f \n',Nconc);
            fprintf(fid,['Particle Radius (nm) \t Absorption cross
section (',crossunitsdisplay,'^2) \t Absorption efficiency (unitless)
\t Absorption coefficient (',coeffunitsdisplay,'^-1) \n']);
            for z=1:numel(all_sizes);
                fprintf(fid,'%2.6f \t %2.6E \t %2.6E \t %2.6E
\n',sizes(z),crossabs(z),efficabs(z),coeffabs(z));
            end
            fprintf(fid,['Particle Radius (nm) \t Mie Scattering cross
section (',crossunitsdisplay,'^2) \t Rayleigh Scattering cross section
(',crossunitsdisplay,'^2) \t Mie Scattering efficiency (unitless) \t
Rayleigh Scattering efficiency (unitless) \t Mie Scattering coefficient
(',coeffunitsdisplay,'^-1) \t Rayleigh Scattering coefficient
(',coeffunitsdisplay,'^-1) \n']);
            for z=1:numel(all_sizes);
                fprintf(fid,'%2.6f \t %2.6E \t %2.6E \t %2.6E \t %2.6E
```

```
\t %2.6E \t %2.6E
\n',sizes(z),miecrosssca(z),raycrosssca(z),mieefficsca(z),rayefficsca(z
),miecoeffsca(z),raycoeffsca(z));
            end
            fprintf(fid,['Particle Radius (nm) \t Mie Extinction cross
section (',crossunitsdisplay,'^2) \t Rayleigh Extinction cross section
(',crossunitsdisplay,'^2) \t Mie Extinction efficiency (unitless) \t
Rayleigh Extinction efficiency (unitless) \t Mie Extinction coefficient
(',coeffunitsdisplay,'^-1) \t Rayleigh Extinction coefficient
(',coeffunitsdisplay,'^-1) \n']);
            for z=1:numel(all_sizes);
                fprintf(fid,'%2.6f \t %2.6E \t %2.6E \t %2.6E \t %2.6E
\t %2.6E \t %2.6E
\n',sizes(z),miecrossext(z),raycrossext(z),mieefficext(z),rayefficext(z
),miecoeffext(z),raycoeffext(z));
            end
            fprintf(fid,'\n\n\n');
            fclose(fid);
        end
    end
    if get(handles.whichgraph,'String') == '3'
        axes(handles.scacrossgraph);
        cla;
        plot(sizes,miecrosssca,sizes,raycrosssca);
        legend('Mie','Rayleigh');
        xlabel('x (2*pi*nmed*a/wavelength)');
        ylabel(['Scattering Cross Section
(',crossunitsdisplay,'^{2})']);
        grid;
        axes(handles.scaefficgraph);
        cla;
        plot(sizes,mieefficsca,sizes,rayefficsca);
        legend('Mie','Rayleigh');
        xlabel('x (2*pi*nmed*a/wavelength)');
        ylabel('Scattering Efficiency (unitless)');
        grid;
        axes(handles.scacoeffgraph);
        cla;
        plot(sizes,miecoeffsca,sizes,raycoeffsca);
        legend('Mie','Rayleigh');
        xlabel('x (2*pi*nmed*a/wavelength)');
        ylabel(['Scattering Coefficient (',coeffunitsdisplay,'^{ -
1})']);
        grid;
        axes(handles.abscrossgraph);
        cla;
        plot(sizes,crossabs);
        xlabel('x (2*pi*nmed*a/wavelength)');
        ylabel(['Absorption Cross Section
(',crossunitsdisplay,'^{2})']);
        grid;
        axes(handles.absefficgraph);
        cla;
        plot(sizes,efficabs);
        xlabel('x (2*pi*nmed*a/wavelength)');
        ylabel('Absorption Efficiency (unitless)');
        grid;
        axes(handles.abscoeffgraph);
```

```
        cla;
        plot(sizes,coeffabs);
        xlabel('x (2*pi*nmed*a/wavelength)');
        ylabel(['Absorption Coefficient (',coeffunitsdisplay,'^{ -
1})']);
        grid;
        axes(handles.extcrossgraph);
        cla;
        plot(sizes,miecrossext,sizes,raycrossext);
        legend('Mie','Rayleigh');
        xlabel('x (2*pi*nmed*a/wavelength)');
        ylabel(['Extinction Cross Section
(',crossunitsdisplay,'^{2})']);
        grid;
        axes(handles.extefficgraph);
        cla;
        plot(sizes,mieefficext,sizes,rayefficext);
        legend('Mie','Rayleigh');
        xlabel('x (2*pi*nmed*a/wavelength)');
        ylabel('Extinction Efficiency (unitless)');
        grid;
        axes(handles.extcoeffgraph);
        cla;
        plot(sizes,miecoeffext,sizes,raycoeffext);
        legend('Mie','Rayleigh');
        xlabel('x (2*pi*nmed*a/wavelength)');
        ylabel(['Extinction Coefficient (',coeffunitsdisplay,'^{ -
1})']);
        grid;
        if get(handles.excelfile,'Value') == 1
            fid = fopen(get(handles.excelfilename,'String'),'a');
            fprintf(fid,'Wavelength (nm) \t');
            fprintf(fid,'%2.6f \n',lambda0);
            fprintf(fid,'Refractive index of particle \t');
            fprintf(fid,'%2.6f \n',npart);
            fprintf(fid,'Refractive index of medium \t');
            fprintf(fid,'%2.6f \n',nmed);
            fprintf(fid,'N (particles per nm^3) \t');
            fprintf(fid,'%2.6f \n',Nconc);
            fprintf(fid,['x (2*pi*nmed*a/wavelength) \t Absorption
cross section (',crossunitsdisplay,'^2) \t Absorption efficiency
(unitless) \t Absorption coefficient (',coeffunitsdisplay,'^-1) \n']);
            for z=1:numel(all_sizes);
                fprintf(fid,'%2.6f \t %2.6E \t %2.6E \t %2.6E
\n',xdata(z),crossabs(z),efficabs(z),coeffabs(z));
            end
            fprintf(fid,['x (2*pi*nmed*a/wavelength) \t Mie Scattering
cross section (',crossunitsdisplay,'^2) \t Rayleigh Scattering cross
section (',crossunitsdisplay,'^2) \t Mie Scattering efficiency
(unitless) \t Rayleigh Scattering efficiency (unitless) \t Mie
Scattering coefficient (',coeffunitsdisplay,'^-1) \t Rayleigh
Scattering coefficient (',coeffunitsdisplay,'^-1) \n']);
            for z=1:numel(all_sizes);
                fprintf(fid,'%2.6f \t %2.6E \t %2.6E \t %2.6E \t %2.6E
\t %2.6E \t %2.6E
\n',xdata(z),miecrosssca(z),raycrosssca(z),mieefficsca(z),rayefficsca(z
),miecoeffsca(z),raycoeffsca(z));
            end
```

```
            fprintf(fid,['x (2*pi*nmed*a/wavelength) \t Mie Extinction
cross section (',crossunitsdisplay,'^2) \t Rayleigh Extinction cross
section (',crossunitsdisplay,'^2) \t Mie Extinction efficiency
(unitless) \t Rayleigh Extinction efficiency (unitless) \t Mie
Extinction coefficient (',coeffunitsdisplay,'^-1) \t Rayleigh
Extinction coefficient (',coeffunitsdisplay,'^-1) \n']);
            for z=1:numel(all_sizes);
                fprintf(fid,'%2.6f \t %2.6E \t %2.6E \t %2.6E \t %2.6E
\t %2.6E \t %2.6E
\n',xdata(z),miecrossext(z),raycrossext(z),mieefficext(z),rayefficext(z
),miecoeffext(z),raycoeffext(z));
            end
            fprintf(fid,'\n\n\n');
            fclose(fid);
        end
    end
    if get(handles.whichgraph,'String') == '4'
        axes(handles.scacrossgraph);
        cla;
        plot(sizes,miecrosssca,sizes,raycrosssca);
        legend('Mie','Rayleigh');
        xlabel('rho (2*x*|m-1|)');
        ylabel(['Scattering Cross Section
(',crossunitsdisplay,'^{2})']);
        grid;
        axes(handles.scaefficgraph);
        cla;
        plot(sizes,mieefficsca,sizes,rayefficsca);
        legend('Mie','Rayleigh');
        xlabel('rho (2*x*|m-1|)');
        ylabel('Scattering Efficiency (unitless)');
        grid;
        axes(handles.scacoeffgraph);
        cla;
        plot(sizes,miecoeffsca,sizes,raycoeffsca);
        legend('Mie','Rayleigh');
        xlabel('rho (2*x*|m-1|)');
        ylabel(['Scattering Coefficient (',coeffunitsdisplay,'^{ -
1})']);
        grid;
        axes(handles.abscrossgraph);
        cla;
        plot(sizes,crossabs);
        xlabel('rho (2*x*|m-1|)');
        ylabel(['Absorption Cross Section
(',crossunitsdisplay,'^{2})']);
        grid;
        axes(handles.absefficgraph);
        cla;
        plot(sizes,efficabs);
        xlabel('rho (2*x*|m-1|)');
        ylabel('Absorption Efficiency (unitless)');
        grid;
        axes(handles.abscoeffgraph);
        cla;
        plot(sizes,coeffabs);
        xlabel('rho (2*x*|m-1|)');
        ylabel(['Absorption Coefficient (',coeffunitsdisplay,'^{ -
```

```
1})']);
        grid;
        axes(handles.extcrossgraph);
        cla;
        plot(sizes,miecrossext,sizes,raycrossext);
        legend('Mie','Rayleigh');
        xlabel('rho (2*x*|m-1|)');
        ylabel(['Extinction Cross Section
(',crossunitsdisplay,'^{2})']);
        grid;
        axes(handles.extefficgraph);
        cla;
        plot(sizes,mieefficext,sizes,rayefficext);
        legend('Mie','Rayleigh');
        xlabel('rho (2*x*|m-1|)');
        ylabel('Extinction Efficiency (unitless)');
        grid;
        axes(handles.extcoeffgraph);
        cla;
        plot(sizes,miecoeffext,sizes,raycoeffext);
        legend('Mie','Rayleigh');
        xlabel('rho (2*x*|m-1|)');
        ylabel(['Extinction Coefficient (',coeffunitsdisplay,'^{ -
1})']);
        grid;
        if get(handles.excelfile,'Value') == 1
            fid = fopen(get(handles.excelfilename,'String'),'a');
            fprintf(fid,'Wavelength (nm) \t');
            fprintf(fid,'%2.6f \n',lambda0);
            fprintf(fid,'Refractive index of particle \t');
            fprintf(fid,'%2.6f \n',npart);
            fprintf(fid,'Refractive index of medium \t');
            fprintf(fid,'%2.6f \n',nmed);
            fprintf(fid,'N (particles per nm^3) \t');
            fprintf(fid,'%2.6f \n',Nconc);
            fprintf(fid,['rho (2*x*|m-1|) \t Absorption cross section
(',crossunitsdisplay,'^2) \t Absorption efficiency (unitless) \t
Absorption coefficient (',coeffunitsdisplay,'^-1) \n']);
            for z=1:numel(all_sizes);
                fprintf(fid,'%2.6f \t %2.6E \t %2.6E \t %2.6E
\n',rho(z),crossabs(z),efficabs(z),coeffabs(z));
            end
            fprintf(fid,['rho (2*x*|m-1|) \t Mie Scattering cross
section (',crossunitsdisplay,'^2) \t Rayleigh Scattering cross section
(',crossunitsdisplay,'^2) \t Mie Scattering efficiency (unitless) \t
Rayleigh Scattering efficiency (unitless) \t Mie Scattering coefficient
(',coeffunitsdisplay,'^-1) \t Rayleigh Scattering coefficient
(',coeffunitsdisplay,'^-1) \n']);
            for z=1:numel(all_sizes);
                fprintf(fid,'%2.6f \t %2.6E \t %2.6E \t %2.6E \t %2.6E
\t %2.6E \t %2.6E
\n',rho(z),miecrosssca(z),raycrosssca(z),mieefficsca(z),rayefficsca(z),
miecoeffsca(z),raycoeffsca(z));
            end
            fprintf(fid,['rho (2*x*|m-1|) \t Mie Extinction cross
section (',crossunitsdisplay,'^2) \t Rayleigh Extinction cross section
(',crossunitsdisplay,'^2) \t Mie Extinction efficiency (unitless) \t
Rayleigh Extinction efficiency (unitless) \t Mie Extinction coefficient
```

```
(',coeffunitsdisplay,'^-1) \t Rayleigh Extinction coefficient
(',coeffunitsdisplay,'^-1) \n']);
            for z=1:numel(all_sizes);
                fprintf(fid,'%2.6f \t %2.6E \t %2.6E \t %2.6E \t %2.6E
\t %2.6E \t %2.6E
\n',rho(z),miecrossext(z),raycrossext(z),mieefficext(z),rayefficext(z),
miecoeffext(z),raycoeffext(z));
            end
            fprintf(fid,'\n\n\n');
            fclose(fid);
        end
    end
end
set(handles.calculatebutton,'ForegroundColor',[0 1 0]);
set(handles.calculatebutton,'String','Calculate');

% --- Executes on button press in excelfile.
function excelfile_Callback(hObject, eventdata, handles)
% hObject    handle to excelfile (see GCBO)
% eventdata  reserved - to be defined in lambda0 future version of
%            MATLAB
% handles    structure with handles and user data (see GUIDATA)
% Hint: get(hObject,'Value') returns toggle state of excelfile

function excelfilename_Callback(hObject, eventdata, handles)
% hObject    handle to excelfilename (see GCBO)
% eventdata  reserved - to be defined in lambda0 future version of
%            MATLAB
% handles    structure with handles and user data (see GUIDATA)
% Hints: get(hObject,'String') returns contents of excelfilename as
%        text
%        str2double(get(hObject,'String')) returns contents of
excelfilename as lambda0 double
% --- Executes during object creation, after setting all properties.
function excelfilename_CreateFcn(hObject, eventdata, handles)
% hObject    handle to excelfilename (see GCBO)
% eventdata  reserved - to be defined in lambda0 future version of
%            MATLAB
% handles    empty - handles not created until after all CreateFcns
%            called

% Hint: edit controls usually have lambda0 white background on Windows.
%       See ISPC and COMPUTER.
if ispc && isequal(get(hObject,'BackgroundColor'),
get(0,'defaultUicontrolBackgroundColor'))
    set(hObject,'BackgroundColor','white');
end

% --- Executes on button press in wavelengthbutton.
function wavelengthbutton_Callback(hObject, eventdata, handles)
% hObject    handle to singlelayercheck (see GCBO)
% eventdata  reserved - to be defined in a future version of MATLAB
% handles    structure with handles and user data (see GUIDATA)
% Hint: get(hObject,'Value') returns toggle state of singlelayercheck
set(handles.lambda0, 'BackgroundColor', [0 0 0]);
set(handles.astart, 'BackgroundColor', [0 0 0]);
set(handles.aend, 'BackgroundColor', [0 0 0]);
```

```
set(handles.ainc, 'BackgroundColor', [0 0 0]);
set(handles.lambda0start, 'BackgroundColor', [1 1 1]);
set(handles.lambda0end, 'BackgroundColor', [1 1 1]);
set(handles.lambda0inc, 'BackgroundColor', [1 1 1]);
set(handles.a, 'BackgroundColor', [1 1 1]);
set(handles.whichgraph,'String','1');
guidata(hObject,handles);

% --- Executes on button press in radiusbutton.
function radiusbutton_Callback(hObject, eventdata, handles)
% hObject    handle to singlelayercheck (see GCBO)
% eventdata  reserved - to be defined in a future version of MATLAB
% handles    structure with handles and user data (see GUIDATA)
% Hint: get(hObject,'Value') returns toggle state of singlelayercheck
set(handles.lambda0, 'BackgroundColor', [1 1 1]);
set(handles.astart, 'BackgroundColor', [1 1 1]);
set(handles.aend, 'BackgroundColor', [1 1 1]);
set(handles.ainc, 'BackgroundColor', [1 1 1]);
set(handles.lambda0start, 'BackgroundColor', [0 0 0]);
set(handles.lambda0end, 'BackgroundColor', [0 0 0]);
set(handles.lambda0inc, 'BackgroundColor', [0 0 0]);
set(handles.a, 'BackgroundColor', [0 0 0]);
set(handles.whichgraph,'String','2');
guidata(hObject,handles);

% --- Executes on button press in xbutton.
function xbutton_Callback(hObject, eventdata, handles)
% hObject    handle to singlelayercheck (see GCBO)
% eventdata  reserved - to be defined in a future version of MATLAB
% handles    structure with handles and user data (see GUIDATA)
% Hint: get(hObject,'Value') returns toggle state of singlelayercheck
set(handles.lambda0, 'BackgroundColor', [1 1 1]);
set(handles.astart, 'BackgroundColor', [1 1 1]);
set(handles.aend, 'BackgroundColor', [1 1 1]);
set(handles.ainc, 'BackgroundColor', [1 1 1]);
set(handles.lambda0start, 'BackgroundColor', [0 0 0]);
set(handles.lambda0end, 'BackgroundColor', [0 0 0]);
set(handles.lambda0inc, 'BackgroundColor', [0 0 0]);
set(handles.a, 'BackgroundColor', [0 0 0]);
set(handles.whichgraph,'String','3');
guidata(hObject,handles);

% --- Executes on button press in rhobutton.
function rhobutton_Callback(hObject, eventdata, handles)
% hObject    handle to singlelayercheck (see GCBO)
% eventdata  reserved - to be defined in a future version of MATLAB
% handles    structure with handles and user data (see GUIDATA)
% Hint: get(hObject,'Value') returns toggle state of singlelayercheck
set(handles.lambda0, 'BackgroundColor', [1 1 1]);
set(handles.astart, 'BackgroundColor', [1 1 1]);
set(handles.aend, 'BackgroundColor', [1 1 1]);
set(handles.ainc, 'BackgroundColor', [1 1 1]);
set(handles.lambda0start, 'BackgroundColor', [0 0 0]);
set(handles.lambda0end, 'BackgroundColor', [0 0 0]);
set(handles.lambda0inc, 'BackgroundColor', [0 0 0]);
set(handles.a, 'BackgroundColor', [0 0 0]);
set(handles.whichgraph,'String','4');
guidata(hObject,handles);
```

```
% --- Executes on selection change in crossunits.
function crossunits_Callback(hObject, eventdata, handles)
% hObject    handle to crossunits (see GCBO)
% eventdata  reserved - to be defined in a future version of MATLAB
% handles    structure with handles and user data (see GUIDATA)

% Hints: contents = get(hObject,'String') returns crossunits contents
%        as cell array
% contents{get(hObject,'Value')} returns selected item from crossunits


% --- Executes during object creation, after setting all properties.
function crossunits_CreateFcn(hObject, eventdata, handles)
% hObject    handle to crossunits (see GCBO)
% eventdata  reserved - to be defined in a future version of MATLAB
% handles    empty - handles not created until after all CreateFcns
%            called

% Hint: popupmenu controls usually have a white background on Windows.
%       See ISPC and COMPUTER.
if ispc && isequal(get(hObject,'BackgroundColor'),
get(0,'defaultUicontrolBackgroundColor'))
    set(hObject,'BackgroundColor','white');
end


% --- Executes on selection change in coeffunits.
function coeffunits_Callback(hObject, eventdata, handles)
% hObject    handle to coeffunits (see GCBO)
% eventdata  reserved - to be defined in a future version of MATLAB
% handles    structure with handles and user data (see GUIDATA)

% Hints: contents = get(hObject,'String') returns coeffunits contents
%        as cell array
% contents{get(hObject,'Value')} returns selected item from coeffunits


% --- Executes during object creation, after setting all properties.
function coeffunits_CreateFcn(hObject, eventdata, handles)
% hObject    handle to coeffunits (see GCBO)
% eventdata  reserved - to be defined in a future version of MATLAB
% handles    empty - handles not created until after all CreateFcns
%            called

% Hint: popupmenu controls usually have a white background on Windows.
%       See ISPC and COMPUTER.
if ispc && isequal(get(hObject,'BackgroundColor'),
get(0,'defaultUicontrolBackgroundColor'))
    set(hObject,'BackgroundColor','white');
end
```

REFERENCES

1. Zukauskas, A., Shur, M.S. & Gaska, R. *Introduction to Solid State Lighting*. (Wiley-Interscience, New York: 2002).

2. Navigant Consulting Inc. Energy savings potential of solid state lighting in general illumination applications. *US Department of Energy* (2003).

3. Tsao, J.Y. Light emitting diodes (LEDs) for general illumination. *Optoelectronics Industry Development Association, Washington DC* (2002).

4. Building Energy Data Book. *US Department of Energy* (2007).

5. Basic Research Needs for Solid-State Lighting: Report of the Basic Energy Sciences Workshop on Solid-State Lighting. *US Department of Energy* (2006).

6. Round, H.J. A note on carborundum. *Electrical world* **49**, 309 (1907).

7. Losev, O. Luminous carborundum [silicon carbide] detector and detection with crystals. *Telegrafi ya i Telefoniya bez Provodov* **44**, 485-494 (1927).

8. Holonyak Jr, N. & Bevacqua, S.F. Coherent (visible) light emission from Ga (AsP) junctions. *Applied Physics Letters* **1**, 82-83 (1962).

9. Nakamura, S., Mukai, T. & Senoh, M. Candela-class high-brightness InGaN/AIGaN double-heterostructure blue-light-emitting. *Applied Physics Letters* **64**, 1687–1689 (1994).

10. Nakamura, S. & Fasol, G. *The blue laser diode: GaN based light emitters and lasers*. (Springer, Berlin: 1997).

11. Schnitzer, I., Yablonovich, E., Caneau, C. & Gmitter, T.J. Ultra-high spontaneous emission quantum efficiency, 99.7% internally and 72% externally, from epitaxially lifted-off GaAs/AlGaAs double heterostructure. *Applied Physics Letters* **62**, 131-133 (1993).

12. Schubert, E.F. & Luo, H.X. Solid-state lighting–a benevolent technology. *Reports on Progress in Physics* **69**, 3069–3100 (2006).

13. Batentschuk, M., Schmitt, B., Schneider, J. & Winnacker, A. Color Engineering of Garnet Based Phosphors for Luminescence Conversion Light Emitting Diodes (LUCOLEDs). *Materials Research Society Symposium Proceedings* **560**, 215–220 (1999).

14. Schlotter, P., Baur, J., Hielscher, C., Kunzer, M., Obloh, H., Schmidt, R. & Schneider, J. Fabrication and characterization of GaN/InGaN/AlGaN double heterostructure LEDs and their application in luminescence conversion LEDs. *Materials Science & Engineering B* **59**, 390–394 (1999).

15. Narukawa, Y. & Mukai, T. High color rendering and high luminous efficacy white light emitting diodes. *Conference on Lasers and Electro-Optics* 346–347 (2003).

16. Tamura, T., Setomoto, T. & Taguchi, T. Illumination characteristics of lighting array using 10 candela-class white LEDs under AC 100V operation. *Journal of Luminescence* **87-89**, 1180–1182 (2000).

17. Wu, J.L. & Devenney, M. Optimization of cerium doped garnets using combinatorial chemistry for application as luminescent conversion phosphors in white LEDs. *Materials Research Society Symposium Proceedings* **560**, 65–70 (1999).

18. Narukawa, Y., Narita, J., Sakamoto, T., Deguchi, K., Yamada, T. & Mukai, T. Ultra-high efficiency white light emitting diodes. *Japanese Journal of Applied Physics* **45**, L1084–L1086 (2006).

19. Bogner, G., Debray, A., Heidel, G., Hoehn, K., Mueller, U. & Schlotter, P. White LED. *Proceedings of SPIE* **3621**, 143-150 (1999).

20. Yam, F.K. & Hassan, Z. Innovative advances in LED technology. *Microelectronics Journal* **36**, 129–137 (2005).

21. Xie, R.J., Hirosaki, N., Kimura, N., Sakuma, K. & Mitomo, M. 2-phosphor-converted white light-emitting diodes using oxynitride/nitride phosphors. *Applied Physics Letters* **90**, 191101 (2007).

22. Yang, C.C., Lin, C.M., Chen, Y.J., Wu, Y.T., Chuang, S.R., Liu, R.S. & Hu, S.F. Highly stable three-band white light from an InGaN-based blue light-emitting diode chip precoated with (oxy) nitride green/red phosphors. *Applied Physics Letters* **90**, 123503 (2007).

23. Steigerwald, D.A., Bhat, J.C., Collins, D., Fletcher, R.M., Holcomb, M.O., Ludowise, M.J., Martin, P.S. & Rudaz, S.L. Illumination with solid state lighting technology. *IEEE Journal of Selected Topics in Quantum Electronics* **8**, 310–320 (2002).

24. Liu, C.H. & Wu, R.K. n-UV+ blue/green/red white light emitting diode lamps. *Japanese Journal of Applied Physics* **42**, 2284–2287 (2003).

25. Wu, H., Zhang, X., Guo, C., Xu, J., Wu, M. & Su, Q. Three-band white light from InGaN-based blue LED chip precoated with green/red phosphors. *IEEE Photonics Technology Letters* **17**, 1160–1162 (2005).

26. Sheu, J.K., Chang, S.J., Kuo, C.H., Su, Y.K., Wu, L.W., Lin, Y.C., Lai, W.C., Tsai, J.M., Chi, G.C. & Wu, R.K. White-light emission from near UV InGaN-GaN LED chip precoated with blue/green/red phosphors. *IEEE Photonics Technology Letters* **15**, 18–20 (2003).

27. Chhajed, S., Xi, Y., Li, Y.L., Gessmann, T. & Schubert, E.F. Influence of junction temperature on chromaticity and color-rendering properties of trichromatic white-light sources based on light-emitting diodes. *Journal of Applied Physics* **97**, 054506 (2005).

28. Muthu, S., Schuurmans, F.J. & Pashley, M.D. Red, green, and blue LEDs for white light illumination. *IEEE Journal of Selected Topics in Quantum Electronics* **8**, 333–338 (2002).

29. d'Andrade, B.W. & Forrest, S.R. White organic light-emitting devices for solid-state lighting. *Advanced Materials* **16**, 1585-1595 (2004).

30. Zhi-lin, Z., Xue-yin, J., Wen-qing, Z., Bu-xin, Z. & Shao-hong, X. A white organic light emitting diode with improved stability. *Journal of Physics D, Applied Physics* **34**, 3083–3087 (2001).

31. Mitschke, U. & Bäuerle, P. The electroluminescence of organic materials. *Journal of Materials Chemistry* **10**, 1471–1507 (2000).

32. Ko, C.W. & Tao, Y.T. Bright white organic light-emitting diode. *Applied Physics Letters* **79**, 4234-4236 (2001).

33. Tasch, S., List, E.J.W., Ekström, O., Graupner, W., Leising, G., Schlichting, P., Rohr, U., Geerts, Y., Scherf, U. & Müllen, K. Efficient white light-emitting diodes realized with new processable blends of conjugated polymers. *Applied Physics Letters* **71**, 2883-2885 (1997).

34. Chuen, C.H. & Tao, Y.T. Highly-bright white organic light-emitting diodes based on a single emission layer. *Applied Physics Letters* **81**, 4499-4501 (2002).

35. Heeger, A.J. Light emission from semiconducting polymers: light-emitting diodes, light-emitting electrochemical cells, lasers and white light for the future. *Solid State Communications* **107**, 673–680 (1998).

36. Gong, X., Wang, S., Moses, D., Bazan, G.C. & Heeger, A.J. Multilayer polymer light-emitting diodes: White-light emission with high efficiency. *Advanced Materials* **17**, 2053–2053 (2005).

37. Kido, J., Kimura, M. & Nagai, K. Multilayer white light-emitting organic electroluminescent device. *Science* **267**, 1332-1334 (1995).

38. Duggal, A.R., Shiang, J.J., Heller, C.M. & Foust, D.F. Organic light-emitting devices for illumination quality white light. *Applied Physics Letters* **80**, 3470-3472 (2002).

39. Granström, M. & Inganäs, O. White light emission from a polymer blend light emitting diode. *Applied Physics Letters* **68**, 147-149 (1996).

40. Yang, J.P., Jin, Y.D., Heremans, P.L., Hoefnagels, R., Dieltiens, P., Blockhuys, F., Geise, H.J., Van der Auweraer, M. & Borghs, G. White light emission from a single layer organic light emitting diode fabricated by spincoating. *Chemical Physics Letters* **325**, 251–256 (2000).

41. Zugang, L. & Nazare, H. White organic light-emitting diodes emitting from both hole and electron transport layers. *Synthetic Metals* **111-112**, 47–51 (2000).

42. Chen, S.A., Chuang, K.R., Chao, C.I. & Lee, H.T. White-light emission from electroluminescence diode with polyaniline as the emitting layer. *Synthetic Metals* **82**, 207–210 (1996).

43. Kido, J., Ikeda, W., Kimura, M. & Nagai, K. White-light-emitting organic electroluminescent device using lanthanide complexes. *Japanese Journal of Applied Physics* **35**, L394–L396 (1996).

44. Schubert, E.F. *Light-emitting diodes*. (Cambridge University Press: 2006).

45. Schnitzer, I., Yablonovitch, E., Caneau, C., Gmitter, T.J. & Scherer, A. 30% external quantum efficiency from surface textured, thin-film light-emitting diodes. *Applied Physics Letters* **63**, 2174-2176 (1993).

46. Windisch, R., Heremans, P., Dutta, B., Kuijk, M., Schoberth, S., Kiesel, P., Dohler, G.H., Borghs, G. & IMEC, L. High-efficiency non-resonant cavity light-emitting diodes. *Electronics Letters* **34**, 1153–1154 (1998).

47. Windisch, R., Heremans, P., Knobloch, A., Kiesel, P., Döhler, G.H., Dutta, B. & Borghs, G. Light-emitting diodes with 31% external quantum efficiency by outcoupling of lateral waveguide modes. *Applied Physics Letters* **74**, 2256-2258 (1999).

48. Hunt, N.E.J., Schubert, E.F., Logan, R.A. & Zydzik, G.J. Enhanced spectral power density and reduced linewidth at 1.3 mm in an InGaAsP quantum well resonant-cavity light-emitting diode. *Applied Physics Letters* **61**, 2287–2289 (1992).

49. Kato, T., Susawa, H., Hirotani, M., Saka, T., Ohashi, Y., Shichi, E. & Shibata, S. GaAs/GaAs surface emitting IR LED with Bragg reflector grown by MOCVD. *Journal of Crystal Growth* **107**, 832–835 (1991).

50. Sugawara, H., Itaya, K., Nozaki, H. & Hatakoshi, G. High-brightness InGaAlP green light-emitting diodes. *Applied Physics Letters* **61**, 1775-1777 (1992).

51. Schubert, E.F., Hunt, N.E.J., Micovic, M., Malik, R.J., Sivco, D.L., Cho, A.Y. & Zydzik, G.J. Highly efficient light-emitting diodes with microcavities. *Science* **265**, 943-945 (1994).

52. Schubert, E.F., Wang, Y.H., Cho, A.Y., Tu, L.W. & Zydzik, G.J. Resonant cavity light-emitting diode. *Applied Physics Letters* **60**, 921-923 (1992).

53. Lin, S.Y., Fleming, J.G., Hetherington, D.L., Smith, B.K., Biswas, R., Ho, K.M., Sigalas, M.M., Zubrzycki, W., Kurtz, S.R. & Bur, J. A three-dimensional photonic crystal operating at infrared wavelengths. *Nature* **394**, 251–253 (1998).

54. Fan, S., Villeneuve, P.R., Joannopoulos, J.D. & Schubert, E.F. High extraction efficiency of spontaneous emission from slabs of photonic crystals. *Physical Review Letters* **78**, 3294–3297 (1997).

55. Boroditsky, M., Krauss, T.F., Coccioli, R., Vrijen, R., Bhat, R. & Yablonovitch, E. Light extraction from optically pumped light-emitting diode by thin-slab photonic crystals. *Applied Physics Letters* **75**, 1036-1038 (1999).

56. Lee, R.K., Xu, Y. & Yariv, A. Modified spontaneous emission from a two-dimensional photonic bandgap crystal slab. *Journal of the Optical Society of America B* **17**, 1438–1442 (2000).

57. Joannopoulos, J.D., Villeneuve, P.R. & Fan, S. Photonic crystals: putting a new twist on light. *Nature* **386**, 143-149 (1997).

58. Boroditsky, M., Vrijen, R., Krauss, T.F., Coccioli, R., Bhat, R. & Yablonovitch, E. Spontaneous emission extraction and Purcell enhancement from thin-film 2-D photonic crystals. *Journal of Lightwave Technology* **17**, 2096–2112 (1999).

59. Baba, T., Inoshita, K., Tanaka, H., Yonekura, J., Ariga, M., Matsutani, A., Miyamoto, T., Koyama, F. & Iga, K. Strong enhancement of light extraction efficiency in GaInAsP2-D-arranged microcolumns. *Journal of Lightwave Technology* **17**, 2113–2120 (1999).

60. Chow, E., Lin, S.Y., Johnson, S.G., Villeneuve, P.R., Joannopoulos, J.D., Wendt, J.R., Vawter, G.A., Zubrzycki, W., Hou, H. & Alleman, A. Three-dimensional control of light in a two-dimensional photonic crystal slab. *Nature* **407**, 983–986 (2000).

61. Krauss, T.F., De La Rue, R.M. & Brand, S. Two-dimensional photonic-bandgap structures operating at near-infrared wavelengths. *Nature* **383**, 699-702 (1996).

62. Krames, M.R., Ochiai-Holcomb, M., Höfler, G.E., Carter-Coman, C., Chen, E.I., Tan, I.H., Grillot, P., Gardner, N.F., Chui, H.C., Huang, J.W., Stockman, S.A., Kish, F.A. & Craford, M.G. High-power truncated-inverted-pyramid (AlGa) InP/GaP light-emitting diodes exhibiting> 50% external quantum efficiency. *Applied Physics Letters* **75**, 2365-2367 (1999).

63. Carr, W.N. & Pittman, G.E. One-watt GaAs PN junction infrared source. *Applied Physics Letters* **3**, 173–175 (1963).

64. Franklin, A.R. & Newman, R. Shaped electroluminescent GaAs diodes. *Journal of Applied Physics* **35**, 1153-1155 (1964).

65. Taguchi, T., Uchida, Y. & Kobashi, K. Efficient white LED lighting and its application to medical fields. *Physica Status Solidi A* **201**, 2730-2735 (2004).

66. Narendran, N. Improved performance white LED. *Proceedings of SPIE* **5941**, 594108 (2005).

67. Kim, J.K., Luo, H., Schubert, E.F., Cho, J., Sone, C. & Park, Y. Strongly enhanced phosphor efficiency in GaInN white light-emitting diodes using remote phosphor configuration and diffuse reflector cup. *Japanese Journal of Applied Physics* **44**, L649-L651 (2005).

68. Guo, X., Li, Y.L. & Schubert, E.F. Efficiency of GaN/InGaN light-emitting diodes with interdigitated mesa geometry. *Applied Physics Letters* **79**, 1936-1938 (2001).

69. Jin, S.X., Li, J., Li, J.Z., Lin, J.Y. & Jiang, H.X. GaN microdisk light emitting diodes. *Applied Physics Letters* **76**, 631-633 (2000).

70. Möller, S. & Forrest, S.R. Improved light out-coupling in organic light emitting diodes employing ordered microlens arrays. *Journal of Applied Physics* **91**, 3324-3327 (2002).

71. Madigan, C.F., Lu, M.H. & Sturm, J.C. Improvement of output coupling efficiency of organic light-emitting diodes by backside substrate modification. *Applied Physics Letters* **76**, 1650-1652 (2000).

72. Jin, S.X., Li, J., Lin, J.Y. & Jiang, H.X. InGaN/GaN quantum well interconnected microdisk light emitting diodes. *Applied Physics Letters* **77**, 3236-3238 (2000).

73. Wong, W.S., Sands, T., Cheung, N.W., Kneissl, M., Bour, D.P., Mei, P., Romano, L.T. & Johnson, N.M. Fabrication of thin-film InGaN light-emitting diode membranes by laser lift-off. *Applied Physics Letters* **75**, 1360-1362 (1999).

74. Haerle, V., Hahn, B., Kaiser, S., Weimar, A., Bader, S., Eberhard, F., Plössl, A. & Eisert, D. High brightness LEDs for general lighting applications Using the new ThinGaN™-Technology. *Physica Status Solidi A* **201**, 2736-2739 (2004).

75. Gao, Y., Fujii, T., Sharma, R., Fujito, K., Danbaars, S.P. & Nakamura, S. Roughening hexagonal surface morphology on laser lift-off (LLO) n face GaN with simple photo-enhanced chemical wet etching. *Japanese Journal of Applied Physics* **43**, L637-L639 (2004).

76. Alivisatos, A.P. Semiconductor clusters, nanocrystals, and quantum dots. *Science* **271**, 933-937 (1996).

77. Murray, C.B., Kagan, C.R. & Bawendi, M.G. Synthesis and characterization of monodisperse nanocrystals and close-packed nanocrystal assemblies. *Annual Review of Materials Science* **30**, 545–610 (2000).

78. Efros, A.L. & Efros, A.L. Interband light absorption in semiconductor sphere. *Soviet Physics Semiconductors* **16**, 772-775 (1982).

79. Brus, L.E. Electron–electron and electron-hole interactions in small semiconductor crystallites: The size dependence of the lowest excited electronic state. *The Journal of Chemical Physics* **80**, 4403-4409 (1984).

80. Norris, D.J. & Bawendi, M.G. Measurement and assignment of the size-dependent optical spectrum in CdSe quantum dots. *Physical Review B* **53**, 16338–16346 (1996).

81. Norris, D.J., Sacra, A., Murray, C.B. & Bawendi, M.G. Measurement of the size dependent hole spectrum in CdSe quantum dots. *Physical Review Letters* **72**, 2612–2615 (1994).

82. Ekimov, A.I., Hache, F., Schanne-Klein, M.C., Ricard, D., Flytzanis, C., Kudryavtsev, I.A., Yazeva, T.V., Rodina, A.V. & Efros, A.L. Absorption and intensity-dependent photoluminescence measurements on CdSe quantum dots: assignment of the first electronic transitions. *Journal of the Optical Society of America B* **10**, 100–107 (1993).

83. Parak, W.J., Gerion, D., Pellegrino, T., Zanchet, D., Micheel, C., Williams, S.C., Boudreau, R., Le Gros, M.A., Larabell, C.A. & Alivisatos, A.P. Biological applications of colloidal nanocrystals. *Nanotechnology* **14**, 15–27 (2003).

84. Wu, X., Liu, H., Liu, J., Haley, K.N., Treadway, J.A., Larson, J.P., Ge, N., Peale, F. & Bruchez, M.P. Immunofluorescent labeling of cancer marker Her2 and other cellular targets with semiconductor quantum dots. *Nature Biotechnology* **21**, 41–46 (2002).

85. Jaiswal, J.K., Mattoussi, H., Mauro, J.M. & Simon, S.M. Long-term multiple color imaging of live cells using quantum dot bioconjugates. *Nature Biotechnology* **21**, 47–51 (2002).

86. Chan, W.C., Maxwell, D.J., Gao, X., Bailey, R.E., Han, M. & Nie, S. Luminescent quantum dots for multiplexed biological detection and imaging. *Current Opinion in Biotechnology* **13**, 40–46 (2002).

87. Akerman, M.E., Chan, W.C., Laakkonen, P., Bhatia, S.N. & Ruoslahti, E. Nanocrystal targeting in vivo. *Proceedings of the National Academy of Sciences* **99**, 12617–12621 (2002).

88. Michalet, X., Pinaud, F.F., Bentolila, L.A., Tsay, J.M., Doose, S., Li, J.J., Sundaresan, G., Wu, A.M., Gambhir, S.S. & Weiss, S. Quantum dots for live cells, in vivo imaging, and diagnostics. *Science* **307**, 538–544 (2005).

89. Gao, X., Chan, W.C. & Nie, S. Quantum-dot nanocrystals for ultrasensitive biological labeling and multicolor optical encoding. *Journal of Biomedical Optics* **7**, 532-537 (2002).

90. Han, M., Gao, X., Su, J.Z. & Nie, S. Quantum-dot-tagged microbeads for multiplexed optical coding of biomolecules. *Nature Biotechnology* **19**, 631–635 (2001).

91. Voura, E.B., Jaiswal, J.K., Mattoussi, H. & Simon, S.M. Tracking metastatic tumor cell extravasation with quantum dot nanocrystals and fluorescence emission-scanning microscopy. *Nature Medicine* **10**, 993–998 (2004).

92. Murphy, C.J. Optical sensing with quantum dots. *Analytical Chemistry* **74**, 520A-526A (2002).

93. Medintz, I.L., Uyeda, H.T., Goldman, E.R. & Mattoussi, H. Quantum dot bioconjugates for imaging, labelling and sensing. *Nature Materials* **4**, 435–446 (2005).

94. Medintz, I.L., Clapp, A.R., Mattoussi, H., Goldman, E.R., Fisher, B. & Mauro, J.M. Self-assembled nanoscale biosensors based on quantum dot FRET donors. *Nature Materials* **2**, 630–638 (2003).

95. Zhang, C.Y., Yeh, H.C., Kuroki, M.T. & Wang, T.H. Single-quantum-dot-based DNA nanosensor. *Nature Materials* **4**, 826–831 (2005).

96. Tran, P.T., Anderson, G.P., Mauro, J.M. & Mattoussi, H. Use of luminescent CdSe-ZnS nanocrystal bioconjugates in quantum dot-based nanosensors. *Physica Status Solidi B* **229**, 427-432 (2002).

97. Li, Y.Q., Rizzo, A., Cingolani, R. & Gigli, G. Bright white-light-emitting device from ternary nanocrystal composites. *Advanced Materials* **18**, 2545-2548 (2006).

98. Lee, J., Sundar, V.C., Heine, J.R., Bawendi, M.G. & Jensen, K.F. Full color emission from II-VI semiconductor quantum dot-polymer composites. *Advanced Materials* **12**, 1102-1105 (2000).

99. Chen, H., Hsu, C. & Hong, H. InGaN-CdSe-ZnSe quantum dots white LEDs. *IEEE Photonics Technology Letters* **18**, 193–195 (2006).

100. Lim, J., Jun, S., Jang, E., Baik, H., Kim, H. & Cho, J. Preparation of highly luminescent nanocrystals and their application to light-emitting diodes. *Advanced Materials* **19**, 1927–1932 (2007).

101. Park, J.H., Kim, J.Y., Chin, B.D., Kim, Y.C., Kim, J.K. & Park, O.O. White emission from polymer/quantum dot ternary nanocomposites by incomplete energy transfer. *Nanotechnology* **15**, 1217–1220 (2004).

102. Lee, S., Cho, W.J., Han, I.K., Choi, W.J. & Lee, J.I. White light emitting silicon nanocrystals as nanophosphor. *Physica Status Solidi B* **241**, 2767–2770 (2004).

103. Ali, M., Chattopadhyay, S., Nag, A., Kumar, A., Sapra, S., Chakraborty, S. & Sarma, D.D. White-light emission from a blend of CdSeS nanocrystals of different Se: S ratio. *Nanotechnology* **18**, 75401–75401 (2007).

104. Chen, H.S., Wang, S.J., Lo, C.J. & Chi, J.Y. White-light emission from organics-capped ZnSe quantum dots and application in white-light-emitting diodes. *Applied Physics Letters* **86**, 131905 (2005).

105. Colvin, V.L., Schlamp, M.C. & Alivisatos, A.P. Light-emitting diodes made from cadmium selenide nanocrystals and a semiconducting polymer. *Nature* **370**, 354-357 (1994).

106. Mattoussi, H., Radzilowski, L.H., Dabbousi, B.O., Thomas, E.L., Bawendi, M.G. & Rubner, M.F. Electroluminescence from heterostructures of poly (phenylene vinylene) and inorganic CdSe nanocrystals. *Journal of Applied Physics* **83**, 7965-7974 (1998).

107. Rizzo, A., Li, Y., Kudera, S., Della Sala, F., Zanella, M., Parak, W.J., Cingolani, R., Manna, L. & Gigli, G. Blue light emitting diodes based on fluorescent CdSe/ ZnS nanocrystals. *Applied Physics Letters* **90**, 051106 (2007).

108. Munro, A.M., Bardecker, J.A., Liu, M.S., Cheng, Y.J., Niu, Y.H., Plante, I.J., Jen, A.K. & Ginger, D.S. Colloidal CdSe quantum dot electroluminescence: ligands and light-emitting diodes. *Microchimica Acta* **160**, 345–350 (2008).

109. Steckel, J.S., Snee, P., Coe-Sullivan, S., Zimmer, J.P., Halpert, J.E., Anikeeva, P., Kim, L.A., Bulovic, V. & Bawendi, M.G. Color-saturated green-emitting QD-LEDs. *Angewandte Chemie* **45**, 5796-5799 (2006).

110. Zhao, J., Bardecker, J.A., Munro, A.M., Liu, M.S., Niu, Y., Ding, I.K., Luo, J., Chen, B., Jen, A.K. & Ginger, D.S. Efficient CdSe/CdS quantum dot light-emitting diodes using a thermally polymerized hole transport layer. *Nano Letters* **6**, 463-467 (2006).

111. Dabbousi, B.O., Bawendi, M.G., Onitsuka, O. & Rubner, M.F. Electroluminescence from CdSe quantum-dot/polymer composites. *Applied Physics Letters* **66**, 1316-1318 (1995).

112. Zhao, J., Zhang, J., Jiang, C., Bohnenberger, J., Basché, T. & Mews, A. Electroluminescence from isolated CdSe/ ZnS quantum dots in multilayered light-emitting diodes. *Journal of Applied Physics* **96**, 3206-3210 (2004).

113. Coe-Sullivan, S., Woo, W.K., Steckel, J.S., Bawendi, M. & Bulović, V. Tuning the performance of hybrid organic/inorganic quantum dot light-emitting devices. *Organic Electronics* **4**, 123–130 (2003).

114. Schlamp, M.C., Peng, X. & Alivisatos, A.P. Improved efficiencies in light emitting diodes made with CdSe (CdS) core/shell type nanocrystals and a semiconducting polymer. *Journal of Applied Physics* **82**, 5837-5842 (1997).

115. Jun, S., Jang, E., Park, J. & Kim, J. Photopatterned semiconductor nanocrystals and their electroluminescence from hybrid light-emitting devices. *Langmuir* **22**, 2407–2410 (2006).

116. Coe, S., Woo, W.K., Bawendi, M. & Bulovic, V. Electroluminescence from single monolayers of nanocrystals in molecular organic devices. *Nature* **420**, 800–803 (2002).

117. Gao, M.Y., Richter, B., Kirstein, S. & Mohwald, H. Electroluminescence studies on self-assembled films of PPV and CdSe nanoparticles. *Journal of Physical Chemistry B* **102**, 4096–4103 (1998).

118. Li, Y., Rizzo, A., Mazzeo, M., Carbone, L., Manna, L., Cingolani, R. & Gigli, G. White organic light-emitting devices with CdSe/ZnS quantum dots as a red emitter. *Journal of Applied Physics* **97**, 113501 (2005).

119. Rohwer, L.E., Abrams, B.L., Wilcoxon, J.P. & Thoma, S.G. Development of solid state light sources based on II-VI semiconductor quantum dots. *Proceedings of SPIE* **5366**, 66-74 (2004).

120. Mueller, A.H., Petruska, M.A., Achermann, M., Werder, D.J., Akhadov, E.A., Koleske, D.D., Hoffbauer, M.A. & Klimov, V.I. Multicolor light-emitting diodes based on semiconductor nanocrystals encapsulated in GaN charge injection layers. *Nano Letters* **5**, 1039–1044 (2005).

121. Achermann, M., Petruska, M.A., Kos, S., Smith, D.L., Koleske, D.D. & Klimov, V.I. Energy-transfer pumping of semiconductor nanocrystals using an epitaxial quantum well. *Nature* **429**, 642–646 (2004).

122. Achermann, M., Petruska, M.A., Koleske, D.D., Crawford, M.H. & Klimov, V.I. Nanocrystal-based light-emitting diodes utilizing high-efficiency nonradiative energy transfer for color conversion. *Nano Letters* **6**, 1396–1400 (2006).

123. Bowers II, M.J., McBride, J.R. & Rosenthal, S.J. White-light emission from magic-sized cadmium selenide nanocrystals. *Journal of the American Chemical Society* **127**, 15378-15379 (2005).

124. Schreuder, M.A., Gosnell, J.D., Smith, N.J., Warnement, M.R., Weiss, S.M. & Rosenthal, S.J. Encapsulated white-light CdSe nanocrystals as nanophosphors for solid-state lighting. *Journal of Materials Chemistry* **18**, 970–975 (2008).

125. Gosnell, J.D., Schreuder, M.A., Bowers II, M.J., Rosenthal, S.J. & Weiss, S.M. Cadmium selenide nanocrystals as white-light phosphors. *Proceedings of SPIE* **6337**, 63370A (2006).

126. Gosnell, J.D., Schreuder, M.A., Rosenthal, S.J. & Weiss, S.M. Efficiency improvements of white-light CdSe nanocrystal-based LEDs. *Proceedings of SPIE* **6669**, 66690R (2007).

127. Gosnell, J., Rosenthal, S. & Weiss, S. White Light Emission Characteristics of Polymer-encapsulated CdSe Nanocrystal Films. *IEEE Photonics Technology Letters* **22**, 541-543 (2010).

128. Dukes, A.D., III, Schreuder, M.A., Sammons, J.A., McBride, J.R., Smith, N.J. & Rosenthal, S.J. Pinned emission from ultrasmall cadmium selenide nanocrystals. *The Journal of Chemical Physics* **129**, 121102-4 (2008).

129. Schreuder, M.A., McBride, J.R., Dukes, A.D., Sammons, J.A. & Rosenthal, S.J. Control of surface state emission via phosphonic acid modulation in ultrasmall CdSe nanocrystals: the role of ligand electronegativity. *The Journal of Physical Chemistry C* **113**, 8169-8176 (2009).

130. Landes, C., Braun, M., Burda, C. & El-Sayed, M.A. Observation of large changes in the band gap absorption energy of small CdSe nanoparticles induced by the adsorption of a strong hole acceptor. *Nano Letters* **1**, 667–670 (2001).

131. Jose, R., Zhanpeisov, N.U., Fukumura, H., Baba, Y. & Ishikawa, M. Structure-property correlation of CdSe clusters using experimental results and first-principles DFT calculations. *Journal of the American Chemical Society* **128**, 629–636 (2006).

132. Landes, C.F., Braun, M. & El-Sayed, M.A. On the nanoparticle to molecular size transition: fluorescence quenching studies. *The Journal of Physical Chemistry B* **105**, 10554–10558 (2001).

133. DiMaio, J.R., Kokuoz, B. & Ballato, J. White light emissions through down-conversion of rare-earth doped LaF3 nanoparticles. *Optics Express* **14**, 11412–11417 (2006).

134. Sapra, S., Mayilo, S., Klar, T.A., Rogach, A.L. & Feldmann, J. Bright white light emission from semiconductor nanocrystals: by chance and by design. *Advanced Materials* **19**, 569-572 (2007).

135. Nag, A. & Sarma, D.D. White light from Mn2+-Doped CdS nanocrystals: a new approach. *The Journal of Physical Chemistry C* **111**, 13641-13644 (2007).

136. Thoma, S.G., Abrams, B.L., Rohwer, L.S., Sanchez, A., Wilcoxon, J.P. & Woessner, S.M. Encapsulation of nanoparticles for the manufacture of solid state lighting devices. *Proceedings of SPIE* **5276**, 202-212 (2004).

137. Shea-Rohwer, L.E., Martin, J.E. & Kelley, D.F. Increasing the luminescent quantum yield of CdS nanoparticles having broadband emission. *Journal of The Electrochemical Society* **157**, J1-J7 (2010).

138. Maege, I., Jaehne, E., Henke, A., Adler, H.J., Bram, C., Jung, C. & Stratmann, M. Self-assembling adhesion promoters for corrosion resistant metal polymer interfaces. *Progress in Organic Coatings* **34**, 1–12 (1997).

139. Dabbousi, B.O., Rodriguez-Viejo, J., Mikulec, F.V., Heine, J.R., Mattoussi, H., Ober, R., Jensen, K.F. & Bawendi, M.G. (CdSe)ZnS core−shell quantum dots: synthesis and characterization of a size series of highly luminescent nanocrystallites. *The Journal of Physical Chemistry B* **101**, 9463-9475 (1997).

140. Kuno, M., Lee, J.K., Dabbousi, B.O., Mikulec, F.V. & Bawendi, M.G. The band edge luminescence of surface modified CdSe nanocrystallites: probing the luminescing state. *The Journal of Chemical Physics* **106**, 9869-9882 (1997).

141. Zhu, D., Corbett, B., Roycroft, B., Maaskant, P., McAleese, C., Akhter, M., Kappers, M.J. & Humphreys, C.J. Enhanced efficiency of near-UV emitting LEDs for solid state lighting applications. *Proceedings of SPIE* **6797**, 67970O (2007).

142. Pan, C.C., Hsieh, C.H., Lin, C.W. & Chyi, J.I. Light output improvement of InGaN ultraviolet light-emitting diodes by using wet-etched stripe-patterned sapphire substrates. *Journal of Applied Physics* **102**, 084503 (2007).

143. Cheong, H.S., Na, M.G., Choi, Y.J., Cuong, T.V., Hong, C.H., Suh, E.K., Kong, B.H. & Cho, H.K. Structural and optical properties of near-UV LEDs grown on V-grooved sapphire substrates fabricated by wet etching. *Journal of Crystal Growth* **298**, 699–702 (2007).

144. Tran, N.T. & Shi, F.G. Studies of phosphor concentration and thickness for phosphor-based white light-emitting-diodes. *Journal of Lightwave Technology* **26**, 3556–3559 (2008).

145. Murase, N., Li, C., Yang, P. & Ando, M. Comparison of brightness of emitting semiconductor nanocrystals with that of rare-earth phosphor. *Japanese Journal of Applied Physics* **46**, 7545–7548 (2007).

146. Fujita, S.S., Sakamoto, A.A. & Tanabe, S.S. Luminescence characteristics of YAG glass–ceramic phosphor for white LED. *IEEE Journal of Selected Topics in Quantum Electronics* **14**, 1387–1391 (2008).

147. Sommer, C., Wenzl, F.P., Hartmann, P., Pachler, P., Schweighart, M. & Leising, G. Tailoring of the color conversion elements in phosphor-converted high-power LEDs by optical simulations. *IEEE Photonics Technology Letters* **20**, 739–741 (2008).

148. Nizamoglu, S. & Demir, H.V. Nanocrystal-based hybrid white light generation with tunable colour parameters. *Journal of Optics A* **9**, S419-S424 (2007).

149. Bowen Katari, J.E., Colvin, V.L. & Alivisatos, A.P. X-ray photoelectron spectroscopy of CdSe nanocrystals with applications to studies of the nanocrystal surface. *The Journal of Physical Chemistry* **98**, 4109–4117 (1994).

150. van Sark, W.G., Frederix, P.L., Van den Heuvel, D.J., Gerritsen, H.C., Bol, A.A., van Lingen, J.N., de Mello Donega, C. & Meijerink, A. Photooxidation and photobleaching of single CdSe/ZnS quantum dots probed by room-temperature time-resolved spectroscopy. *The Journal of Physical Chemistry B* **105**, 8281–8284 (2001).

151. Chang, C.C., Chern, R.L., Chang, C.C., Chu, C.C. & Chi, J.Y. Monte carlo simulation of optical properties of phosphor-screened ultraviolet light in a white light-emitting device. *Japanese Journal of Applied Physics* **44**, 6056–6061 (2005).

152. Gosnell, J.D. & Weiss, S.M. Light scattering by white-emitting CdSe nanocrystals and traditional YAG:Ce3+ phosphor particles. *Materials Research Society Symposium Proceedings* **1148E**, 1148-PP09-02 (2009).

153. Abeles, F. Recherches sur la propagation des ondes électromagnétiques sinusoıd dans les milieux stratifiés. *Annales de Physique* **5**, 596–640 (1950).

154. Macleod, H.A. *Thin-film optical filters*. (Institute of Physics Publishing, Bristol, PA: 2001).

155. Haranath, D., Chander, H., Sharma, P. & Singh, S. Enhanced luminescence of Y3Al5O12: Ce3+ nanophosphor for white light-emitting diodes. *Applied Physics Letters* **89**, 173118 (2006).

156. Su, L.T., Tok, A.I.Y., Boey, F.Y.C., Zhang, X.H., Woodhead, J.L. & Summers, C.J. Photoluminescence phenomena of Ce-doped YAlO nanophosphors. *Journal of Applied Physics* **102**, 083541 (2007).

157. Jia, D., Wang, Y., Guo, X., Li, K., Zou, Y.K. & Jia, W. Synthesis and characterization of YAG:Ce LED nanophosphors. *Journal of the Electrochemical Society* **154**, J1-J4 (2007).

158. Nozik, A.J. Quantum dot solar cells. *Physica E: Low-dimensional Systems and Nanostructures* **14**, 115–120 (2002).

159. Greenham, N.C., Peng, X. & Alivisatos, A.P. Charge separation and transport in conjugated-polymer/semiconductor-nanocrystal composites studied by photoluminescence quenching and photoconductivity. *Physical Review B* **54**, 17628–17637 (1996).

160. van de Hulst, H.C. *Light scattering by small particles*. (Wiley, New York: 1957).

161. Bohren, C.F. & Huffman, D.R. *Absorption and scattering of light by small particles*. (Wiley, New York: 1983).

162. Weiner, I., Rust, M. & Donnelly, T.D. Particle size determination: an undergraduate lab in Mie scattering. *American Journal of Physics* **69**, 129-136 (2001).

163. Cox, A.J., DeWeerd, A.J. & Linden, J. An experiment to measure Mie and Rayleigh total scattering cross sections. *American Journal of Physics* **70**, 620-625 (2002).

164. Leatherdale, C.A., Woo, W.K., Mikulec, F.V. & Bawendi, M.G. On the absorption cross section of CdSe nanocrystal quantum dots. *The Journal of Physical Chemistry B* **106**, 7619–7622 (2002).

165. Probert-Jones, J.R. Resonance component of backscattering by large dielectric spheres. *Journal of the Optical Society of America A* **1**, 822–830 (1984).

166. Gupta, T.K. & Doh, J. Optical properties of polycrystalline CdSe films. *Journal of Materials Research* **7**, 1243-1246 (1992).

167. Shaalan, M. & Müller, R. The optical constants of CdSe thin films in the visible and near-IR. *Solar Cells* **28**, 185-192 (1990).

168. Palik, E.D. *Handbook of Optical Constants of Solids II*. (Academic Press: 1991).

169. Yu, W.W., Qu, L., Guo, W. & Peng, X. Experimental determination of the extinction coefficient of CdTe, CdSe, and CdS nanocrystals. *Chemistry of Materials* **15**, 2854–2860 (2003).

170. Gosnell, J. D., Schreuder, M. A., McBride, J. R., Rosenthal, S. J. & Weiss, S. M. Size-dependent extinction coefficient and absorption cross section of CdSe nanocrystals (in preparation).

171. Schmelz, O., Mews, A., Basché, T., Herrmann, A. & Mullen, K. Supramolecular complexes from CdSe nanocrystals and organic fluorophors. *Langmuir* **17**, 2861–2865 (2001).

172. Striolo, A., Ward, J., Prausnitz, J.M., Parak, W.J., Zanchet, D., Gerion, D., Milliron, D. & Alivisatos, A.P. Molecular weight, osmotic second virial coefficient, and extinction coefficient of colloidal CdSe nanocrystals. *The Journal of Physical Chemistry B* **106**, 5500-5505 (2002).

173. Jasieniak, J., Smith, L., Embden, J.V., Mulvaney, P. & Califano, M. Re-examination of the size-dependent absorption properties of CdSe quantum dots. *The Journal of Physical Chemistry C* **113**, 19468-19474 (2009).

174. Taylor, J., Kippeny, T. & Rosenthal, S.J. Surface stoichiometry of CdSe nanocrystals determined by Rutherford backscattering spectroscopy. *Journal of Cluster Science* **12**, 571–582 (2001).

175. Shiang, J.J., Kadavanich, A.V., Grubbs, R.K. & Alivisatos, A.P. Symmetry of annealed wurtzite CdSe nanocrystals: assignment to the C3v point group. *The Journal of Physical Chemistry* **99**, 17417-17422 (1995).

176. Soloviev, V.N., Eichhofer, A., Fenske, D. & Banin, U. Molecular limit of a bulk semiconductor: size dependence of the "band gap" in CdSe cluster molecules. *Journal of the American Chemical Society* **122**, 2673-2674 (2000).

177. Rogach, A.L., Kornowski, A., Gao, M., Eychmuller, A. & Weller, H. Synthesis and characterization of a size series of extremely small thiol-stabilized CdSe nanocrystals. *The Journal of Physical Chemistry B* **103**, 3065–3069 (1999).

178. Taylor, J.R. *An Introduction to Error Analysis: The Study of Uncertainties in Physical Measurements*. (University Science Books: 1996).